

AD-A133758

SOLID STATE ELECTRONICS LABORATORY

STANFORD ELECTRONICS LABORATORIES
DEPARTMENT OF ELECTRICAL ENGINEERING
STANFORD UNIVERSITY · STANFORD, CA 94305



SSEL 11-79

INTERIM TECHNICAL REPORT
SUBMITTED TO
ADVANCED RESEARCH PROJECTS AGENCY
ARLINGTON, VIRGINIA 22209

LASER AND ELECTRON BEAM PROCESSING OF SEMICONDUCTORS: CW BEAM PROCESSING OF ION IMPLANTED SILICON

BY
STANFORD UNIVERSITY
STANFORD, CALIFORNIA 94305

FOR THE PERIOD
JANUARY 1, 1978 THROUGH
DECEMBER 31, 1980

APPROVED FOR PUBLIC RELEASE
DISTRIBUTION UNLIMITED

MDA 903-78-C-0128
AO 3493

Dr. James F. Gibbons
Program Manager and Principal Investigator
Professor of Electrical Engineering
Stanford Electronics Laboratories

OCT 19 1983
S A

DTIC FILE COPY

83 10 04 191

MDA903-78-C-0128

Principal Investigator -- J. F. Gibbons

Research on the use of directed energy sources, particularly cw lasers and electron beams, for semiconductor processing operations has been carried out at Stanford under the principal sponsorship of DARPA since January 1, 1978. Over the two years from January 1, 1978 to December 31, 1980, research effort has been concentrated on three principal topics:

- (1) Use of lasers and electron beams for annealing ion implanted silicon under solid phase conditions;
- (2) Use of lasers and arc sources for recrystallization of thin polysilicon films and a study of the device potential of this material; and
- (3) Use of cw lasers and electron beams for promoting metal silicide reactions.

In the following report we collect papers on the annealing of ion implanted silicon published during the period of time indicated above. A brief summary of the papers has been prepared to provide an overview of the work. Two subsequent reports will collect and summarize papers published on polysilicon and silicide formation, respectively.



Account For

1. ☒ 2. ☐ 3. ☐ 4. ☐

Section

A

SUMMARY OF STANFORD PAPERS ON CW BEAM PROCESSING OF ION IMPLANTED SILICON

Research at Stanford on the use of cw lasers and electron beams for annealing ion implanted silicon has led to the publication of 17 original papers and 20 reviews. The central contributions contained in this work are summarized briefly below with reference to the attached papers:

- Paper 1 describes the construction and basic operation of the system used to scan a focussed laser beam across a semiconductor sample at rates appropriate for processing operations.
- Papers 2 and 3 provide the theoretical foundation for cw beam processing under solid phase (non-melting) conditions.
- Papers 4-7 provide experimental confirmation of the cw beam annealing mechanism and measurements of the electronic and crystallographic properties of As⁺-implanted silicon annealed with both scanning laser and scanning electron beam systems. The As⁺-dose in these experiments is sufficient to produce amorphicity but not sufficient to introduce As at concentration levels above the solid solubility.
- Papers 8-10 show that the cw beam annealing process is capable of incorporating implanted As in Si at concentrations that exceed the solid solubility and provide new measurements of the solid solubility of As as a single substitutional (non-complexed) dopant in Si at temperatures in the range 700°C - 1000°C.
- Paper 11 describes the cw laser annealing of boron implanted silicon under implantation conditions that are typical of present application for bipolar devices.
- Papers 12-16 describe DLTS measurements from which the energy levels and spatial distributions of point defects remaining in Si following cw beam annealing are inferred. Both laser and electron beam systems are used and the results are compared (in paper 16). The annihilation of these point defects by subsequent low temperature thermal annealing is also measured.
- Paper 17 (a review) contains original results on the use of a cw laser to oxidize Si surfaces and to reduce Q_{SS} in SiO₂ films deposited on a Si substrate.

OVERVIEW OF STANFORD PAPERS ON
CW BEAM PROCESSING OF ION IMPLANTED SILICON

Paper No. 1.

"A Laser Scanning Apparatus for Annealing of Ion Implantation Damage in Semiconductors, A. Cat and J. F. Gibbons, Applied Physics Letters 32, 3, 172 (Feb. 1, 1978)."

This paper describes the construction and basic operation of a system that can be used to scan a focussed laser beam across a semiconductor sample at rates appropriate for processing operations. Experimentation with the system described in the paper have led to the following modifications:

(a) An improved, temperature-controlled sample holder has been built allowing the substrate temperature to be increased to 550°C.

(b) The 79 mm focussing lens used for the initial experiments was found to have a focal length that was somewhat too short. Lenses with focal lengths in the range of 136-267 mm are typically used in present experiments.

Contribution: This paper contains the first published results on cw laser annealing of As⁺-implanted-amorphized silicon. Two-point resistance probe measurements were employed to show that the laser annealing process can produce sheet resistivities as low as those obtained by thermal annealing.

Paper No. 2

"Temperature Distributions Produced in Semiconductors by a Scanning Elliptical or Circular CW Laser Beam", Y. I. Nissim, A. Lietoila, R. B. Gold and J. F. Gibbons, Journal of Applied Physics 51, 1, 274 (Jan 1980)."

Contribution: This paper provides a general mathematical solution for the surface temperatures produced by a laser beam scanning over a target having thermal conductivity K(T). Detailed numerical results are presented for silicon and gallium arsenide. The central results of the paper are presented as a set of normalized, "linear temperature", curves, with

Paper No. 2 (Cont'd)

temperature plotted as a function of (beam power/spot radius). The true temperature is obtained from the "linear temperature" for each material by use of a Kirchoff transform. The final results permit specification of experimental conditions to achieve required processing temperatures.

Paper No. 3

"Calculation of Solid Phase Reaction Rates Induced by a Scanning CW Laser", R. B. Gold and J. F. Gibbons, Journal of Applied Physics 51, 2, 1256 (Feb. 1980)."

Most of the processes induced by cw laser scanning are thermally activated. Thus, when the results of a laser treatment are to be quantitatively evaluated, one has to account for the fact that the temperature at each point of the sample varies rapidly with time as the (approximately) Gaussian beam is scanned over the point in question.

Contribution: This paper presents a formalism for treating the general problem in which a given point on the sample surface is assumed to be heated to the maximum possible beam-induced temperature for an effective dwell time t_{eff} . This effective dwell time is related to the real dwell time by a "dwell time reduction factor", which is calculated as a function of the substrate temperature for various process activation energies (e.g., 2.2 eV for silicon epitaxial solid phase regrowth, and 2.35 eV for palladium silicide formation). The predicted growth rates are found to agree accurately with experiment, justifying the use of the model for process calculations.

Paper No. 4

"A Study of the Mechanism of CW Laser Annealing of Arsenic-Implanted Silicon", A. Gat, A. Lietoila and J. F. Gibbons, J. of Appl. Phys. 50, 4, 2926 (April 1979).

Contribution: This paper demonstrates experimentally that laser annealing of implantation amorphized silicon proceeds with a temperature-time dependence that can be accurately modelled as a thermal equilibrium solid phase epitaxial process.

Paper No. 5

"Physical and Electrical Properties of Laser-Annealed, Ion Implanted Silicon", A. Gat, J. F. Gibbons, T. J. Magee, J. Peng, V. R. Deline, P. Williams and C. A. Evans, Jr.", Appl. Phys. Letters 32, 5, 276 (1 March 1978)."

Contribution: This paper establishes the fundamental properties of cw laser annealing of As⁺-implantation-amorphizes silicon, which are:

- (a) Complete recovery of the crystal structure to a resolution of 50 Å as judged by transmission electron microscopy and transmission electron diffraction.
- (b) Complete electrical activation of the impurities as judged by spreading resistance measurements.
- (c) Absence of any dopant redistribution during laser annealing as judged by secondary ion mass spectroscopy compared with theoretical impurity profiles constructed from LSS range statistics.

Paper No. 6

"Scanning Electron Beam Annealing of Arsenic Implanted Silicon", J. L. Regolini, J. F. Gibbons, T. W. Sigmon, R. F. W. Pease, T. J. Magee and J. Peng", Appl. Phys. Lett. 34, 6, 410 (15 March 1979).

Contribution: This paper provides the first experimental demonstration that a scanning electron beam can be used to anneal ion implanted silicon. A scanning cw electron beam obtained from a Hamilton Standard Welder, operated at a beam voltage of 30 keV and beam current of 0.5 mA, is shown to yield annealing results closely similar to those obtained with the cw laser in paper No. 5 above. The analytical methods employed in this study are similar to those used in paper No. 5 except that MeV ion channeling is also used to study recovery of crystal structure and lattice location of the implanted species after annealing.

Paper No. 7

"Physical Properties of Ion Implanted, SEM-annealed Silicon", J. L. Regolini, N. M. Johnson, R. Sinclair, T. W. Sigmon and J. F. Gibbons, in Laser and Electron Beam Processing of Materials, editors C. W. White and P. S. Peercy, Academic Press, New York, 1980, pg. 297 ff."

Contribution: The feasibility of a modified scanning electron microscope for electron beam annealing purposes is demonstrated. The results obtained and the analytical methods employed are identical to those used in papers Nos. 5 and 6 above.

Paper No. 8

"The Solubility of Arsenic and Silicon as Determined by Thermal Annealing of Metastable, Laser Annealed Concentrations", A. Lietoila, J. F. Gibbons, J. L. Regolini, T. W. Sigmon, T. J. Magee, J. Peng and J. D. Hong, in Laser and Electron Beam Processing of Electronic Materials, Proceedings Vol. 80-1, The Electrochemical Society, Princeton, New Jersey, 1980, p. 350."

Contribution: It is shown in this paper that cw laser annealing is capable of activating metastable As-concentrations of at least $1 \times 10^{21} / \text{cm}^3$, which is approximately three times the value obtained by thermal processing. Thermal annealing causes the metastable laser-annealed concentration to relax to an equilibrium value which allows the solubility of arsenic in silicon to be measured. The solubility is determined as a function of temperature in the range from 700-1000°C, with values that are substantially less than those reported by Trumbore [F. A. Trumbore, BSTJ, Vol. 39, p. 205 (1960)].

The nature of the arsenic deactivation from the metastable state is studied with both TEM and MeV ion channeling, and the thermal activation energy of the deactivation process is measured. This deactivation energy is found to be very nearly 1 eV, leading to the speculation that vacancy generation is responsible for the ultimate formation of As-V-As clusters and subsequent precipitation of rods and defect loops.

Paper No. 9

"Metastable As Concentrations Formed by Scanned E-Beam Annealing of As-implanted Silicon", J. L. Regolini, T. W. Sigmon, and J. F. Gibbons, Appl. Phys. Lett. 32, 2, 114 (15 July 1979).

Contribution: MeV ion channeling and differential van der Pauw measurements are used to show that cw electron beam annealing is also capable of creating metastable arsenic concentrations of up to $1 \times 10^{21}/\text{cm}^3$ with properties very similar to results obtained in paper No. 8.

Paper No. 10

"Metastable Arsenic Concentrations in Silicon Achieved by Ion Implantation and Rapid Thermal Annealing", A. Lietoila, R. B. Gold, J. F. Gibbons, and T. W. Sigmon, to be published in J. of Appl. Phys."

Contribution: It is shown in this paper that conventional thermal annealing, when done sufficiently quickly, can also create a metastable arsenic concentration. However, the maximum concentration obtained is not as high as the concentration obtained with either laser or electron beam annealing. The results of this paper, together with those of papers 8 and 9, show that arsenic atoms initially take up lattice sites during the solid phase epitaxial regrowth of an amorphized layer. If the equilibrium solubility of the dopant is exceeded, deactivation (or precipitation) takes place after the recrystallization process. This is possible because the (measured) time constant for precipitation or deactivation is substantially greater than that for the epitaxial regrowth process.

Paper No. 11

"Use of a Scanning Cw Kr Laser to Obtain Diffusion-Free Annealing of B-implanted Silicon", A. Gat, J. F. Gibbons, T. J. Magee, J. Peng, P. Williams, V. Deline, and C. A. Evans, Jr., Appl. Phys. Lett. 33, 5, 389 (1 Sept 1978)."

Contribution: This is to date the only published study of cw laser annealing of boron-implanted silicon. The case is fundamentally different from those described in papers 1 through 10 in that the boron implantation does not typically produce an amorphous layer in the

Paper No. 11 (Cont'd)

implanted silicon. Thus the annealing mechanism is not simply a solid phase epitaxial process proceeding from the underlying crystalline substrate toward the sample surface. Rather the annihilation of point defects and activation of the implanted dopant take place simultaneously throughout the damaged layer. Annealing in this case is expected to be more difficult than in the presence of an amorphous layer. Nonetheless, two-point probe measurements and transmission electron microscopy showed that the laser annealing resulted in essentially complete dopant activation with good crystalline quality. SIMS measurements indicate that impurity diffusion during laser annealing is negligible in contrast to the significant dopant redistribution produced during typical thermal annealing sequences.

Paper No. 12

"Constant-capacitance DLTS Measurement of Defect-density Profiles in Semiconductors", N. M. Johnson and D. J. Bartelink, R. B. Gold and J. F. Gibbons, J. Appl. Phys. 50, 7, 4828 (July 1979).

Contribution: This paper provides the theoretical foundation for the constant capacitance DLTS measurement of defect-density profiles in semiconductors.

Paper No. 13

"Electron Defect Levels in Self-Implanted CW Laser-Annealed Silicon", N. M. Johnson, R. B. Gold and J. F. Gibbons, Appl. Phys. Lett. 34, 10, 704 (15 May 1979).

Contribution: This paper contains measurements of the energy levels and spatial distribution of electron defect levels introduced by the cw laser annealing of ion-implanted Si. The measured emission spectrum is dominated by two levels near the middle of the Si forbidden energy gap, with activation energies of 0.49 eV and 0.56 eV. An additional level at 0.28 eV appears upon subsequent thermal annealing at 450°C. Schottky barrier techniques are used to form the rectifying barrier required for the measurement.

Paper No. 14

"Deep Levels in Ion-Implanted, CW Laser-Annealed Silicon", N. M. Johnson, R. B. Gold, A. Lietoila and J. F. Gibbons, Published in Laser-Solid Interactions and Laser Processing - 1978 (American Institute of Physics, New York, 1979), eds. S. D. Ferris, H. J. Leamy, and J. M. Poate, AIP Conference Proceedings, No. 50, pp. 550-555.

Contribution: This paper presents a comparison of defect levels obtained from Schottky barrier DLTS measurements where the cw laser process is used to anneal both Czochralski-grown and epitaxial silicon wafers. Results obtained with these two substrates are essentially identical.

Paper No. 15

"Deep Levels in Scanned Electron-Beam Annealed Silicon", N. M. Johnson, J. L. Regolini and D. J. Bartelink, Appl. Phys. Lett. 36, 6, 425 (15 Mar 1980).

Contribution: This paper provides DLTS measurements of defect levels introduced by scanned electron beam annealing. The trap energy and depth distributions obtained are similar to those obtained with cw laser annealing.

Paper No. 16

"A Comparison of Ion-Implantation Induced Deep Levels in Scanned Electron-Beam Annealed and CW Laser-Annealed Silicon", N. M. Johnson, D. J. Bartelink and M. D. Moyer, J. F. Gibbons, A. Lietoila, K. N. Ratnakumar and J. L. Regolini, presented at Materials Research Symposium, Cambridge, Mass. Nov. 27-30, 1979. Published in Proceedings.

Contribution: This paper describes electron defect levels measured in ion implanted p-n junction diodes annealed by both cw laser and electron beam processing. As in the previous papers, the two annealing processes are found to be comparable though there is some indication that the final defect density produced with the electron beam system is lower.

Paper No. 17

"Applications of Scanning cw Lasers and Electron Beams in Silicon Technology", J. F. Gibbons, Proc. 11th Conference on Solid State Devices, Tokyo 1979; Japanese J. Appl. Phys. 19 (1980), Supplement 19-1, pp. 121-128.

Contribution: This paper contains a broad review of cw beam annealing as it may apply to silicon technology. Original results presented in this paper include measurements of (1) the oxidation rate for crystalline silicon subjected to cw laser irradiation and (2) the degree to which the scanning cw laser can be used to reduce Q_{SS} in SiO_2 films deposited on Si substrates by CVD techniques. In both cases the results are found to be similar to those obtained with conventional furnace processing.

Paper #1

"A Laser Scanning Apparatus for Annealing of Ion Implantation Damage in Semiconductors."

Paper #2

"Temperature Distributions Produced in Semiconductors by a Scanning Elliptical or Circular CW Laser Beam."

Paper #3

"Calculation of Solid Phase Reaction Rates Induced by a Scanning CW Laser."

Paper #4

"A Study of the Mechanism of CW Laser Annealing of Arsenic-Implanted Silicon."

Paper #5

"Physical and Electrical Properties of Laser-Annealed, Ion Implanted Silicon."

Paper #6

"Scanning Electron Beam Annealing of Arsenic Implanted Silicon."

Paper #7

"Physical Properties of Ion Implanted, SEM-Annealed Silicon."

Paper #8

"The Solubility of Arsenic and Silicon as Determined by Thermal Annealing of Metastable, Laser Annealed Concentrations."

Paper #9

"Metastable As Concentrations Formed by Scanned E-Beam Annealing of As-Implanted Silicon."

Paper #10

"Metastable Arsenic Concentrations in Silicon Achieved by Ion Implantation and Rapid Thermal Annealing."

Paper #11

"Use of Scanning CW Kr Laser to Obtain Diffusion-Free Annealing of B-Implanted Silicon."

Paper #12

"Constant-Capacitance DLTS Measurement of Defect-Density Profiles in Semiconductors."

Paper #13

"Electron Defect Levels in Self-Implanted CW Laser-Annealed Silicon."

Paper #14

"Deep Levels in Ion-Implanted, CW-Annealed Silicon."

Paper #15

"Deep Levels in Scanned Electron-Beam Annealed Silicon."

Paper #16

"A Comparison of Ion-Implantation Induced Deep Levels in Scanned Electron-Beam Annealed and CW Laser-Annealed Silicon."

Paper #17

"Applications of Scanning CW Lasers and Electron Beams in Silicon Technology."

A laser-scanning apparatus for annealing of ion-implantation damage in semiconductors

A. Gat and J. F. Gibbons

Stanford Electronics Laboratories, Stanford, California 94305

(Received 15 August 1977; accepted for publication 11 November 1977)

The feasibility of annealing ion-implantation damage by means of a continuous high-power laser is demonstrated. An apparatus for the scanning of a semiconductor sample is described and a first-order set of optimum conditions for annealing ion-implanted Si is given. A preliminary comparison between laser and thermal annealing shows comparable results in terms of electrical activity of the annealed samples.

PACS numbers: 81.40.Ef, 61.70.Tm

A major problem associated with ion implantation in semiconductors is that a thin layer of material at or near the surface of the crystal is damaged during the implantation, often being driven completely amorphous. For most device applications some process of annealing is needed to restore the crystallinity of the implanted layer.

Several authors¹⁻⁵ have reported the use of pulsed ruby and Nd-YAG lasers for annealing of ion-implantation damage in semiconductors. In addition, Klimenko *et al.*⁶ describe annealing that can be obtained with a continuous argon ion laser. However Klimenko's experiments were conducted with a low power density in the laser beam, which made it necessary to irradiate the material for several seconds to restore the crystallinity of the ion-implanted layer. Also Kachurin *et al.*⁷ describe a mechanical scanner for use with an argon ion laser for annealing of implanted layers. In that system the semiconductor sample was put out of the focal plane of the lens and a set of optimal conditions for a 40-mm lens was given.

The objective of this work is to prove the feasibility of continuous beam laser annealing under different conditions than those described by the authors cited above. In particular, we wish to describe a system in which the implanted sample is placed in the focal plane of the lens. Since the laser beam has a long and narrow waist at its focal point, small scanning angles will not alter the peak intensity on the sample, thus assuring annealing uniformity at different scan angles. A set of annealing conditions appropriate for use with a 79-mm lens has been determined for As-implanted Si and will be described. The apparatus used for scanning the laser will also be described and a preliminary comparison of thermal and laser annealing will be given.

The scanning mechanism used for these experiments employs synchronous deflection of the laser beam by two mirrors driven by galvanometers. A focusing lens positioned in front of the first mirror is used to control the spot size on the sample. It is essential that the sample be in the focal plane of the lens to minimize nonuniformity problems during the scan. A schematic description of the optical system is shown in Fig. 1. Since the optimal conditions for the anneal were not known at the outset, a versatile electronic system was built to drive the mirrors.

The block diagram of the driving electronics is shown in Fig. 2. The sensitivity of the galvanometers used is $10^\circ/\text{A}$ with linearity better than 1%. The x -scan rate can be varied from 0.1 to 840 sec, the x amplitude from -10° to $+10^\circ$, the y -step size from 3×10^{-3} to 0.9 deg, and the y limit to 10° . Control of the spot size can be achieved by selecting the proper lens. The laser used was a Spectra Physics argon ion model 171-08 with a maximum power rating of 15 W.

To determine appropriate annealing conditions for a typical implantation case, As⁺ was implanted into Si at 100 keV to a dose of $5 \times 10^{14} \text{ cm}^{-2}$. The Si sample was $\sim 3 \Omega \text{ cm } p$ type, oriented in the $\langle 100 \rangle$ direction. Using a 79-mm lens, the optimum conditions were found to be (1) total laser power in the multiline mode of 7 W, (2) x -scan rate of 2.76 cm/sec, and (3) y increment at the end of each x line of $\sim 15 \mu$ (estimated). The calculated spot size of the TEM₀₀ mode was $38.5 \mu\text{m}$ in diameter, which corresponds to a power density of $6 \times 10^5 \text{ W/cm}^2$. The width of an annealed line was $22 \mu\text{m}$, and the energy density needed for the anneal was calculated to be 5.4 kJ/cm^2 .

A critical parameter for annealing in this system is

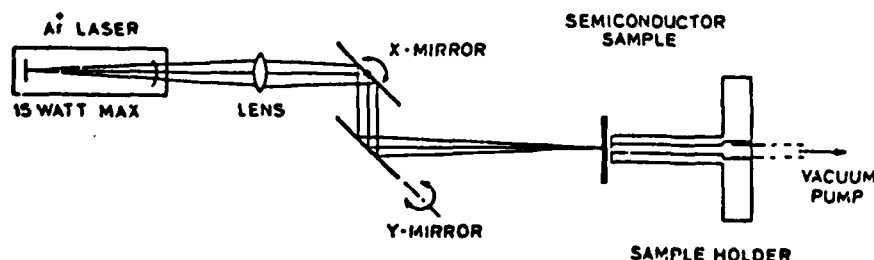


FIG. 1. A general schematic of the annealing apparatus. Includes Ar⁺ laser, lens, perpendicular x and y mirrors, and a vacuum sample holder.

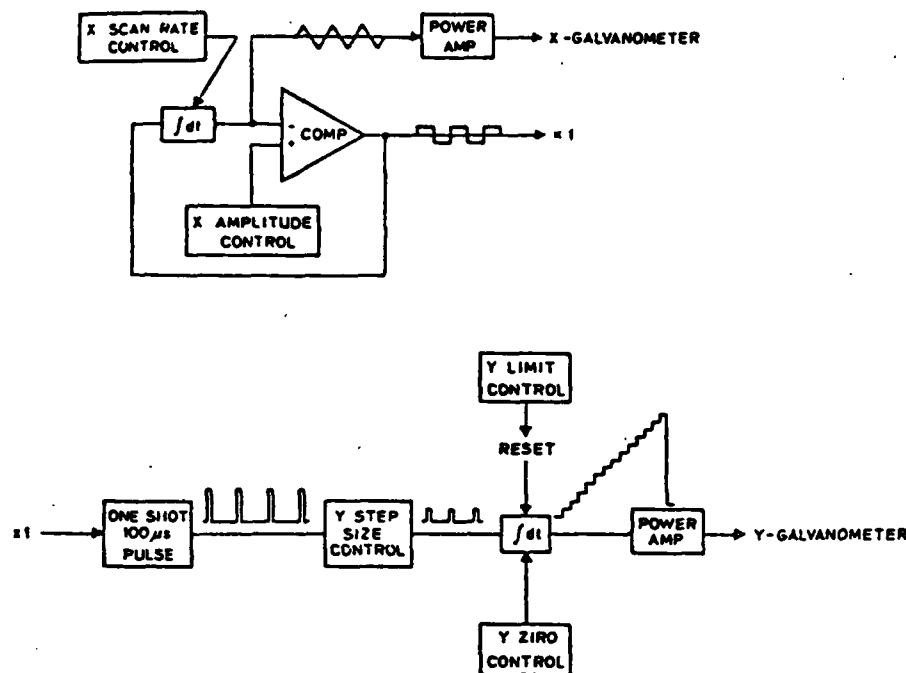


FIG. 2. Block diagram of the galvanometer drivers used for scanning the x-y mirrors in the laser annealing apparatus.

the power density in the scanning beam. In particular, deviations on the order of 8% in power density were found to give unsatisfactory annealing, i.e., a total power of 6.5 W failed to produce annealing, while a total power of 7.5 W produced discoloration and possibly thermal etching in the region where adjacent scan lines overlap.

To compare the laser anneal with a conventional thermal anneal, implanted samples identical to those used for the laser anneal were thermally annealed in nitrogen at 1000°C for 30 min. Surface spreading resistance measurements (two-point probe) were performed on both types of annealed samples. The probes were stepped in the x direction on the samples and the probe to probe resistance was recorded. The results of these measurements are given in Fig. 3. In the comparison five samples were thermally annealed, of which two are

shown in Fig. 3. The resistance values for all thermally annealed samples were $157 \pm 3 \Omega$. For illustration purposes sample No. S5-3 had only its right-half laser annealed and its measurement shows a decrease of resistivity from 3000 Ω in the unannealed area to 150 Ω after a laser scan. A total of five samples were laser annealed. These samples were found to have resistance values of $160 \pm 10 \Omega$.

Evidently the electrical activity obtained from the laser anneal is very similar to that obtained in the thermally annealed samples, which implies that a high degree of electrical activation was produced by the laser anneal. Preliminary SIMS data indicate that the impurity profile after laser annealing is essentially identical to the as-implanted profile, whereas the thermally annealed profile shows significant diffusive redistribution.⁶ A more thorough comparison of laser- and thermally annealed samples including SIMS, back-scattering, TEM, and electrical analysis of the annealed layers is being performed and will be submitted for publication shortly.

The authors would like to thank Luke Meisenbach and Carrol Frankfurt for the construction of the scanning apparatus and John Goldsmith for assistance in the use of the Ar⁺ laser and other optical equipment. The work was supported by NSF Grant No. DMR7618000.

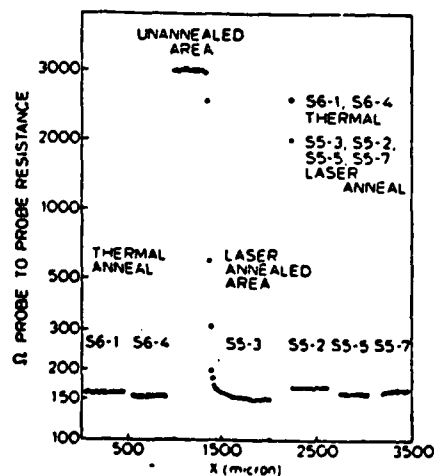


FIG. 3. Surface spreading resistance measurements done of implanted silicon samples subjected to laser and thermal anneal.

¹G.A. Kachurin, N.B. Pridachin, and L.S. Smirnov, Sov. Phys.-Semicond. 9, 946 (1975).

²E.I. Shtyrkov, I.B. Khibullin, M.M. Zavipov, M.F. Galyatudinov, and R.M. Bayazitov, Sov. Phys.-Semicond. 9, 1309 (1975).

³A.Kh. Antonenko, N.N. Gerasimenko, A.V. Dvorenchenko, L.S. Smirnov, and G.M. Tseitlin, Sov. Phys.-Semicond. 10, 81 (1976).

⁴V.V. Bolotov, N.R. Pricachin, and L.S. Smirnov, Sov. Phys.-Semicond. 10, 338 (1976).

⁵O.G. Kutukova and L.N. Stel'tsov, Sov. Phys.-Semicond. 10, 265 (1976).

⁶A.G. Klimenko, E.A. Klimenko, and V.I. Donin, Sov. J. Quantum Electron. 5, 1289 (1976).

⁷G.A. Kachurin, E.V. Nidaev, A.V. Khodyachikh, and L.A. Kovaleva, Sov. Phys.-Semicond. 10, 1128 (1976).

⁸C.A. Evans (private communication).

Temperature distributions produced in semiconductors by a scanning elliptical or circular cw laser beam

Y. I. Nissim, A. Lietoila, R. B. Gold, and J. F. Gibbons
Stanford Electronics Laboratories, Stanford, California 94305

(Received 25 June 1979; accepted for publication 6 August 1979)

Temperature profiles induced by a cw laser beam in a semiconductor are calculated. The calculation is done for an elliptical scanning beam and covers a wide range of experimental conditions. (The limiting case of a circular beam is also studied.) This calculation is developed in the particular cases of silicon and gallium arsenide, where the temperature dependence of the thermal conductivity has been taken into consideration. Using a cylindrical lens to produce an elliptical beam with an aspect ratio of 20, a 1-mm-wide area of an ion-implanted silicon wafer was annealed in a single scan. The experimental data are consistent with the extrapolation of solid-phase epitaxial regrowth rates to the calculated laser-induced temperatures.

PACS numbers: 51.80. - x, 44.90. + c

I. INTRODUCTION

Recently, the use of a scanning cw laser to anneal ion-implanted semiconductors has been reported by several authors.^{1,2} It has been shown that, in silicon, if the layer is driven amorphous by the implantation, the annealing mechanism is a solid-phase epitaxial regrowth which proceeds at rates comparable to those obtained for conventional thermal annealing.³ The function of the laser (or electron beam) in this case is simply to heat the implantation-damaged region to a high temperature (~ 1100 – 1200 °C) so that complete solid-phase regrowth of the entire damaged layer can occur during the dwell time of the laser (typically 1 msec). Because the annealing time is short and the implanted material is never melted in this process, diffusion of the implanted impurity is negligible during the annealing cycle.

To calculate recrystallization rates and a variety of other phenomena related to cw-beam annealing, it is necessary to know accurately the temperature distribution produced by the beam in the material being annealed. A formalism for calculating the temperature distribution produced by an irradiated beam has already been developed for the case of a stationary⁴ and moving⁵ circular beam, and calculations based on this formalism have been found to agree well with experimental data. However, there are a number of situations in which a ribbon beam with an elliptical rather than a circular cross section would be desirable. Such a beam could be modeled as having an elliptical profile which is narrow in the direction of the scan and large in the direction perpendicular to the scan. Such an intensity distribution can easily be obtained with a cylindrical lens. Moreover, any ratio between large and small axes of the elliptical beam can be achieved by using the correct set of spherical and cylindrical lenses. In view of its potential importance, we have calculated temperature profiles to be expected for beams having an elliptical cross section. In this paper we present these results as an aid to those who wish to explore the use of elliptical laser beams for heating and annealing experiments.

To minimize the amount of data to be presented, and to make the results valid for any kind of material, we present the calculations in two parts. We develop first an expression for the linear temperature rise induced by a moving elliptical

beam in a material that is assumed to have constant thermal conductivity. This calculation is based on the formalism proposed by Cline and Anthony. An analytical expression is obtained for the maximum temperature at the center of the moving beam, and a numerical integration is carried out to obtain all the relevant parameter dependences. A different approach, using the formalism developed by Lax,⁶ leads to the same maximum temperature rise.

We next present a more refined set of calculations that take into account the temperature dependence of the thermal conductivity. A Kirchhoff transform^{6,7} is used with experimental data on the thermal conductivity of Si⁸ and GaAs⁹ to obtain the "true" temperature profiles for these cases.

Finally, as an application of the results, we compare the theory with an experiment in which laser conditions were arranged so that lines of various widths could be annealed in a single pass of a cw Ar laser over an implantation-amorphized layer. The agreement between the theoretical predictions and the experimental data is found to be excellent.

II. SOLUTION TO THE HEAT EQUATION

We assume that the laser beam is elliptical in an (x, y) plane perpendicular to the direction of laser propagation (z). The ratio between the large axis (r_y) and the small axis (r_x) of the ellipse will be an important parameter in our analysis, defined as: $\beta = r_y/r_x$. We assume a Gaussian laser intensity distribution in both directions, \hat{x} and \hat{y} :

$$I = I_0 \exp(-x^2/2r_x^2) \exp(-y^2/2r_y^2). \quad (1)$$

I_0 can be determined as a function of the power absorbed by the material assuming an infinite surface:

$$I_0 = P(1 - R)/2\pi r_x r_y, \quad (2)$$

where P is the total incident power and R is the coefficient of reflection of the irradiated material. Finally, we write the energy absorbed in the solid if the beam is moving with the velocity v in the x direction:

$$Q = \frac{P(1 - R)}{2\pi r_x r_y} \exp\left(-\frac{(x - vt)^2}{2r_x^2} - \frac{y^2}{2r_y^2}\right) f(z). \quad (3)$$

In Eq. (3) $f(z)$ gives the z dependence of the total absorbed energy.

To solve the heat equation, we use a standard Green's function analysis. The source function for the heat equation,¹⁰

$$\frac{\partial T}{\partial t} - D \nabla^2 T = \frac{Q}{C_p} \quad (4)$$

is

$$G = G\left(\frac{x', y', z', t'}{x, y, z, t}\right) = \exp\left(-\frac{[(x-x')^2 + (y-y')^2 + (z-z')^2]}{4D(t-t')}\right) \times [4\pi D(t-t')]^{-3/2} \quad (5)$$

We define our coordinate axes in the following way:

$x = y = z = 0$ will be the center of the beam at the surface of the material, with the x and y axes lying at the surface of the material, pointing along the small and large axes, respectively, of the elliptical beam. The z axis is along the direction of propagation of the laser beam (i.e., perpendicular to the surface of the material).

$$\Theta = \frac{2P(1-R)}{C_p \pi^{3/2}} \int_{-\infty}^t \frac{1}{\{4D(t-t')[4D(t-t') + 2r_x^2][4D(t-t') + 2r_y^2]\}^{1/2}} \times \exp\left(-\frac{(x-vt')^2}{4D(t-t') + 2r_x^2} - \frac{y^2}{4D(t-t') + 2r_y^2} - \frac{z^2}{4D(t-t')}\right) dt' \quad (7)$$

In order to simplify the writing of this expression, we introduce the following dimensionless parameters:

$$X = x/r_x; \quad Y = y/r_x; \quad Z = z/r_x; \quad \beta = r_y/r_x;$$

and we define

$$p = [P(1-R)]/r_x, \quad V = vr_x/2D.$$

After the two successive changes of variables, $t'' = -t'$ and $u = (2Dt''/r_x^2)^{1/2}$, the linear temperature at $t = 0$ can be written:

$$\Theta = \frac{p}{C_p D} \frac{1}{\sqrt{2\pi^{3/2}}} \int_0^\infty \frac{1}{[(u^2 + 1)(u^2 + \beta^2)]^{1/2}} \exp\left[-\frac{1}{2}\left(\frac{(X + Vu)^2}{u^2 + 1} + \frac{Y^2}{u^2 + \beta^2} + \frac{Z^2}{u^2}\right)\right] du \quad (8)$$

We can now determine, analytically, the maximum linear temperature, obtained at the center of the ellipse ($X = Y = Z = 0$) for a stationary beam ($V = 0$). The integration leads to the following result:

$$\Theta_{\max} = \frac{p}{\beta C_p D} \frac{1}{\sqrt{2\pi^{3/2}}} K\left(\frac{\beta^2 - 1}{\beta^2}\right)^{1/2}, \quad (9)$$

where K is the complete elliptical integral of the first kind.

A similar result can be found by considering the elliptical beam as a superposition of circular beams. We can then write the intensity of an elliptical spot in the following way:

$$I_{\text{ellipse}}(x, y) = \int_{-\infty}^\infty I_{\text{circular}}(x, y - y') S(y') dy'. \quad (10)$$

We have to find the weighting function $S(y)$ so that the above

In the first step we are going to consider a constant thermal conductivity with respect to temperature which will lead to the linear temperature rise.

Making our observation at a time t at a point (x, y, z) , the linear temperature rise is as follows:

$$\Theta = \int_{-\infty}^t \int_{-\infty}^\infty \int_{-\infty}^\infty \int_{-\infty}^\infty (Q/C_p)(x', y', z', t') \times G(x', y', z', t'/x, y, z, t) dx' dy' dz' dt'. \quad (6)$$

The integration over the different variables can be done separately. The integrals over x' and y' are Gaussian tabulated integrals.

To make the integration over z' , we need to define the function $f(z)$ which expresses the penetration of laser energy into the material with respect to depth. Since in most cases of interest $\alpha^{-1} \ll r_x, r_y$, we choose $f(z)$ to be a δ function at the surface of the material. To account for the discontinuity at $z = 0$, we have carried out the integration over z' from $-\infty$ to $+\infty$, and then taken twice its value from mirror image considerations.

After carrying out the integration over x, y, z , the linear temperature is the following:

intensity distribution gives the correct elliptical intensity written earlier. An identification leads to:

$$S(y) = \left(\frac{1}{2\pi r_x^2(\beta^2 - 1)}\right)^{1/2} \exp\left(-\frac{y^2}{2r_x^2(\beta^2 - 1)}\right) \quad (11)$$

Using now the expression for the linear temperature for a circular beam presented by Lax,⁴ and realizing that the same weighting function will distribute the linear temperature, we have

$$\Theta_{\max} = \int_{-\infty}^\infty \Theta^{\text{circle}}(y') S(y') dy', \quad (12)$$

which leads to

$$\Theta_{\max} = \frac{P(1-R)}{C_p D r_x \beta \sqrt{2\pi^{3/2}}} K\left(\frac{\beta^2 - 1}{\beta^2}\right)^{1/2}, \quad (13)$$

or with our p notation:

$$\Theta_{\max} = \frac{p}{\beta C_p D} \frac{1}{\sqrt{2\pi^{3/2}}} K\left(\frac{\beta^2 - 1}{\beta^2}\right)^{1/2}, \quad (14)$$

which is identical to the result of Eq. (9).

This above result can be used to find the maximum temperature for a circular beam by setting $\beta = r_x/r_y = 1$, then

$$\Theta_{\max}^{\text{circle}} = p/C_p D 2\sqrt{2\pi}. \quad (15)$$

The analytical integration has now been carried as far as possible. To analyze the dependence of the actual temperature on beam and substrate parameters, a numerical integration must be performed. To make the results valid for any

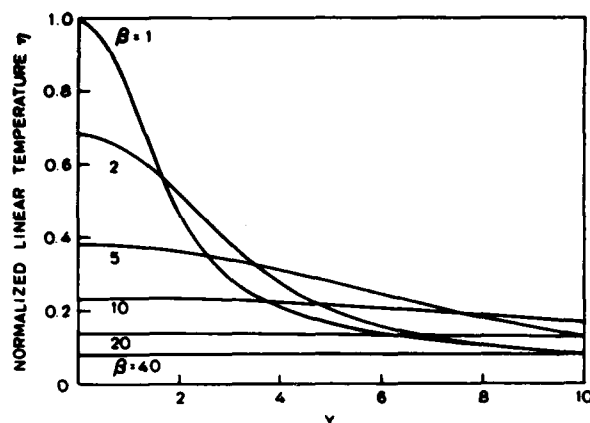


FIG. 1. Linear normalized temperature rise η at $X = Z = V = 0$ as a function of the Y position ($Y = y/r_s$) for different values of β ($\beta = r_s/r_s$) ranging from 1 to 40.

kind of material, we define the following quantity:

$$\eta = \frac{\theta}{\theta_{\max}^{\text{circle}}(\beta = 1)} = \frac{2}{\pi} \int_0^\infty \frac{du}{[(u^2 + 1)(u^2 + \beta^2)]^{1/2}} \times \exp\left[-\frac{1}{2}\left(\frac{(X + Vu^2)^2}{u^2 + 1} + \frac{Y^2}{u^2 + \beta^2} + \frac{Z^2}{u^2}\right)\right]. \quad (16)$$

III. CALCULATED NORMALIZED LINEAR TEMPERATURE CURVES

The numerical integration of Eq. (16) leads to a set of curves that can be chosen to cover a wide range of experimental conditions. A representative set of such curves is presented here. Figure 1 shows the linearized normal temperature η as a function of the Y ($Y = y/r_s$) position for different values of the ratio β ranging from 1 to 40. We see that large values of β give a more uniform temperature distribution. Under most experimental conditions, we cannot readily decrease r_s , so the only way to obtain high values of β is to increase r_y . A substitution of numbers shows that the power needed to reach an annealing temperature at high values of β

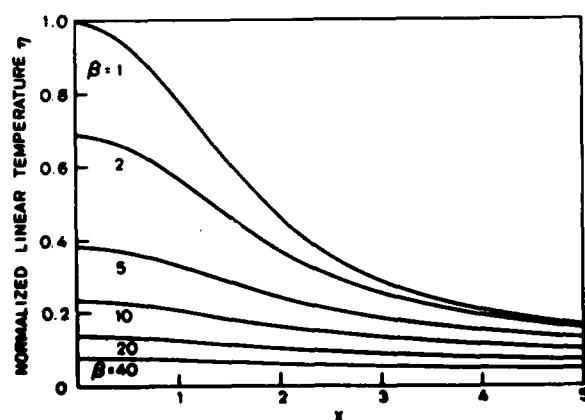


FIG. 2. Linear normalized temperature rise η at $Y = Z = V = 0$ as a function of the X position ($X = x/r_s$) for different values of β ($\beta = r_s/r_s$) ranging from 1 to 40.

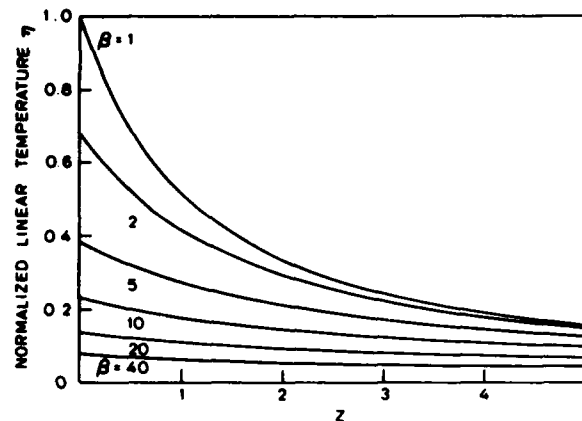


FIG. 3. Linear normalized temperature rise η at $X = Y = V = 0$ as a function of depth Z ($Z = z/r_s$) for different values of β ($\beta = r_s/r_s$) ranging from 1 to 40.

is very high, in fact, above the limit of currently practical cw Ar or Kr lasers, but certainly within the limits of an electron beam.

Similarly, in Figs. 2 and 3, the variations of η in the X ($X = x/r_s$) and Z ($Z = z/r_s$) directions are presented.

An extended scale in the Z direction has been taken in Fig. 4 (for $r_s = 20 \mu\text{m}$, the full scale represents $1 \mu\text{m}$). This curve shows clearly that the variations near the surface are insignificant and that, for instance, the temperature at the interface of an implanted layer in a semiconductor and underlying substrate is essentially the same as at the surface.

A similar study has been done using beam scanning speed as the parameter for two fixed values of β : $\beta = 1$ and $\beta = 20$. Figures 5 and 6 represent the variation η in the Y direction. Again, in Fig. 6, we can see that if we have enough power for annealing, high speed at $\beta = 20$ gives a uniform temperature distribution along the Y axis. Similarly, Figs. 7 and 8 represent the variations of η in the X direction. Since the beam is moving in this direction the nonsymmetrical behavior with respect to the point $X = 0$ appears clearly in

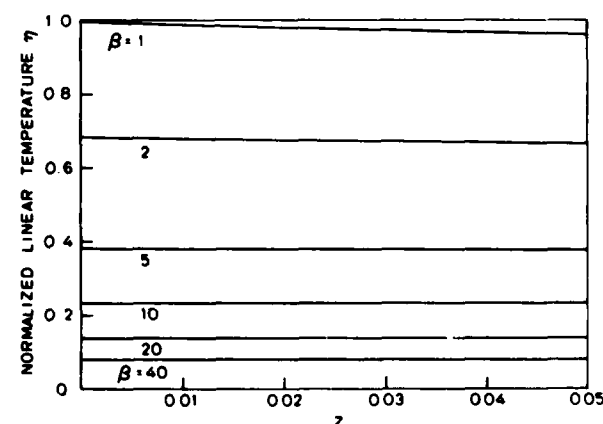


FIG. 4. Linear normalized temperature rise η at $X = Y = V = 0$ as a function of depth close to the surface Z ($Z = z/r_s$) for different values of β ($\beta = r_s/r_s$) ranging from 1 to 40.

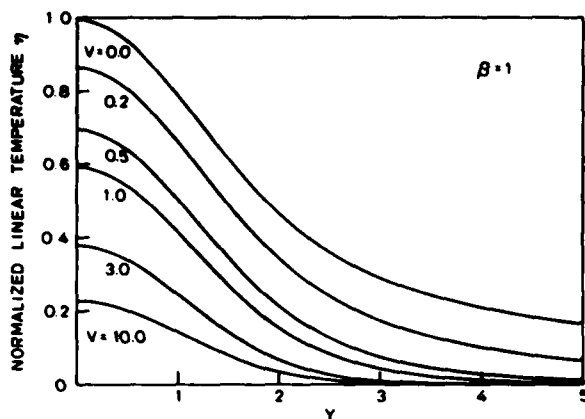


FIG. 5. Linear normalized temperature rise η at $X = Z = 0$ as a function of the Y position ($Y = y/r_s$) for different values of the normalized scan speed V ($V = vr_s/2D$) ranging from 0 to 10 and for $\beta = 1$ ($\beta = r_s/r_s$).

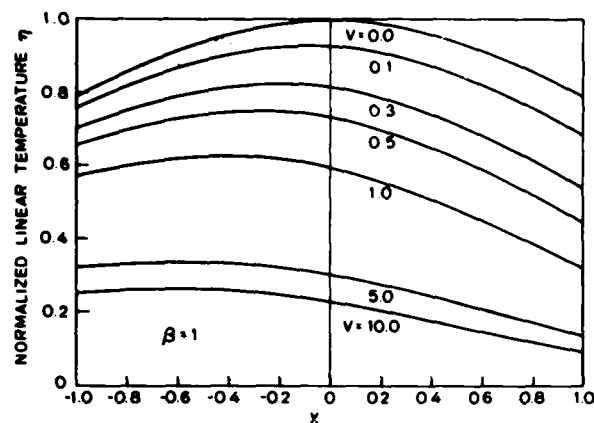


FIG. 7. Linear normalized temperature rise η at $Y = Z = 0$ as a function of the X position ($X = x/r_s$) for different values of the normalized scan speed V ($V = vr_s/2D$) ranging from 0 to 10 and for $\beta = 1$ ($\beta = r_s/r_s$).

these curves. Finally, the variation along Z in Fig. 9 shows again the weak changes of temperature as a function of depth into the material.

In order to allow the reader to use the curves for any combination of speed and ratio β , we have plotted the variation of η as a function of speed with β as a parameter in Figs. 10 and 11. Figure 11 emphasizes the fact that for the typical values of the speed used in a cw laser system, the solid easily reaches thermal equilibrium.

IV. THE TRUE TEMPERATURE RISE IN SILICON AND GALLIUM ARSENIDE

We are now ready to use the Kirchhoff transformation^{6,7} which leads to the true temperature rise induced by the laser beam. We have chosen to develop these calculations for silicon and gallium arsenide. The temperature-dependent thermal conductivity $K(T)$ has been taken from the literature.

We have been able to fit a rational function to the experimental data by using the form:

$$K(T) = C_p D(T) = A/(T - B). \quad (17)$$

Using this form the relation between the true and linear temperatures is then

$$T = B + (T_{\text{back}} - B) \exp\left(\frac{C_p D(T_{\text{back}})}{A} \theta\right), \quad (18)$$

where T_{back} is the temperature of the backsurface of the semiconductor.

For silicon we have averaged the experimental data in Ref. 8 to obtain values of: $A = 299 \text{ W/cm}$ and $B = 99 \text{ K}$. We have verified that a step-by-step numerical integration using published data for $D(T)$ gives a temperature profile which is essentially identical to that obtained using Eq. (17).

For gallium arsenide, we have used experimental data

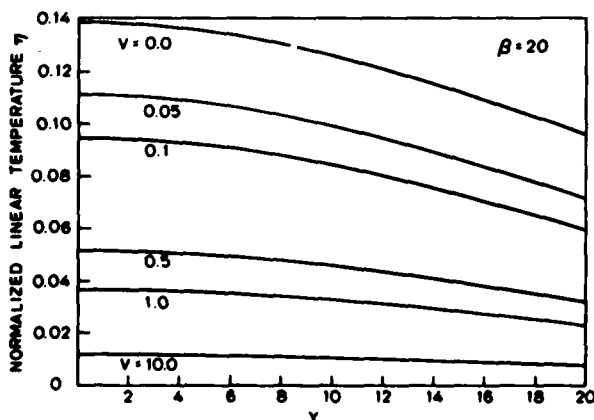


FIG. 6. Linear normalized temperature rise η at $X = Z = 0$ as a function of the Y position ($Y = y/r_s$) for different values of the normalized scan speed V ($V = vr_s/2D$) ranging from 0 to 10 and for $\beta = 20$ ($\beta = r_s/r_s$).

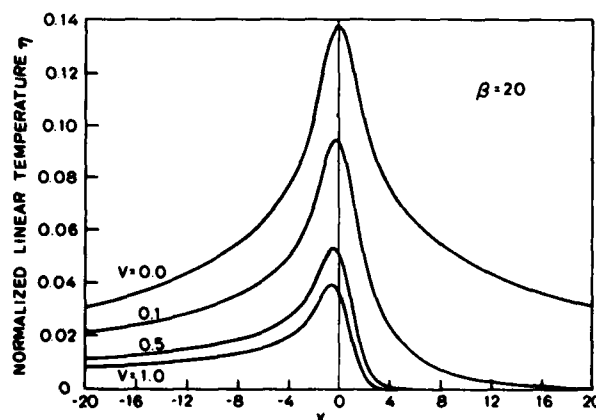


FIG. 8. Linear normalized temperature rise η at $Y = Z = 0$ as a function of the X position ($X = x/r_s$) for different values of the normalized scan speed V ($V = vr_s/2D$) ranging from 0 to 1 and for $\beta = 20$ ($\beta = r_s/r_s$).

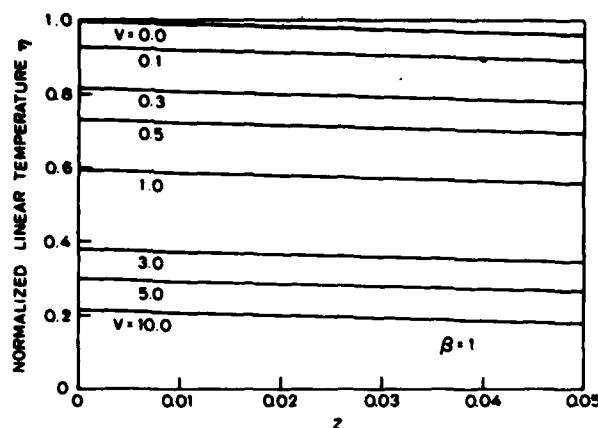


FIG. 9. Linear normalized temperature rise η at $X = Y = 0$ as a function of depth near the surface Z ($Z = z/r_s$) for different values of the normalized scan speed V ($V = vr_s/2D$) ranging from 0 to 10 and for $\beta = 1$ ($\beta = r_s/r_s$).

given by Maycock,⁹ which resulted in the following numbers: $A = 91$ W/cm and $B = 91$ K. Since no data are available above $T = 900$ K, we have extrapolated the behavior of $D(T)$ using the same function for higher temperature.

We are now able to obtain the real temperature as a function of p [$p = (1 - R)P/r_s$] for both silicon and gallium arsenide. Figures 12 and 13 present these variations (for $\beta = 1$) for silicon and gallium arsenide, respectively.

V. AN EXPERIMENTAL APPLICATION

The use of an elliptical laser beam to anneal gallium arsenide has already been reported.¹¹ Such a technique also offers the potential for annealing large areas of ion-implanted silicon in a single scan. Here we have used a 150-mm cylindrical lens to anneal (100) silicon which was arsenic implanted at 100 keV to dose of 6×10^{14} cm⁻². The lens employed produces a beam with $r_s = 18$ μ m and $\beta = 20$. The annealing parameters were as follows: beam power from 14 to 21 W, back-surface temperature of 550 °C, and scan rate of 1 cm/sec. The reflectivity of the material was mea-

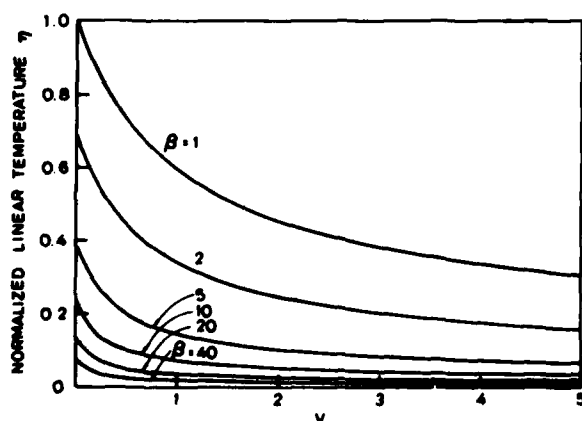


FIG. 10. Linear normalized temperature rise η at $X = Y = Z = 0$ as a function of the normalized scan speed V ($V = vr_s/2D$) for different values of β ($\beta = r_s/r_s$) ranging from 1 to 40.

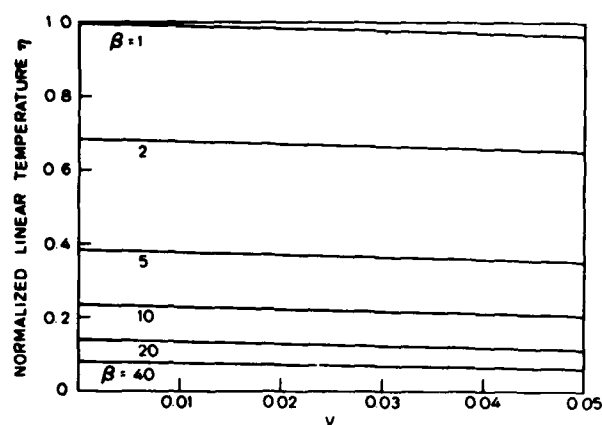


FIG. 11. Extended scale for the linear normalized temperature rise η at $X = Y = Z = 0$ as a function of the normalized scan speed V ($V = vr_s/2D$) for different values of β ($\beta = r_s/r_s$) ranging from 1 to 40.

sured at room temperature to be $R = 0.38$. Since no melting occurs we will assume R to be constant.

The first annealed area appears at $P = 14.5$ W, which corresponds to a calculated temperature of 967 °C. At $P = 17$ W we can see a line of width $d = 0.4$ mm, as shown in Fig. 14(a). At 21 W of incident power using the same scanning and back-surface temperature setting, we have been able to anneal a 1-mm-wide area, as shown in Fig. 14(b). We can compare these results with those to be expected from the temperature calculations just presented in the following way. First, we assume that the regrowth rate is described by the equation:

$$U = U_0 \exp(-E_a/kT), \quad (19)$$

in which $U_0 = 1.79 \times 10^{15}$ Å/sec and $E_a = 2.35$ eV, as determined by Csepregi and Kennedy.¹²

We have regrown a 1000-Å-thick amorphous layer. The dwell time is approximately $t = 1.7$ msec. The required regrowth temperature is then $T = 977$ °C. Figure 15 shows the temperature profile at the center of the beam ($T = T_{max}$) and at the edge of the beam ($Y = 20$) for our experimental conditions. Knowing that the beam is 1 mm wide we can estimate from this curve the regrown width for temperatures

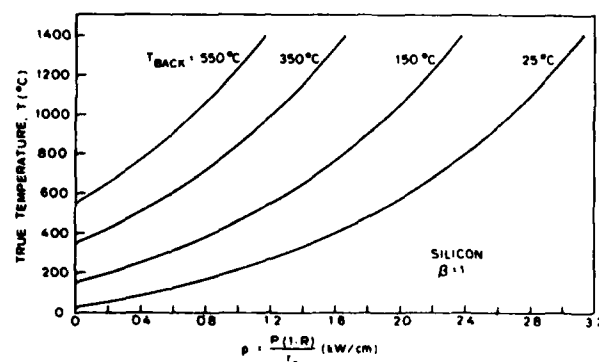


FIG. 12. The true maximum temperature ($X = Y = Z = V = 0$) in Si is plotted versus the normalized power p [$p = [P(1 - R)]/r_s$] for different substrate back-surface temperatures.

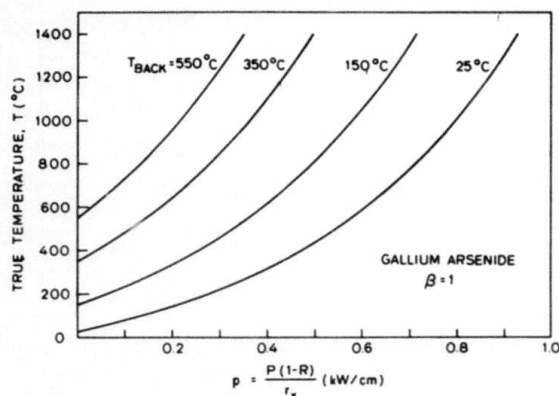


FIG. 13. The true maximum temperature ($X = Y = Z = V = 0$) in GaAs is plotted versus the normalized power p [$p = [P(1 - R)]/r_x$] for different back-surface temperatures.

larger than the calculated one. We can then evaluate that 40% of the beam width has been regrown at 17 W and 100% of the beam width at 21 W. This shows an excellent agreement with our experimental data.

CONCLUSIONS

These calculated results cover a wide range of experimental conditions and can be applied for a laser beam as well

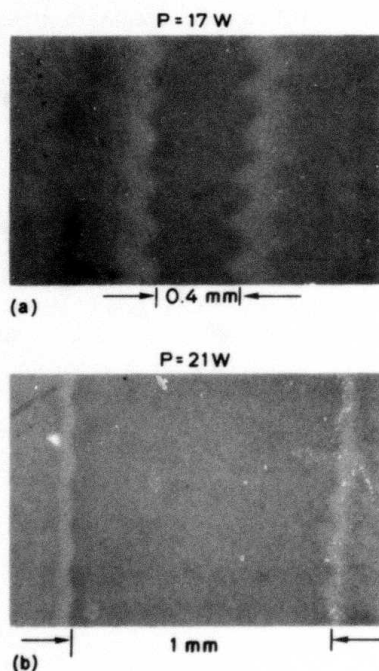


FIG. 14. Photomicrographs (55 \times) of laser-annealed line in silicon using a 150-mm focal length cylindrical lens at (a) $P = 17$ W and (b) $P = 21$ W, $T_{\text{back}} = 550^\circ\text{C}$, and $v = 1$ cm/sec. The waviness at the edge of the lines is due to the feedback of the laser working in a light controlled mode.

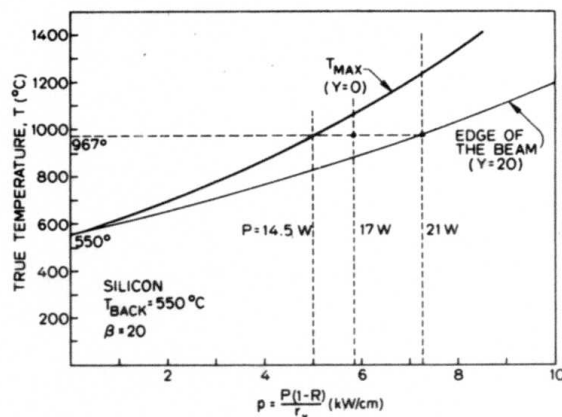


FIG. 15. The true temperature in silicon is plotted at the center of the beam, $Y = 0$, and at the Y edge of the beam, $Y = 20$, for $\beta = 20$ ($\beta = r_y/r_x$). With our experimental conditions, the temperature required for solid-phase epitaxial regrowth is indicated so that the expected width of an annealed line can be determined as a function of laser power. The 17- and 21-W points are shown.

as an electron beam. The calculated linear temperature is valid for any material. With knowledge of the temperature-dependent thermal conductivity, a simple transformation leads to the true temperature. The use of elliptical beam permits large areas to be laser annealed in a single scan. Furthermore, it has the advantage of producing the same annealing as a large radius circular spot will produce but with substantially less laser power.

ACKNOWLEDGMENTS

The authors are grateful to AROD (Grant No. DAAG29-78-G-0119), ARPA (Contract MDA903-78-C-0218), and to Dr. R. Reynolds for his continued interest and support.

- ¹G.A. Katchurin, E.V. Nidaev, A.V. Khodyachikh, and L.A. Kovaleva, *Sov. Phys.-Semicond.* **10**, 1128 (1976).
- ²A. Gat, J.F. Gibbons, T.J. Magee, J. Peng, V.R. Deline, P. Williams, and C.A. Evans, Jr., *Appl. Phys. Lett.* **32**, 276 (1978).
- ³A. Gat, A. Lietoila, and J.F. Gibbons, *J. Appl. Phys.* **50**, 2926 (1979).
- ⁴M. Lax, *J. Appl. Phys.* **48**, 3919 (1977).
- ⁵H.E. Cline and T.R. Anthony, *J. Appl. Phys.* **48**, 3895 (1977).
- ⁶W.B. Joyce, *Solid-State Electron.* **18**, 321 (1975).
- ⁷M. Lax, *Appl. Phys. Lett.* **33**, 786 (1978).
- ⁸C.Y. Ho, R.W. Powell, and P.E. Liley, *J. Phys. Chem. Ref. Data* **3**, Suppl. 1, I-588 (1974).
- ⁹P.D. Maycock, *Solid-State Electron.* **10**, 161 (1967).
- ¹⁰H.S. Carslaw and J.C. Jaeger, *Conduction of Heat in Solids*, 2nd ed. (Oxford U.P., New York, 1959).
- ¹¹J.C.C. Fan, J.P. Donnelly, C.O. Bozler, and R.L. Chapman, *Proc. 7th Int. Symp. On GaAs and Related Compounds*, St. Louis, 1978 (Institute of Physics, London, 1979), p. 472.
- ¹²L. Csepregi and E.F. Kennedy, *Proc. of the Symposium on Thin-Film Phenomena Interfaces and Interactions*, edited by J.E.E. Baglin and J.M. Poate (Electrochemical Society, Princeton, N.J. 1978), p. 77.

Calculation of solid-phase reaction rates induced by a scanning cw laser

R.B. Gold and J.F. Gibbons

Stanford Electronics Laboratories, Stanford, California 94305

(Received 27 August 1979; accepted for publication 8 October 1971)

An analytical model is presented for solid-phase reactions induced by a scanning cw laser. The results are applicable for both rate-limited reactions, such as the regrowth of implanted amorphous Si, and diffusion-limited reactions, such as the formation of metal silicides. The effect of the laser is interpreted in terms of a furnace anneal at an "effective temperature," T_{eff} , for an "effective time," t_{eff} . T_{eff} is shown to be equal to the maximum laser-induced surface temperature, while t_{eff} equals the laser dwell time multiplied by a "dwell-time reduction factor" which is a rational function of several material and annealing parameters and is typically on the order of $\frac{1}{3}$. A comparison of theory and experiment is made for the specific case of the formation of Pd_2Si .

PACS numbers: 82.40 — g, 61.80 — x,

Irradiation with a scanned cw laser has been shown to be an attractive alternative to conventional thermal processing for the annealing of the damage induced by ion implantation in semiconductors¹⁻³ and for the formation of metal silicides.⁴ In the first case, a model based on solid-phase epitaxial regrowth of the amorphous implanted layer has been proposed to account for the observed behavior.³⁻⁵ This model is supported by data obtained using *in situ* reflectivity³ and glancing-angle Rutherford backscattering,⁴ which show, respectively, the absence of the liquid phase and the presence of an intermediate partial regrowth stage. In addition, it has been shown that complete regrowth during the dwell time of a scanning laser beam^{3,4} as well as the diameter of the annealed region in a stagnant beam experiment⁵ are consistent with the extrapolation of epitaxial growth rates obtained from furnace-annealing experiments to the calculated laser-induced surface temperatures. A solid-phase reaction mechanism has also been proposed to explain the formation of Pd_2Si by a scanning cw laser.⁶

Although the solid-phase nature of these processes seems well established, an accurate analysis of reaction rate in the scanning-beam case has not yet been carried out. In a typical furnace anneal, the growth interface can be considered to be at a constant temperature throughout the duration of the anneal. This is not true for anneals by a scanning cw laser, however, since the temperature in this case is a rapidly changing function of time. We calculate here the expected laser-anneal regrown-layer thickness, including the dependence of temperature on time and assuming that the growth process can be described by a simple activation energy. The results of these calculations then permit a comparison of observed laser-anneal growth rates with extrapolated furnace-anneal data.

For a constant-temperature furnace anneal of amorphous implanted Si, the regrown-layer thickness can be expressed as

$$z = R_0 t \exp(-E_a/kT), \quad (1)$$

where t and T are the anneal time and temperature, respectively, and E_a is the activation energy. Pure (100) Si has been shown to have an activation energy of 2.35 eV and a value for the preexponential constant, R_0 , of 3.2×10^{14} Å/sec.⁷ For diffusion-controlled reactions, such as the for-

mation of metal silicides, the z in Eq. (1) is replaced by z^2 , but all other features of the following discussion are still applicable.

The strong dependence of temperature on time in the case of laser annealing means that we must replace Eq. (1) by

$$z = R_0 \int_{-\infty}^x \exp\left(\frac{-E_a}{kT(t)}\right) dt. \quad (2)$$

Liau *et al.*⁸ have shown that, for the case of irradiation by a laser pulse, Eq. (2) can be reduced to Eq. (1) by the determination of an "effective annealing temperature," T_{eff} , and an "effective annealing time," t_{eff} . While the technique of the present calculation is quite similar to that of Liau *et al.*, there are three major differences due to the nature of the temperature rise due to scanned cw laser irradiation:

(a) The maximum surface temperature, T_{max} , is a function of the ratio of absorbed power to spot radius, rather than the ratio of absorbed power to spot area.⁹ This is a consequence of the three-dimensional spreading of heat in the scanned case as opposed to the one-dimensional flow assumed in the pulse case.

(b) The temperature rise induced by a scanning cw laser reaches a constant value in times shorter than typical laser dwell times. The problem can thus be treated analytically as a steady-state temperature distribution in a moving frame of reference. The time dependence of the temperature at any given point is determined indirectly by $T(x)$ and $x(t)$, where x represents the distance from the beam center to the point of interest, rather than by an explicit $T(t)$.

(c) The thermal conductivity of Si exhibits a very strong temperature dependence.¹⁰ It is impossible to incorporate this effect into an analytical solution for the one-dimensional time-dependent case. It has been shown, however, that in the time-independent case, the true nonlinear temperature can be analytically related to the linear temperature rise, calculated assuming constant thermal conductivity, by means of the Kirchhoff transformation.^{11,12}

We assume that the spatial intensity distribution of the laser can be represented as $I = (P/\pi w^2) \exp(-r^2/w^2)$, where r is the distance from the center of the beam and P is the total absorbed power. For typical experimental conditions, both the laser beam penetration depth, $1/\alpha$, and the amorphous-layer thickness, z_0 , are much less than the Gaus-

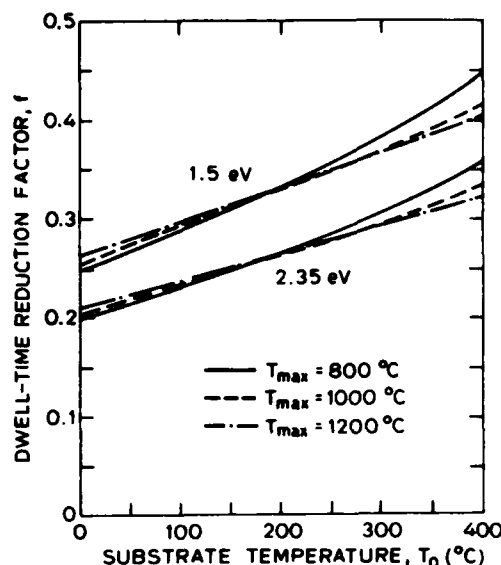


FIG. 1. Calculated dependence on T_0 and T_{\max} of the dwell-time reduction factor of Eq. (11c). The activation energies of 1.5 and 2.35 eV correspond, respectively, to the formation of Pd₂Si and the regrowth of implanted amorphous Si.

sian beam radius, w . The temperature at the regrowing-layer interface is thus essentially equal to the surface temperature calculated assuming a penetration depth of zero.

We stipulate furthermore that the beam is moving with a velocity v in the x direction, and that it is centered on the point of interest, (x, y) (0,0), at time $t = 0$. Using the results of Lax,⁹ the linear temperature rise $\theta(t)$ at this point can be shown to be

$$\theta(t) = \theta_{\max} \exp(-v^2 t^2 / 2w^2) I_0(v^2 t^2 / 2w^2), \quad (3)$$

Equation (6) can be used to eliminate θ , with the result

$$T(t) \approx T_{\max} \left(1 - \frac{v^2 t^2}{2w^2} \frac{(T_0 - T_k) \ln[(T_{\max} - T_k)/(T_0 - T_k)]}{T_{\max}} \frac{(T_{\max} - T_k)}{(T_0 - T_k)} \right) \quad (9a)$$

and

$$T_{\max} = T_k + (T_0 - T_k) \exp\left(\frac{P}{2\pi^{1/2} w A}\right). \quad (9b)$$

The expression for $T(t)$ can now be inserted into Eq. (2) to calculate the total regrown-layer thickness produced by a single scan through the point of interest. A final approximation, $T_{\max}(1-a) \approx T_{\max}/(1+a)$, justified as above, permits the integral to be solved analytically, yielding

$$z \approx R_0 \frac{2w}{v} \left(\frac{\pi k T_{\max}^2}{2E_a (T_{\max} - T_k) \ln[(T_{\max} - T_k)/(T_0 - T_k)]} \right)^{1/2} \exp\left(-\frac{E_a}{k T_{\max}}\right). \quad (10)$$

In a manner similar to that proposed by Liau *et al.*⁸ for the one dimensional long-pulse case, we interpret the growth predicted by Eq (10) as equivalent to a furnace annealing at an "effective temperature," T_{eff} , for an "effective time," t_{eff} , i.e.,

$$z \approx R_0 f_{\text{eff}} \exp\left(-\frac{E_a}{k T_{\text{eff}}}\right), \quad (11a)$$

where

$$T_{\text{eff}} = T_{\max} \quad (11b)$$

and

$$t_{\text{eff}} = \frac{2w}{v} \left(\frac{\pi k T_{\max}^2}{2E_a (T_{\max} - T_k) \ln[(T_{\max} - T_k)/(T_0 - T_k)]} \right)^{1/2} = \frac{2w}{v} f. \quad (11c)$$

where $I_0(x)$ is the modified Bessel function of order zero. The maximum linear temperature rise at $t = 0$ is given by $\theta_{\max} = (P/2\pi^{1/2} w K_0)$, where K_0 is the thermal conductivity at the wafer back-surface temperature, T_0 . This linear temperature rise, $\theta(t)$, is then related to the true temperature, $T(t)$, by the relation

$$\theta(t) = \int_{T_0}^{T(t)} \left(\frac{K(T')}{K_0} \right) dT'. \quad (4)$$

This expression can be numerically integrated using published thermal conductivity data for Si.¹⁰ However, we have found that an excellent fit to this data is obtained by the approximation

$$K(T) = A/(T - T_k) \quad (5)$$

with the constants A and T_k equal to 299 W/cm and 99 K, respectively, for Si. Equation (4) thus yields the following closed-form expression for $T(t)$:

$$T(t) = T_k + (T_0 - T_k) \exp[\theta(t)/(T_0 - T_k)]. \quad (6)$$

The results of Eqs. (3) and (6) can now be inserted into Eq. (2) and integrated to calculate the regrown-layer thickness. Since the growth rate is an extremely strong function of temperature, very little loss of accuracy is introduced¹³ by a first-order expansion of $\theta(t)$ near θ_{\max} ,

$$\theta(t) \approx \theta_{\max} - \theta_{\max} \left(\frac{v^2 t^2}{2w^2} \right). \quad (7)$$

The true temperature $T(t)$ is then approximately

$$\begin{aligned} T(t) &\approx T_{\max} - \theta_{\max} \left(\frac{v^2 t^2}{2w^2} \right) \frac{dT}{d\theta} \bigg|_{\theta_{\max}} \\ &= T_{\max} \left(1 - \frac{v^2 t^2}{2w^2} \frac{\theta_{\max}}{T_{\max}} \frac{dT}{d\theta} \bigg|_{\theta_{\max}} \right). \end{aligned} \quad (8)$$

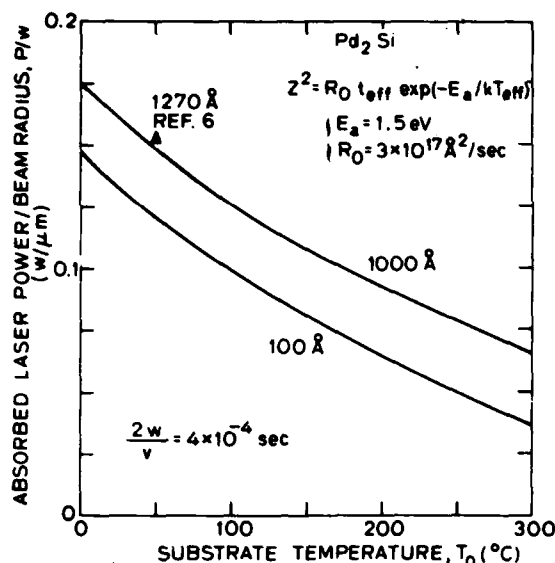


FIG. 2. Calculated combinations of absorbed laser power [$P_{\text{abs}} = P_{\text{inc}}(1 - R)$] and substrate temperature required to induce the formation of 100 Å and 1000 Å of Pd₂Si in a single scan. The effect of the dwell-time reduction factor is taken into account. Shown for comparison is the experimental data point of Ref. 6.

The effective time, t_{eff} , is equal to the laser-beam dwell time, $2w/v$, multiplied by a "dwell-time reduction factor," f . The calculated dependence of f on T_0 and T_{max} is shown in Fig. 1. It can be seen that the effective dwell time for an activation energy process is on the order of one-third the actual beam dwell time. The effect on f of laser power, and thus T_{max} , is minor; their effect on the total growth thickness is quite significant, however, due to the exponential term in the growth equation (11a).

As an example of the application of these results, we have calculated [using Eqs. (9b) and (11)] the combinations

of absorbed laser power and substrate temperature which should induce the growth of Pd₂Si layers with thicknesses of 100 and 1000 Å. These results are shown in Fig. 2; a laser-beam dwell time of 4×10^{-4} sec was assumed, corresponding, for instance, to a beam radius of 20 μm and scan speed of 10 cm/sec. The extremely strong dependence of thickness on laser power is evident. Also shown is the experimental data point of Ref. 6; it can be seen that good agreement between theoretical (1500 Å) and experimental (1270 Å) thicknesses is obtained.

The authors are grateful to ARPA (Contract MDA903-78-C-0128) for supporting this work, and to Dr. R. Reynolds for his personal interest.

¹A.V. Dvurechensky, G.A. Kachurin, T.N. Mustafin, and L.S. Smirnov, AIP Conf. Proc. **50**, 245 (1979).

²A. Gat, J.F. Gibbons, T.J. Magee, J. Peng, V.R. Deline, P. Williams, and C.A. Evans, Jr., Appl. Phys. Lett. **32**, 276 (1978).

³D.H. Auston, J.A. Golovchenko, P.R. Smith, C.M. Surko, and T.N.C. Venkatesan, Appl. Phys. Lett. **33**, 539 (1978).

⁴J.S. Williams, W.L. Brown, H.J. Leamy, J.M. Poate, J.W. Rodgers, D. Rousseau, G.A. Rozgonyi, J.A. Shelnutt, and T.T. Sheng, Appl. Phys. Lett. **33**, 542 (1978).

⁵A. Gat, A. Lietoila, and J.F. Gibbons, J. Appl. Phys. **50**, 2926 (1979).

⁶T. Shibata, J.F. Gibbons, and T.W. Sigmon, Appl. Phys. Lett. (to be published).

⁷L. Csepregi, E.F. Kennedy, J.W. Mayer, and T.W. Sigmon, J. Appl. Phys. **49**, 3906 (1978).

⁸Z.L. Liao, B.Y. Tsaur, and J.W. Mayer, Appl. Phys. Lett. **34**, 221 (1979).

⁹M. Lax, J. Appl. Phys. **48**, 3919 (1977).

¹⁰C.Y. Ho, R.W. Powell, and P.E. Liley, J. Phys. Chem. Ref. Data Suppl. **1**, 3, 1-588 (1974).

¹¹W.B. Joyce, Solid-State Electron. **18**, 321 (1975).

¹²M. Lax, Appl. Phys. Lett. **33**, 786 (1978).

¹³The regrown-layer thickness calculated from an exact numerical integration was within 1% of that obtained using the approximate result developed here.

A study of the mechanism of cw laser annealing of arsenic-implanted silicon

A. Gat, A. Lietoila, and J. F. Gibbons

Stanford Electronics Laboratories, Stanford, California 94305

(Received 8 June 1978; accepted for publication 13 September 1978)

In this paper we report on experiments designed to study the mechanism by which a continuous scanning laser anneals implantation-amorphized silicon. A stationary Ar laser beam was used to irradiate an As-implanted Si sample at constant power for different anneal times. The size of the annealed spot was found to increase with exposure time. The annealing spot size was also calculated for each exposure time by assuming the laser annealing mechanism to be a simple solid-phase epitaxial regrowth. Comparison of experiment and theory suggests that, at least for amorphous layers, the cw laser simply heats the substrate to a temperature where solid-phase epitaxial regrowth can occur quickly.

PACS numbers: 79.20.Ds, 61.80.Jh, 81.40.Ef, 68.55.+b

I. INTRODUCTION

Recently a number of authors¹⁻⁸ have reported on the use of laser irradiation for annealing ion-implanted silicon. The laser systems used for this work can be broadly divided into two classes: those utilizing a pulsed laser output and those using a scanned cw laser output.

The pulsed system¹⁻⁶ utilizes a high-power Q-switched laser (either ruby or Nd : YAG) operated at energy levels on the order of 1–2 J/cm² per pulse in the case of ruby and 5–10 J/cm² per pulse when Nd : YAG is used. This energy is supplied in a 50-MW/cm² 20-ns pulse and succeeds in melting the silicon to a depth of ~ 0.5 – $1.0 \mu\text{m}$.^{5,6,9}

The molten layer then freezes epitaxially on the underlying substrate. The implanted impurities diffuse rapidly through this molten layer with the result that they are distributed essentially uniformly over the recrystallized region.

In contrast to this behavior, the scanning cw laser system has been shown to anneal the implanted impurities directly into their As-implanted sites; i.e., there is essentially no diffusive redistribution, no evidence of melting and at the same time essentially perfect recrystallization.⁸

These results suggest that the mechanism of annealing for the scanning cw laser may be closely akin to a solid-phase epitaxial regrowth such as that described by Csepregi *et al.*¹⁰ In this paper we report on indirect measurements of the regrowth rate of amorphous layers obtained under conditions similar to those we have used in previously reported annealing experiments.^{7,8} Theoretical analysis shows that the data are consistent with the hypothesis that the annealing mechanism for our experimental conditions is a solid-phase epitaxial regrowth process.

II. EXPERIMENTAL

A test of the solid-phase epitaxy hypothesis requires calculating the temperature distribution in the implanted laser-irradiated sample. Cline *et al.*¹¹ show that, for a slowly moving beam, the instantaneous temperature distribution is

equivalent to the temperature distribution for a stationary beam. Since the scanning rates we employ are very small compared to the velocity of propagation of heat in silicon, we conclude that the annealing mechanism will be the same for a scanning beam as for a stationary beam. We have therefore chosen to study the annealing mechanism by irradiating the implanted silicon with a stationary beam and measuring the size of the annealed spot as a function of the exposure time.

We have used a cw argon laser (Spectra Physics Model 171-09) with a flat total reflector and a 6-m front output coupler. The output beam is focused by a 267-mm lens onto a sample holder positioned in the focal plane of this lens. The samples used were 10–20- Ω cm $\langle 100 \rangle$ p-type silicon wafers that were implanted with 3×10^{14} arsenic/cm² at 100 keV at room temperature. This dose and energy amorphize the first 800 Å of the silicon. The implanted sample was placed on the sample holder referred to above and heated to a temperature of $150 \pm \frac{1}{4}^\circ\text{C}$ prior and during laser irradiation.

The experiment was divided into two parts. First, the laser was used in the multiline mode. The sample was ex-

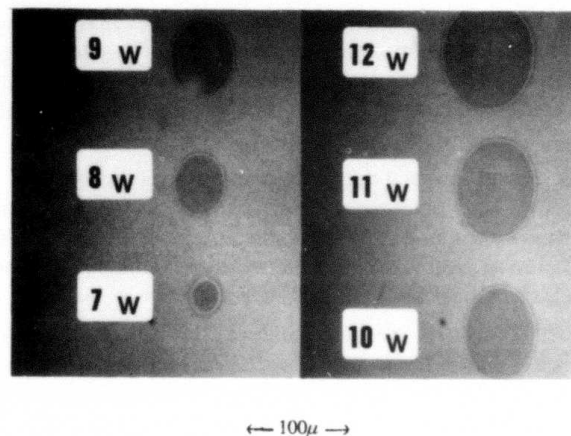


FIG. 1. Laser-annealed spots for constant exposure time and different power level.

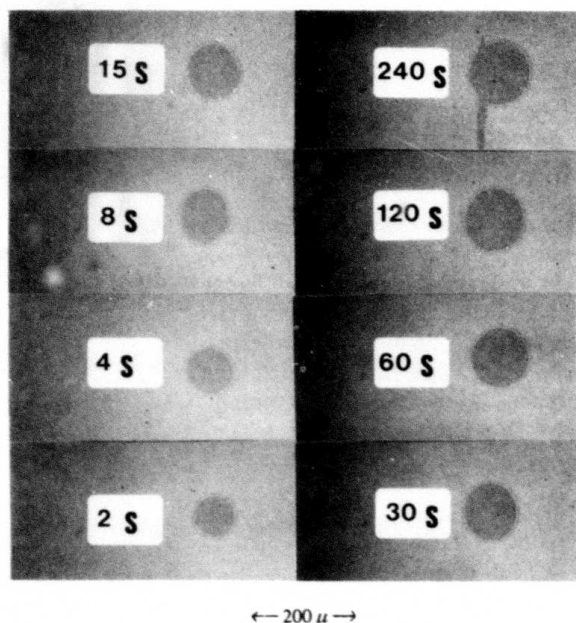


FIG. 2. Laser-annealed spots for constant power level of 7 W and different exposure time.

posed for a constant time of 8 s in each exposure, with the laser power being varied from 7 to 12 W in steps of 1 W. After each exposure the sample was moved upwards by 200 μ to avoid the overlap of spots annealed at different laser power levels.

Since the reflection coefficient of single-crystal silicon is lower than that of implantation-amorphized layers, the annealed single-crystal spots appear dark on a lighter background. The results of this experiment are given in Fig. 1. We have used this part of the experiment to calibrate the maximum temperature achieved in the laser-beam center.

In Fig. 1 the spot that results from a 11-W 8-s exposure, has only slip lines, while the 12-W spot shows distinctive damage in the center. We assume that this damage occurs because of melting and we can therefore set a power level of approximately 11.5 W as being the value at which the center of the beam reaches the melting point of the material. A reasonable assumption is that in our case the silicon has recrystallized before melting so we assume the melting temperature to be 1415 °C. This data will be used in the subsequent theoretical calculations.

In the second part of the experiment (performed on identically implanted samples) the laser was operated in the single-line mode at 5145 Å with a power level of 7 W. We used a single line to obtain better beam symmetry, and a spot size which is closer to the theoretical value.

The sample was exposed to the 7-W irradiation for different anneal times. As before, the sample was moved upwards after each exposure by 200 μ to avoid overlap of the annealed spots.

The results of this experiment are given in Fig. 2. The spot sizes were measured from Fig. 2 and are plotted as a

function of exposure time in Fig. 5. The slightly nonsymmetrical character of the spots arises from low-frequency drift in the laser output. This is one of the major reasons for the difference between experiment and theory.

The annealed spot size in the two parts of the experiment were measured optically based on the difference in the reflection coefficient between the single-crystal and the amorphous regions. To prove that the annealed dark region is crystalline Si, a TEM/TED study was carried out. Figure 3 shows diffraction patterns obtained from the annealed spot as well as from the nonexposed area. In all cases examined, single-crystal diffraction patterns were obtained within the annealed spots in contrast to amorphous diffraction patterns recorded outside of the anneal area.

The surface of the annealed spots was also examined by an ellipsometer to measure the thickness of a possible SiO₂ layer. No trace of any oxide was found which shows that, even with prolonged annealing times, cw-laser annealing does not cause the silicon surface to oxidize. This combined evidence indicates that the annealed spot is an oxide-free surface with single-crystal structure.

Comparison of Fig. 1 and 2 shows that there are differences between the multiline and single-line mode of operation. For example, the 7-W spot in Fig. 1 and the 8-s spot in Fig. 2 are different even though the anneal conditions are the same. We believe this is caused primarily by the difference in the laser beam width in the two modes of operation. To take this effect into account we have measured the beamwidths in the two modes. The beam-intensity distribution at the focal plane of the 267-mm lens was imaged with an 8-mm lens placed 8 mm away from the sample surface. After passing through this lens, the beam was projected on a screen 10 m away from the lens. The beam intensity (as a function of x and y) on the screen was measured using a photodiode and the distance between the $1/e$ points was taken as the beamwidth. This measurement was performed for both the multiline and single-line mode and its accuracy was estimated to be ~15%. Due to the inaccuracy in the absolute values of

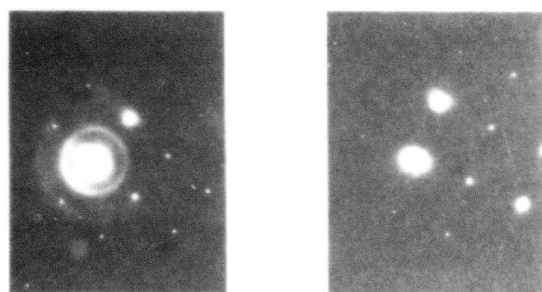


FIG. 3. TEM diffraction patterns from in and out of the annealed spot.

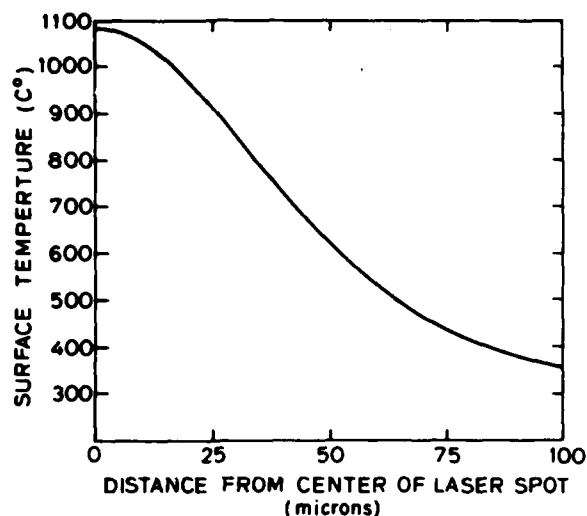


FIG. 4. Steady-state temperature distribution as a function of distance from the beam center for the 5145-Å line, power level of 7 W, and a laser-spot size of 37.3 μm .

this measurement, we have used only the ratio between the two cases, which is

$$\frac{w(\text{all lines})}{w(5145\text{-}\text{\AA}\text{ line})} = 1.21. \quad (2.1)$$

To obtain an absolute value of w for the single-line mode we have calculated the theoretical beam size from the laser mirrors and spacing specifications.¹² After passing through the 267-mm lens the calculated beam size is 37.3 μm .

III. THEORETICAL CALCULATIONS

In this paper, we would like to show that the recrystallization process responsible for the results above is consistent with the assumption that the regrowth mechanism is solid-phase epitaxy. The regrowth starts at the interface between the amorphous layer and the underlying single crystal. This process has been investigated by Csepregi *et al.*,¹⁰ and was found to have a well-defined activation energy of 2.3 eV. In the experiment described above we have obtained the dependence of the annealed spot size on exposure time. To explain this behavior in terms of the proposed model, we must first calculate the temperature distribution in the laser-illuminated silicon sample as a function of r , the distance from the beam center. Clearly the temperature will decrease monotonically with r . For each point in the radial coordinate, we associate a growth rate determined by its temperature. Given the exposure time we then look for the maximum radius r_{max} at which the temperature is sufficient to completely regrow the amorphized layer in the given exposure time. This r_{max} is the theoretical radius of the annealed spot. (As a practical matter, it was found easier to reverse the order and calculate the required exposure time for given r_{max} .)

A. Temperature distribution

The calculation of the temperature distribution is based on a paper by Lax.¹¹ He deals with the steady-state tempera-

ture distribution in a semi-infinite sample. The sample is assumed to have a constant thermal conductivity and the laser beam is assumed to be radially symmetric.

We assume Lax's conditions to be valid for our case. A steady state is obviously achieved, at least for the longer exposure times. The sample can be considered semi-infinite since its dimensions are large compared with the beamwidth. The ambient temperature is the back-surface temperature, 150 °C. The beam is assumed to have an intensity distribution given by

$$I = I_0 \exp(-r^2/w^2), \quad (3.1)$$

where w is the beamwidth parameter and r is the distance from the beam center. The weakest assumption for our application is that of constant thermal conductivity since for silicon the thermal conductivity is approximately proportional to $1/T$, when $T > 450$ K. This will probably be the main source of error in the temperature calculations that follow, though our experimental procedure is designed to minimize the error by using an appropriate temperature-calibration technique.

In Ref. (13), the temperature rise ΔT is shown to be

$$\Delta T = \Delta T_{\text{max}} N(r, z, w), \quad (3.2)$$

where

$$\Delta T_{\text{max}} = \frac{1}{2} P (1 - R) / (\pi)^{1/2} K w, \quad (3.3)$$

K is the thermal conductivity, z is the depth, P is the total incident power, and R is the reflectivity. The function N is normalized to have a maximum value of unity. For the surface, $z = 0$, $N(r, 0, w)$ will be

$$N(r, 0, w) = \frac{w\alpha}{\pi^{1/2}} \int_0^\infty \frac{J_0(\pi r/w) \exp(-\frac{1}{4}\pi^2 \tau^2)}{\alpha w + \tau} d\tau, \quad (3.4)$$

where α is the absorption coefficient for the laser irradiation and J_0 is the zero-order Bessel function of the first kind.

ΔT_{max} cannot be calculated directly from Eq. (3.4) because K is not constant. Therefore, the actual maximum temperature rise will be determined on the basis of the first part of the experiment, annealing for a constant time at different power levels. As indicated there, we have chosen 11.5 W to be the laser power level at which the temperature in the center of the spot is 1415 °C. This estimate can then be used to evaluate the maximum temperature rise in the second part of the experiment, where we used the 5145-Å line at the constant power of 7 W. According to Eq. (3.2), ΔT_{max} is linearly proportional to P and inversely proportional to w . We have measured the ratio between beamwidths in the two parts of the experiment (multiline, 5145-Å line). This ratio is given by Eq. (2.1). The ratio between powers in these two cases is 11.5/7. Recalling that the substrate is held at 150 °C, we then obtain for the actual maximum temperature of the sample

$$T_{\text{max}}(7\text{W}, 5145\text{-}\text{\AA}\text{ line}) = 1082^\circ\text{C}. \quad (3.5)$$

The next step in the calculation is to evaluate Eq. (3.4) which gives the temperature distribution as a function of r . To do this, we use α of Si for 5145 Å, $11\,800\text{ cm}^{-1}$, and the

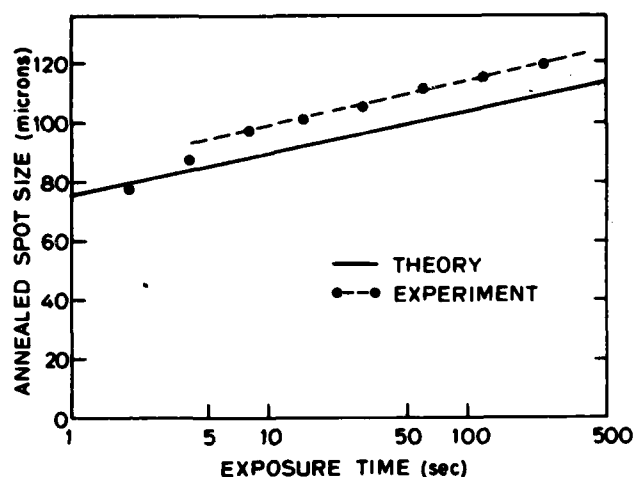


FIG. 5. Experimental and theoretical annealed spot sizes for 5145-Å line 7 W and different exposure time.

calculated value of w , $37.3 \mu\text{m}$.¹² The final surface-temperature profile is given in Fig. 4.

B. Epitaxial growth rate and theoretical spot size

We have used the following equation from Ref. (10) for the epitaxial growth rate v as a function of temperature:

$$v = 1.55 \times 10^{14} \exp[-2.3 \text{ eV}/kT(r)] \quad (\text{\AA}/\text{s}). \quad (3.6)$$

For further calculations we assume the temperature of the amorphous layer to be independent of depth. To verify this assumption, the temperature difference between the surface and a point 800 Å deep into the silicon was calculated using a very low value (0.02 W/cm °C) for the thermal conductivity of amorphous silicon. This temperature difference (across the layer) was found to be less than 0.5 °C.

For a given annealed spot radius we can calculate the required exposure time by dividing the amorphous-layer thickness, 800 Å, by the growth rate at the edge of the annealed spot. The result, together with the experimental data, is presented in Fig. 5, where we give the spot size versus annealing time. For the exposure times employed, the theoretical spot diameter is approximately linearly dependent on the log of the annealing time (this is not true for shorter exposure times).

IV. DISCUSSION AND CONCLUSIONS

In spite of some rather crude approximations made in the calculations above, the experimental and theoretical spot sizes match to within 10% over the entire range of exposure times. Alternately, the corresponding growth rate obtained in this work is within a factor of 2–3 (larger) than the published solid-phase epitaxial regrowth rates.

The difference between theory and experiment can be explained by several factors, among which are inaccuracy in the maximum temperature at the center of the spot and uncertainty in the laser beamwidth. Hence, the model based on solid-phase epitaxy gives a reasonable explanation of anneal-

ing behavior when a cw laser is used. This explanation is consistent with other data we have obtained, including both the absence of redistribution of implanted impurities during the process, and TEM studies which give evidence of a regrowth process that starts from the interface of the amorphous and crystalline silicon.¹⁴

Based on the data presented above, we concluded that conventional solid-phase epitaxial regrowth can occur when implanted amorphized silicon is annealed by a scanned cw laser. Since the temperature involved is relatively high, the short time (of the order of 1 ms) that it takes for a laser beam to move a distance equal to its spot size is enough to allow complete regrowth of the amorphous layer but insufficient to permit significant diffusion of the implanted impurities. Hence, the main effect of the laser radiation is to supply the energy needed to raise the temperature of the material that is being annealed.

In conclusion, we want to point out the sensitivity of our model to the temperature profile in the sample. Increasing the maximum temperature at the center of the spot from 1080 to 1182 °C increases the spot size by 10%. In contrast, the model is insensitive to the preexponential term in the growth rate, Eq. (3.6). Tripling this term increases the calculated spot size by only 10%. Therefore, an ionization enhancement of the growth rate can neither be verified nor ruled out. Another factor which effects the preexponential growth rate constant is type and concentration of impurities. We believe that this effect is neutralized by the high density of electron-hole pairs generated by the incoming radiation which tend to shift the Fermi level to midgap independent of sample doping.

ACKNOWLEDGMENTS

The authors would like to thank Dr. T. Magee and Dr. J. Peng (ARACOR) for the TEM study and its interpretation.

- ¹G.A. Kachurin, N.G. Predachin, and L.S. Smirnov, *Sov. Phys.-Semicond.* **9**, 916 (1975).
- ²E.I. Shtyrkov, I.G. Khaibullin, M.M. Zavipov, M.F. Galyatudinov, and R.M. Bayazitov, *Sov. Phys.-Semicond.* **9**, 1309 (1975).
- ³A. Antonenko, N.N. Gerasimenko, A.V. Dvurenchenski, L.S. Smirnov, and G.M. Tseitlin, *Sov. Phys.-Semicond.* **10**, 81 (1976).
- ⁴R.T. Young, C.W. White, G.J. Clark, J. Narayan, W.H. Christie, M. Murakami, P.W. King, and S.D. Kramer, *Appl. Phys. Lett.* **32**, 139 (1978).
- ⁵G.K. Celler, J.M. Poate, and L.C. Kimerling, *Appl. Phys. Lett.* **32**, 464 (1978).
- ⁶H.J. Leamy, G.A. Rozgonyi, T.T. Sheng, and G.K. Celler, *Appl. Phys. Lett.* **32**, 535 (1978).
- ⁷A. Gat and J.F. Gibbons, *Appl. Phys. Lett.* **32**, 142 (1978).
- ⁸A. Gat, J.F. Gibbons, T.J. Magee, J. Peng, V.R. Deline, P. Williams, and C.A. Evans, *Appl. Phys. Lett.* **32**, 276 (1978).
- ⁹J.C. Wang and R.F. Wood, *Am. Physical Soc., Washington meeting*, 1978 (unpublished).
- ¹⁰L. Csepregi, J.W. Mayer, and T.W. Sigmon, *Appl. Phys. Lett.* **29**, 92 (1976).
- ¹¹H.E. Cline and T.R. Anthony, *J. Appl. Phys.* **48**, 3895 (1977).
- ¹²A.E. Siegman, *Introduction to Lasers and Masers* (McGraw-Hill, New York, 1971).
- ¹³M. Lax, *J. Appl. Phys.* **48**, 3919 (1977).
- ¹⁴T.J. Magee, J. Peng, A. Gat, and J.F. Gibbons (unpublished).

Physical and electrical properties of laser-annealed ion-implanted silicon

A. Gat and J. F. Gibbons

Stanford Electronics Laboratories, Stanford, California 94305

T. J. Magee and J. Peng

Advanced Research and Applications Corp., Sunnyvale, California 94086

V. R. Deline, P. Williams, and C. A. Evans, Jr.

School of Chemical Science, Materials Research Laboratory, University of Illinois, Urbana, Illinois 61801

(Received 10 October 1977; accepted for publication 15 November 1977)

The use of a laser as a tool for annealing of ion-implantation damage is described. The principal results obtained are as follows: (1) electrical measurements show that activity comparable to that of a 1000°C 30-min anneal can be obtained; (2) TEM measurements show that complete recrystallization of the damaged layer occurs during the laser anneal; (3) impurity profiles obtained from SIMS measurements show that the dopant atoms remain in the LSS profile during annealing. Simple diodes were fabricated to examine the feasibility of the method for device fabrication.

PACS numbers: 61.80.Jh, 81.40.Rs

When ions are implanted into a crystalline target, a region near the surface of the target is damaged, and in some cases driven totally amorphous. For the majority of device applications some process of annealing is needed to restore the perfection of the crystal.

Several authors¹⁻⁵ have reported on the use of pulsed ruby and Nd-YAG lasers for annealing of ion-implantation damage in semiconductors. Klimenko *et al.*⁶ also deal with annealing by radiation at low power density for a long period of time. Kachurin *et al.*⁷ describe a mechanical laser scanner for a continuous argon ion beam and show that high electrical activity of the annealed layers can be obtained.

In a more recent paper⁸ Gat and Gibbons describe an apparatus that can be used to synchronously scan a continuous laser beam across an ion-implanted sample. In this apparatus, the sample is placed in the focal plane of the system to assure uniformity of annealing across a given scan line on the sample. In this paper we describe the analysis of As⁺-implanted silicon samples that were annealed in this apparatus. The analysis to be presented is based on SIMS, TEM, SEM, spreading resistance, and *p-n*-junction diode measurements.

As⁺ was implanted at 100 keV to a dose of $5 \times 10^{14}/\text{cm}^2$ into a number of 2–4- Ω cm *p*-type {100} silicon samples. This dose is sufficient to drive the silicon amorphous to a depth of approximately 1000 Å. After implantation, several of the samples were subjected to a 1000°C 30-min thermal anneal in flowing N₂ to provide standards of comparison for the laser-annealed samples.

The laser-annealed samples were subjected to the annealing sequence described in Ref. 8. The system uses an Ar ion laser having its primary output at 4880 Å. A power level of 7 W was found to provide optimum annealing using a 79-mm lens to focus the beam on the surface of a thermally bonded implanted sample. The scan rate was 2.76 cm/sec, at which rate lines of width 22 μ m are annealed on each scan of the sample. The

spacing between adjacent scan lines can be controlled, permitting study of both overlapping and nonoverlapping scan geometries.

Laser-annealed samples in which adjacent scan lines were made to overlap by approximately 20% were profiled by the SIMS technique of Evans *et al.* using Cs⁺ as the primary ion beam.⁹ The crater developed during this process was approximately 100 μ m square, and therefore covered a number of the overlapped 22- μ m scan lines.

A comparison of results obtained from the laser-annealed and thermally annealed samples is given in Fig. 1. The most striking result of this measurement is that the laser-annealed impurity distribution is essentially identical to the theoretical impurity dis-

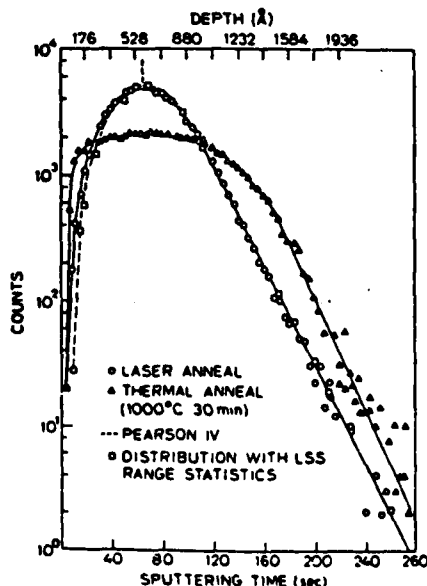
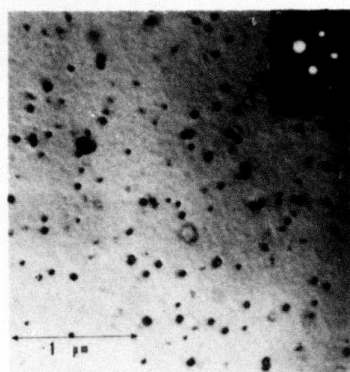


FIG. 1. As concentration profile in As-implanted silicon after laser anneal and thermal anneal.



(a)



(b)

FIG. 2. Electron micrographs of As-implanted silicon subjected to thermal anneal of 1000°C 30 min (a) and laser annealing (b); inserts show diffraction patterns which are typical to their regions.

tribution obtained using a Pearson type-IV distribution function with LSS range statistics.¹⁰ For comparison, the thermally annealed sample shows substantial diffusive redistribution of the As during the annealing cycle (as expected). The sheet resistance for both of the samples was 180 Ω/\square and corresponds to essentially 100% electrical activation of the implanted As⁺.

To study the structural quality of the recrystallization, TEM samples were prepared from conventionally annealed and laser-annealed samples. Samples containing overlapping or nonoverlapping scan lines were investigated in separate experiments. Figure 2 shows representative electron micrographs of As-implanted samples subjected to 1000°C 30-min thermal annealing [Fig. 2(a)] and laser annealing [Fig. 2(b)]. The thermally annealed sample contains a relatively high concentration ($\approx 10^{10}/\text{cm}^2$) of residual damage in the form of dislocation loops (≈ 300 Å average image diameter). In comparison, the concentration of defects in the laser-annealed samples is considerably reduced. In all of the laser-annealed samples, single-crystal diffraction patterns [left inset—Fig. 2(b)] were obtained within single and overlapping laser line scanned regions. The results indicate complete recrystallization and recovery from the amorphous state during laser exposure.

Of particular importance in Fig. 2(b) is the presence of a reasonably well-defined boundary between recrystallized and amorphous zones at the edge of the

laser scan line. The data have consistently shown an absence of thermal cracking and line defects both at the boundary and within laser scanned regions. Correlated SEM examinations also indicate no identifiable surface alteration or surface cracking on samples with overlapping and nonoverlapping scan lines. The results suggest that severe thermal gradients and/or stress-assisted secondary defect nucleation are either absent or sufficiently reduced under the laser exposure conditions described so as to escape detection by TEM. Additional TEM/SEM studies are currently in progress to further identify the nature of lattice reordering as a function of laser power density and exposure time.

Using standard photolithographic techniques, two sets of windows having the dimensions 1400 $\mu\text{m} \times 630$ μm and 770 $\mu\text{m} \times 425$ μm were cut in a 2400-Å-thick SiO₂ layer. As⁺ was then implanted through these windows under the conditions described above and an overlapping scan was employed to anneal the implanted area (without stripping the oxide mask). *I-V* characteristics for the 770- $\mu\text{m} \times 426$ - μm diodes formed in this way are shown in Fig. 3. The *I-V* characteristics may be fitted to the general formula $I = I_0 [\exp(qV/mkT) - 1]$ ^{11,12} by using $m = 1.5$ in the current range from 100 nA to ~ 10 μA and $m = 2.23$ in the current range 10 $\mu\text{A} < I < 3$ mA. Beyond 3 mA the *I-V* curve bends away from an $m = 2.23$ line due to excessive diode resistance.

The reverse breakdown voltage for these diodes was 35 V and the leakage current was 90 nA at -3 V. This relatively high leakage current and the nonideal forward characteristics may be related to effects which seem to occur in the Si under the oxide mask. Specifically, the Si underneath the oxide appeared to have been melted and regrown as a result of the laser anneal. This effect could arise if the oxide layer acted as both an (imperfect) antireflection coating and thermal insulating barrier so that the power absorbed into the semiconductor was greater than the critical energy needed to anneal the amorphous layer. In any event,

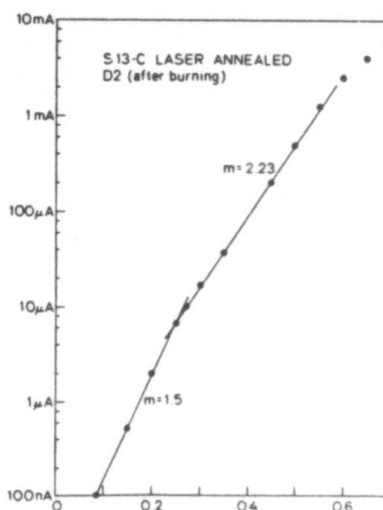


FIG. 3. Forward characteristics of As ion-implanted and laser-annealed diode in *p*-type silicon.

the perimeter of each diode was heavily damaged and is believed to be responsible for the nonideal I - V characteristics described above. Experiments are underway to test this hypothesis.

We conclude that a scanning continuous Ar ion laser is capable of completely annealing the amorphous layer of Si that is produced by a $5 \times 10^{14}/\text{cm}^2$ dose of As⁺ ions implanted at an energy of 100 keV. The electrical activity of the impurities in the annealed layer is essentially 100%, and the impurity profile is essentially identical to the as-implanted profile. TEM shows that inside a given scan line the dislocation loop density is less than that obtained for a thermal anneal, and no worse than a thermal anneal in the region where scan lines overlap. Residual damage may exist under oxide masks, but this can be minimized by using oxide masks of the proper thickness or metal masks.

The authors would like to acknowledge their indebtedness to Professor R. M. Swanson, Professor A. E. Siegman, and Professor R. Byers for helpful advice; to the National Science Foundation for support of the Stanford work; and to NSF CHE 76-03694 and DMR 76-01058 for support of the SIMS work. Partial support

for the TEM analysis was provided by Advanced Research and Applications Corporation.

- ¹B. A. Kachurin, N. B. Pridachin, and L. S. Smirnov, *Sov. Phys.-Semicond.* 9, 946 (1975).
- ²E. I. Shtyrkov, I. B. Khibullin, M. M. Zavipov, M. F. Galyatudinov, and R. M. Bayazitov, *Sov. Phys.-Semicond.* 9, 1309 (1975).
- ³A. Kh. Antonenko, N. N. Gerasimenko, A. V. Drvrenchenkii, L. S. Smirnov, and G. M. Tseitlin, *Sov. Phys.-Semicond.* 10, 81 (1976).
- ⁴V. V. Bolotov, N. R. Pricachin, and L. S. Smirnov, *Sov. Phys.-Semicond.* 10, 338 (1976).
- ⁵O. G. Kutukova and L. N. Stel'tsov, *Sov. Phys.-Semicond.* 10, 265 (1976).
- ⁶A. G. Klimenko, E. A. Klimenko, and V. I. Donin, *Sov. J. Quantum Electron.* 5, 1289 (1976).
- ⁷G. A. Kachurin, E. V. Nidaev, A. V. Khodyachikh, and L. A. Kovaleva, *Sov. Phys.-Semicond.* 10, 1128 (1976).
- ⁸A. Gat and J. F. Gibbons, *Appl. Phys. Lett.* 32, 142 (1978).
- ⁹P. Williams, R. K. Lewis, C. A. Evans, Jr., and P. R. Harley, *Anal. Chem.* 49, 1399 (1977).
- ¹⁰J. F. Gibbons, W. S. Johnson, and S. W. Mylroie, *Projected Range Statistics in Semiconductors* (Dowden, Hutchinson and Ross, Stroudsburg, Pa., 1975).
- ¹¹C. J. Kirchev, *J. Appl. Phys.* 46, 2169 (1975).
- ¹²C. J. Kirchev, *J. Appl. Phys.* 47, 5394 (1976).

Scanning-electron-beam annealing of arsenic-implanted silicon

J. L. Regolini,^{a)} J. F. Gibbons, T. W. Sigmon, and R. F. W. Pease

Stanford Electronics Laboratories, Stanford, California 94305

T. J. Magee and J. Peng

Advanced Research and Applications Corporation, Sunnyvale, California 94086

(Received 6 November 1978; accepted for publication 8 January 1979)

$\langle 100 \rangle$ Si implanted with As (100 keV, $10^{15}/\text{cm}^2$) was annealed with a scanning electron beam. The principal results obtained were (1) the electrical activity of the e-beam-annealed samples is the same as for control samples subjected to either cw laser annealing or thermal annealing at 575 and 1000°C, respectively, for 30 min each; (2) recrystallization of the implanted layer as determined by MeV ion channeling and TEM measurements is complete; (3) the electron distribution obtained by stripping and van der Pauw measurements indicates that no diffusion of the implanted atoms has occurred. The annealing is therefore essentially identical to that obtained with a scanning cw laser.

PACS numbers: 81.40.Ef, 41.80.Dd, 72.20. — i

Within the last year a number of research groups have shown that both Q -switched and scanned cw lasers can be used to anneal damage in Si created by ion implantation.¹⁻³ The annealing mechanism for the Q -switched case involves melting of the implanted layer, followed by a liquid-phase-epitaxial recrystallization process.^{2,4,5} For the scanning laser,¹⁻³ annealing proceeds by a solid-phase-epitaxial regrowth of the damaged layer.^{9,10} The important beam parameters that characterized the two processes are quite different, being energy density for the Q -switched case ($1-3 \text{ J}/\text{cm}^2$)¹¹ and the ratio of beam power to spot radius for the scanned laser ($\sim 0.2 \text{ W}/\mu$).¹⁰

Pulsed electron beams have also been used to anneal ion-implanted Si with results that are very similar to those found for the Q -switched laser, including particularly the threshold energy required for annealing.¹²

The parallelism of pulsed laser and pulsed e-beam results leads naturally to the question of whether a scanned electron beam with beam parameters similar to the cw laser can be used to anneal ion implant damage. The following

describes experimental results which confirm this parallelism exactly.

The amorphous Si layers were formed by implantation of ^{75}As ions into $\langle 100 \rangle$ $10\text{-}20\text{-}\Omega \text{ cm}$ p -type Si substrates held near LN₂ temperature. The total As dose was $1.5 \times 10^{15} \text{ cm}^{-2}$ and the implant energy was 100 keV. This dose and energy are sufficient to form an amorphous layer extending from the surface to a depth of about 1000 Å. The choice of ion, dose, and energy was dictated by reproducing earlier laser conditions and providing an electrically active impurity upon which MeV ion channeling and backscattering measurements can be easily made. After implantation the samples were mounted on a copper heat sink with Dow Corning 340 Heat Sink Compound and electron-beam annealed in a Hamilton Standard Electron Beam Welder Model EBW (7.5) at a working vacuum of 10^{-4} Torr.

Typical e-beam parameters used were 30 kV at 0.5 mA with the beam focused to a spot approximately 300μ in diameter at a distance 8 in. below the lowest surface of the final lens. The beam was scanned at a rate of $2.5 \text{ cm}/\text{sec}$. Both electrical and mechanical scanning were used with identical results. The beam parameters were chosen to closely ap-

^{a)}CONICET Fellow on leave from CNEA, Argentina.

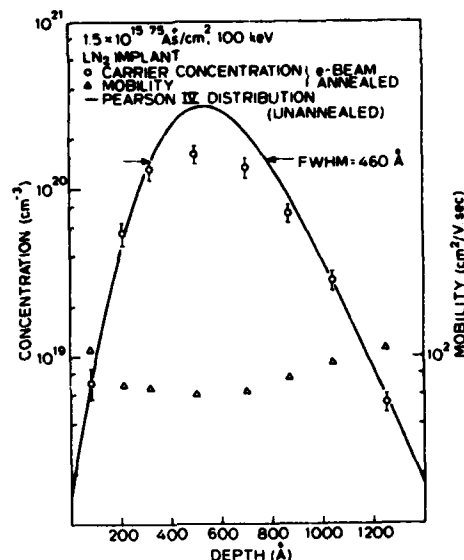


FIG. 1. Plot of electron concentration (No./cm³) and mobility (cm²/V sec) determined from differential van der Pauw measurements versus depth for e-beam-annealed 1.5×10^{15} As/cm² ion implant at 100 keV. Also shown is the theoretical profile expected for an unannealed sample.

proximate the power/radius (P/r) ratio and scan speed of the laser experiments. The temperature of the sample holder remained below 50 °C during the anneal. Large areas of annealed material were prepared for electrical and channeling measurements by overlapping the scanned lines, again similar to the techniques reported in the scanned laser case.

The annealed layers were first examined using Nomarski interference microscopy and were found to be 100–150 μm wide. Variation in the total e-beam current produced (a) no visible effects for $I_B \leq 0.3$ mA; (b) excellent annealing for $I_B \approx 0.5$ mA; (c) surface crazing for $I_B \approx 0.6$ mA; (d) thermal etching of the surface for $I_B > 0.6$ mA.

Electrical evaluation of the annealed layers was performed by measuring both sheet resistivity (using an ASR-100 spreading resistance probe¹³) and carrier concentration and mobility versus depth, using anodic stripping and van der Pauw measurements.

The spreading resistance measurements show a sheet resistivity that decreases from $10^3 \Omega/\square$ after implantation to $100 \Omega/\square$ after the e-beam anneal. This result is identical to results obtained on control samples that were annealed either thermally (1000 °C for 30 min in N₂) or with scanned Ar cw laser beam. No effects of the beam overlap on sheet resistivity were detected by the spreading resistance probe when the probe was stepped across these lines.

The results of the stripping and van der Pauw measurements are shown in Fig. 1 along with the Pearson IV¹⁴ distribution expected for this ⁷⁵As dose and energy implant. The stripping was calibrated by ellipsometric measurements of the anodic films. A Si-SiO₂ ratio of 0.56 was found to characterize this anodic oxidation process. Also shown is the electron mobility measured for each point. These mobility values are in excellent agreement with those found in bulk diffused Si¹⁵ and identical to the values obtained in cw laser-

annealed samples. The total number of electrons/cm² calculated from this figure is $1.02 \times 10^{15} \text{ cm}^{-2}$. The total dose, as measured by MeV backscattering techniques, was $1.5 \times 10^{15}/\text{cm}^2$, indicating that $\sim 33\%$ of the ⁷⁵As atoms are not electrically active.

In Fig. 2 we show data taken by 1.5-MeV ⁴He ion channeling and backscattering for samples subjected to a variety of annealing sequences. For the unannealed case the backscattering yield from the amorphous layer is characterized by a plateau with a high-energy step corresponding to scattering from the surface atoms (0.847 MeV) and a low-energy step corresponding to the interface between the amorphous and single-crystal Si. The thickness of the amorphous layer can be determined from the energy width of the plateau assuming bulk Si density and the measured stopping cross sections.¹⁶ The result is ~ 1000 Å. The total As dose can also be determined from this spectrum and is, using the near-surface approximation,¹⁷ $1.5 \times 10^{15} \text{ As/cm}^2$. The range and FWHM of the arsenic distribution can be estimated and are in excellent agreement with the results presented in Fig. 1.

The aligned spectra for the e-beam and thermally annealed samples show a large number of As atoms in nonsubstitutional lattice sites, $\sim 25\%$ for the e-beam and $\sim 30\%$ for the thermally annealed sample, in excellent agreement with the results obtained in the stripping measurements. The minimum yield at the surface for the $\langle 100 \rangle$ -aligned thermally annealed substrate is $\sim 5\%$, slightly higher than that of a perfect crystal. This result appears to be due to a residual damage region, possibly caused by oxygen knock-ons from the sample surface. The aligned yield on the e-beam-annealed samples is around 5% and the minimum yield is seen to increase more rapidly at lower backscattering energies than the thermally annealed samples, suggesting a greater

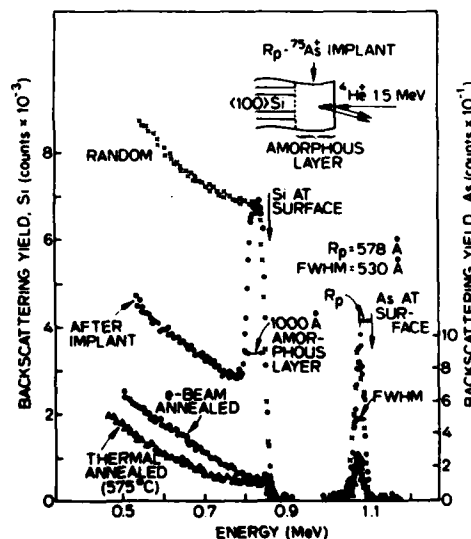


FIG. 2. Aligned spectra for 1.5-MeV ⁴He ions incident on $\langle 100 \rangle$ Si implanted with $1.5 \times 10^{15} \text{ As/cm}^2$ at 100 keV at LN₂ temperature. Spectra are shown for the unannealed, thermally annealed, and e-beam-annealed samples. A random spectrum is also shown for comparison.

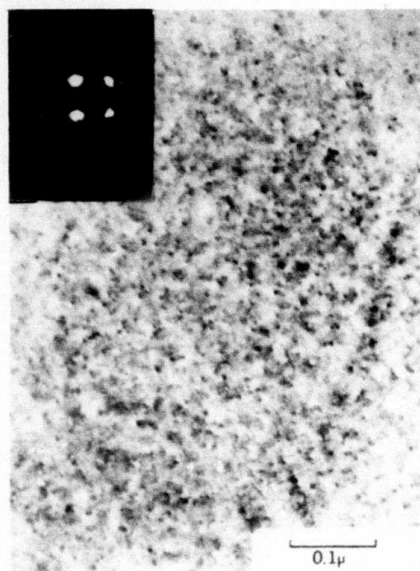


FIG. 3. TEM micrograph of e-beam-annealed ^{75}As implanted sample with selected area diffraction pattern.

number of residual defects remain in this layer. To clarify this point we performed TEM analysis.

In Fig. 3 we show a TEM micrograph for the e-beam-annealed layer. The selected area diffraction pattern (inset) indicates that complete recrystallization of the layer has occurred. However, the bright-field micrograph indicates that residual defects in the form of small dislocation loops (40–100-Å mean image diameter) remain. The average loop concentration was estimated from a number of micrographs to be $\sim 10^{14} \text{ cm}^{-2}$. Similar results were found in thermally annealed samples, leading us to believe that these loops might be associated with the surface peak observed in channeling data. Removal of $\sim 280 \text{ Å}$ of Si by anodic oxidation and stripping reduced the loop density by about an order of magnitude, verifying that these loops are associated with surface damage possibly due to knock-on of oxygen and/or carbon by the high-dose arsenic implant. After removal of the high concentration of loops, we observe a distribution of rodlike structures $\approx 500 \text{ Å}$ in average length that appear to be concentrated near the peak region of the ^{75}As distribution. These structures are seen in both thermal and e-beam-annealed samples.

^{75}As implanted $\langle 100 \rangle$ Si can be annealed with a scanning electron beam with results that are very similar to those obtained with a scanning cw laser, viz: (a) no redistribution

of the implanted dopant during annealing, suggesting that solid phase epitaxy is the annealing mechanism, (b) electrical activity of $\sim 70\%$ with 30% of the implanted atoms off axis, similar to both thermal and cw laser results for the ^{75}As dose used, and (c) essentially perfect recrystallization as measured by TEM, with evidence of clusters near the surface and rod-shaped defects near the peak of the impurity distribution.

We are pleased to acknowledge our indebtedness to G. Pauley and M. Gutierrez at the Stanford High Energy Physics Laboratory for assistance in using the electron-beam equipment; to J. Mayer for allowing us access to the Cal Tech backscattering facility; and to Dr. R. Reynolds, ARPA, for both his continued interest and financial support (Contracts DARPA MDA903-78-C-0128 and DARPA MDA903-78-C-0290).

¹G.A. Kachurin, N.G. Predachin, and L.S. Smirnov, *Sov. Phys.-Semi-cond.* **9**, 916 (1975).

²G. Foti, VIth Int. Conf. on Ion Beam Modification of Materials, Budapest (unpublished).

³R.T. Young, C.W. White, G.J. Clark, J. Narayan, W.H. Christie, M. Murakami, P.W. King, and S.D. Kramer, *Appl. Phys. Lett.* **32**, 139 (1978).

⁴G.K. Celler, J.M. Poate, and L.C. Kimerling, *Appl. Phys. Lett.* **32**, 464 (1978).

⁵H.J. Leamy, G.A. Rozgonyi, T.T. Sheng, and G.K. Celler, *Appl. Phys. Lett.* **32**, 535 (1978).

⁶A. Gat and J.F. Gibbons, *Appl. Phys. Lett.* **32**, 142 (1978).

⁷A. Gat, J.F. Gibbons, T.J. Magee, J. Peng, V.R. Deline, P. Williams, and C.A. Evans, Jr., *Appl. Phys. Lett.* **32**, 276 (1978).

⁸A. Gat, J.F. Gibbons, T.J. Magee, J. Peng, P. Williams, V. Deline, and C.A. Evans, Jr., *Appl. Phys. Lett.* **33**, 389 (1978).

⁹J.S. Williams, W.L. Brown, H.J. Leamy, J.M. Poate, J.W. Rodgers, D. Rousseau, G.A. Rozgonyi, J.A. Shelnutt, and T.T. Sheng, *Appl. Phys. Lett.* **33**, 542 (1978); D.H. Auston, J.A. Golovchenko, P.R. Smith, C.M. Surko, and T.N.C. Venkatesan, *Appl. Phys. Lett.* **33**, 539 (1978).

¹⁰A. Gat, A. Lietoila and J.F. Gibbons, *J. Appl. Phys.* (to be published).

¹¹G. Foti, E. Rimini, W.F. Tseng, and J.W. Mayer, *Appl. Phys.* **15**, 365 (1978).

¹²A.R. Kirkpatrick, J.A. Minnucchi, and A.C. Greenwald, *IEEE Trans. Electron Devices* ED-**24**, 429 (1977).

¹³J.F. Gibbons, J.L. Regolini, A. Lietoila, T.W. Sigmon, J.J. Magee, J. Peng, J.D. Hong, W. Katz, and C.A. Evans, Jr., *J. Appl. Phys.* (to be published).

¹⁴W.K. Hofker, D.P. Oosthoek, N.J. Koeman, and H.A.M. DeGrefte, *Radiat. Eff.* **24**, 223 (1975).

¹⁵S.M. Sze, *Physics of Semiconductor Devices* (Wiley, New York, 1969), p. 43.

¹⁶J.F. Ziegler and W.K. Chu, *At. Data Nucl. Data Tables* **13**, 463 (1974).

¹⁷J.W. Mayer and E. Rimini, *Ion Beam Handbook for Materials Analysis* (Academic, New York, 1977), Sec. 2.

PHYSICAL PROPERTIES OF ION-IMPLANTED SEM-ANNEALED SILICON

J. L. Regolini,¹ N. M. Johnson, and R. Sinclair²
Xerox Palo Alto Research Center
Palo Alto, California

T. W. Sigmon and J. F. Gibbons
Stanford Electronics Laboratories
Stanford, California

A detailed study has been conducted on the structural and electrical properties of ion-implanted silicon which has been annealed with a commercial scanning electron microscope (SEM), modified for high current operation. Electrical evaluation of the annealed layers included the measurement of sheet resistivity and depth profiles of the carrier concentration and mobility. Recrystallization of the implanted layers was evaluated by Rutherford backscattering techniques and transmission electron microscopy (TEM). The results presented here further substantiate previous findings that high-quality single-crystal layers can be obtained from SEM annealing of implanted amorphous layers on silicon.

I. INTRODUCTION

The annealing of arsenic-implanted silicon with a scanned electron beam in a modified SEM (Cambridge Stereoscan S-4) has recently been reported (1). It was demonstrated that the SEM features high-resolution annealing with the attainment of submicron areas of recrystallized silicon in implanted amorphous layers. The single crystal quality was evaluated from electron channeling patterns obtained from selected-area-diffraction scans in the SEM. The electrical activity and redistribution of the implanted species were studied by angle lapping and spreading resistance measurements. In this paper, we report an extended study of the structural and electrical properties of (100) Si implanted with As^+ , Si^+ and SiH^+ on a

¹Present Address: Centro Atomico, 840 Bariloche, Argentina.

²Stanford University, Consultant to the Xerox Corporation.

implanted with As^+ , Si^+ and SiH^+ on a bare surface, or through SiO_2 , and then SEM annealed. The system and annealing conditions were similar to those used in Ref. 1. Material characterization includes: (1) crystal perfection from Rutherford backscattering and TEM measurements and (2) dopant concentration and electron mobility from differential resistivity measurements with the van der Pauw configuration. Studies of electronic defect levels in scanned e-beam annealed silicon are reported elsewhere (4). The results from the present study are compared with those obtained with an e-beam welder (2) and by CW laser annealing (3).

II. EXPERIMENT

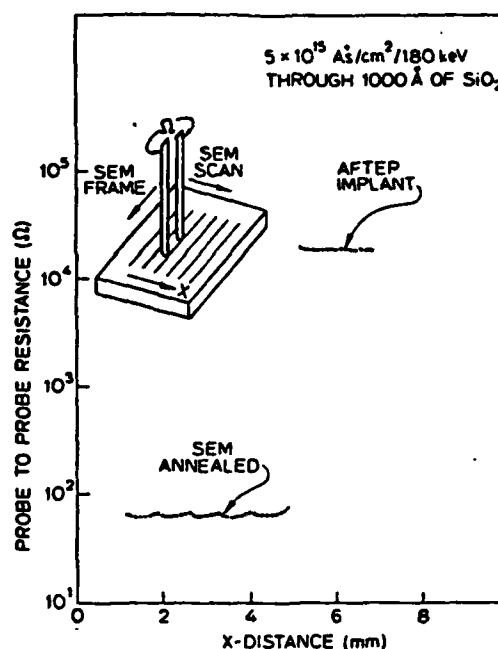
Typical annealing conditions were 20 kV at 50–70 μA , with a scanning speed of 10 cm/sec and a frame time of 40 sec for 1 mm. The working distance was 7 mm. Based on a theoretical analysis of transient annealing (5), it was estimated from measured values of melting and annealing powers that the power-per-unit radius for SEM annealing is 0.21 W/ μm , which yields a beam radius of $\sim 6 \mu\text{m}$.

Large areas of about $1 \times 1 \text{ cm}^2$ were obtained by overlapping scan-lines and frames. The annealed layers were first examined by Nomarski interference microscopy, which clearly revealed when melting occurred on a submicron scale. On the other hand, melting produces topographical changes such as pitting and piling which are readily detected in the SEM and from which the melting power can be determined for given working conditions.

III. RESULTS AND DISCUSSION

Spreading resistance measurements were used to test the lateral homogeneity of the annealed areas. Results are presented in Fig. 1. A (100) p-type silicon substrate was implanted with As^+ at 180 keV to a dose of $5 \times 10^{15} \text{ cm}^{-2}$ through 1000 Å of SiO_2 . After implantation the probe-to-probe resistance is over $10^4 \Omega$, and on the SEM-annealed region it is $\sim 70 \Omega$, consistent with recrystallization of the surface layer and electrical activation of the implanted dopant. The detectable periodic variation in resistance over the SEM-annealed area is due to a slight resistance variation over individual scan-lines. Over a scan distance of 1 mm (i.e., over the length on an individual scan-line) the resistance increases by $\leq 10\%$ from a minimum value at the midpoint, which corresponds to optimum anneal conditions, to larger values at the edges of the scan-lines. This variation is attributed to the effect on beam focus of the

FIGURE 1. Spreading resistance measurement on As^+ -implanted SEM annealed silicon.



finite radius of curvature of the scanned e-beam (6).

MeV ^4He -ion backscattering was used to study single-crystal quality and the substitutionality of implanted atoms. In Fig. 2 are shown data taken by 2.2 MeV $^4\text{He}^+$ ion channeling and backscattering on (100) silicon. The SEM-annealed specimen was first implanted with As^+ at 100 keV to a dose of $1.1 \times 10^{15} \text{ cm}^{-2}$, as measured by RBS. The spectrum for the SEM-annealed sample displays the same minimum backscattering yield at the surface as is obtained from an unimplanted control wafer ($\sim 4\%$). This reveals that the entire implanted amorphous layer has been recrystallized and is comparable in quality to the starting material, as determined by the oriented RBS technique. The minimum yield on the SEM-annealed sample is seen to increase more rapidly at lower backscattering energies than for the unimplanted one, suggesting that a number of residual defects remain in this layer. Also shown in Fig. 2 is the random spectrum which represents the yield for a completely amorphous target. The aligned spectrum for the SEM-annealed sample shows that $\sim 12\%$ of the implanted arsenic is in non-substitutional lattice sites.

In Fig. 3 are shown aligned spectra for self-implanted silicon. The spectrum for $10^{15} \text{ Si}^+ \text{ cm}^{-2}$ implanted at 40 keV with the substrate at LN_2 temperature is essentially identical to the aligned spectra shown in Fig. 2. However the higher yield and second disorder peak (after the surface peak) for the room

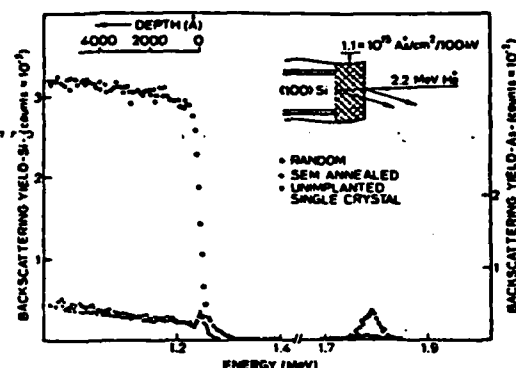


FIGURE 2. Aligned spectra for 2.2-MeV ^4He ions incident on (100) Si implanted with As^+ and SEM annealed.

temperature implant implies a higher level of residual damage after SEM annealing, as in thermal annealed samples after high temperature implantation (7).

Further electrical evaluation of ion-implanted SEM-annealed silicon was performed by differential resistivity with the van der Pauw technique combined with anodic oxidation for depth profiling. The measurement yields carrier concentration and mobility as shown in Fig. 4 for As^+ -implanted silicon. Also shown is the theoretical Pearson IV distribution (8) expected for the indicated As^+ dose and implantation energy. The total number of electrons/ cm^2 calculated from this figure is $9.6 \times 10^{14} \text{ cm}^{-2}$, and the total dose measured by RBS is $1.1 \times 10^{15} \text{ cm}^{-2}$, indicating that about 86% of arsenic is electrically active. Channeling measurements indicate that 12% of the implanted arsenic is in off-lattice sites. The measured mobility displays the same dependence on dopant concentration as found in bulk diffused silicon (9). The mobility is not degraded by defects as previously observed in As^+ -implanted-e-beam-annealed silicon where reduced mobilities were found at depths of 300 and 1200 Å (2).

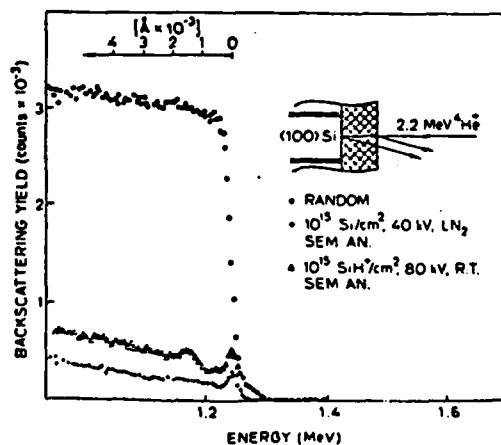


FIGURE 3. Aligned spectra for 2.2-MeV ^4He ions incident on self-implanted SEM-annealed silicon.

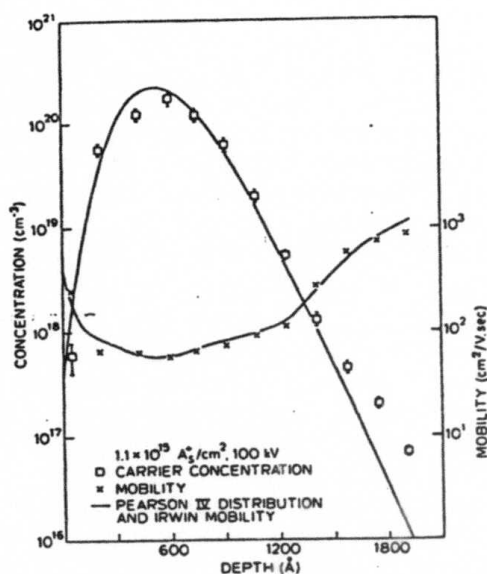


FIGURE 4. Electron concentration and mobility for As⁺-implanted SEM-annealed silicon.

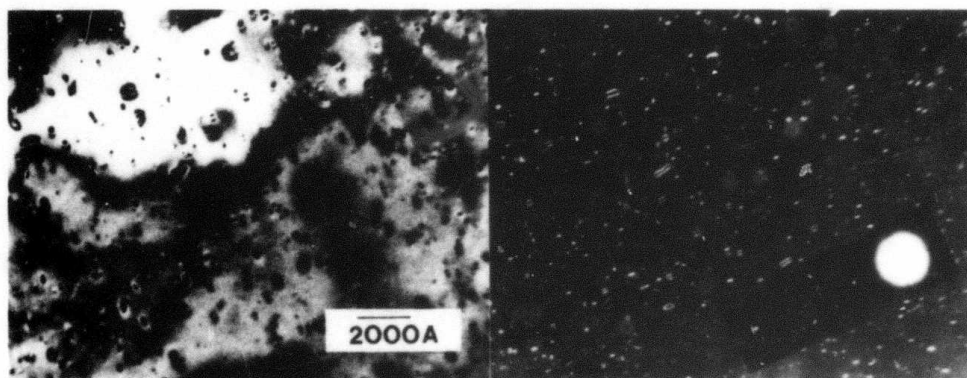


FIGURE 5. TEM micro-graphs for As⁺-implanted (100 keV, 1.1 × 10¹⁵ cm⁻²) SEM-annealed silicon: (a) bright-field image and (b) weak-beam dark-field image (g, 3g, s+ conditions) and electron diffraction pattern with spot sequence 000 (large spot), 220, 440, and 660.

In Fig. 5 are shown TEM micrographs for an As⁺-implanted SEM-annealed layer. The bright-field micrograph in Fig. 5(a) reveals the presence of dislocation loops in the recrystallized layer. In the lower right-hand quadrant, dislocation loops appear aligned with the direction of the scanned electron beam, which in this case is the [220] direction. The same region of the specimen is shown under weak-beam dark-field conditions in Fig. 5(b). The largest loops are ≤ 200 Å in diameter, and the estimated areal density of dislocation loops is 10^{10} cm⁻², which is significantly lower than that obtained with the e-beam welder (2). The insert in Fig. 5(b) shows the electron-diffraction conditions for the dark-field image; the sharpness of the Kikuchi line further confirms the high degree of crystallinity of the SEM-annealed layer.

The small spot size of ≤ 10 μm diameter achievable in the SEM, as compared to ~ 200 μm for the e-beam welder (2), appears to contribute to a more complete annealing of implanted amorphous layers on silicon with the attainment of high substitutionality and low residual damage as revealed by RBS and TEM.

ACKNOWLEDGEMENTS

The authors express their appreciation to K. N. Ratnakumar and R. F. W. Pease for helpful discussions on e-beam annealing. The work at Stanford University was partially supported by ARPA Contract MDA 903-78-C-0128.

REFERENCES

1. K. N. Ratnakumar, R. F. W. Pease, D. J. Bartelink, N. M. Johnson, and J. D. Meindl, *Appl. Phys. Lett.* **35**, 463 (1979).
2. J. L. Regolini, J. F. Gibbons, T. W. Sigmon, R. F. W. Pease, T. J. Magee, and J. Peng, *Appl. Phys. Lett.* **34**, 410 (1979).
3. J. L. Regolini, T. W. Sigmon, and J. F. Gibbons, *Appl. Phys. Lett.* **35**, 114 (1979).
4. N. M. Johnson, D. J. Bartelink, M. D. Moyer, J. F. Gibbons, A. Lietoila, K. N. Ratnakumar, and J. L. Regolini (this conference).
5. A. Lietoila (unpublished).
6. T. H. P. Chang and A. D. G. Stewart, 10th Symposium on Electron, Ion and Laser Beam Technology (San Francisco Press, Ltd, 1969).
7. L. Csepregi, E. F. Kennedy, S. S. Lau, J. W. Mayer, and T. W. Sigmon, *Appl. Phys. Lett.* **29**, 645 (1976).
8. W. K. Hofker, D. P. Oosthoek, N. J. Koeman, and H. A. M. De Grefte, *Radiat. Eff.* **24**, 223 (1975).
9. S. M. Sze, *Physics of Semiconductor Devices* (Wiley, New York, 1969), p. 43.

THE SOLUBILITY OF As IN Si AS DETERMINED BY THERMAL ANNEALING
OF METASTABLE, LASER ANNEALED CONCENTRATIONS

A. Lietoila, J. F. Gibbons, J. L. Regolini*, and T. W. Sigmon
Stanford Electronics Laboratories
Stanford, California 94305

T. J. Magee, J. Peng, and J. D. Hong
Advanced Research and Applications Corporation
Sunnyvale, California 94086

We demonstrate that cw laser annealing can activate implanted As in excess of $1 \times 10^{21} \text{ cm}^{-3}$. Concentrations above $3 \times 10^{20} \text{ cm}^{-3}$ are, however, metastable and relax to $3 \times 10^{20} \text{ cm}^{-3}$ or less during thermal annealing. The value to which the active concentration reduces depends solely on the furnace annealing temperature. The solubility of As in Si as a single, noncomplexed dopant is determined by laser annealing a metastable concentration and subjecting it to thermal equilibrium annealing at temperatures ranging from 700°C to 1000°C. MeV ion channeling measurements show that, while the As activation is decreasing due to thermal treatment, little change takes place in the amount of nonsubstitutional As-atoms. This suggests that the deactivation mechanism is a formation of complexes, which cause the As atoms to move off lattice sites only slightly. The rate of deactivation is thermally activated with an activation energy of 2.0 eV.

Introduction

The solubility of As in Si has raised many questions, since there is a disagreement between published solubility data and the maximum active concentration obtainable in practice. The solubility of As was originally published by Trumbore in 1960 (1), and it is $2 \times 10^{21} \text{ cm}^{-3}$ at around 1000°C. On the other hand, the maximum active concentration which can be achieved by diffusion or thermal annealing of ion implantation is only $3 \times 10^{20} \text{ cm}^{-3}$ (2).

It has been shown that, with scanning cw laser annealing, it is possible to activate As concentrations in excess of 10^{21} cm^{-3} (3,4). But it turns out that doping concentrations above $3 \times 10^{20} \text{ cm}^{-3}$ are metastable: a subsequent thermal annealing causes these concentrations to relax to $3 \times 10^{20} \text{ cm}^{-3}$ or less (4). The value to which the active concentration relaxes depends solely on the thermal annealing temperature. Thus it is possible to determine the solubility of As by implanting and laser annealing a metastable concentration and letting it relax to equilibrium using thermal annealing.

*Present address: Centro Atomico, 8400 Bariloche - R.N., Argentina

Before going to experimental results, we would like to stress that by solubility we mean the maximum concentration of As as a single, noncomplexed substitutional dopant. This paper does not aim to answer the question as to whether there is another solubility which would be higher than the above defined one and could be referred to as the chemical solubility.

1. Sample Preparation

Arsenic was implanted at 0°C into (100) 10-20 Ω -cm p-type wafers. The ion energy was 100 keV and the dose $7.3 \times 10^{15} \text{ cm}^{-2}$.

Laser annealing was performed using our scanning cw laser system (5) with a 250 mm focal length lens and a scanning speed of 7 cm/s. The overlapping between adjacent lines was very substantial, about 80%, to assure a homogeneous annealing. Unless otherwise specified, the annealing power was 86% of the power required to melt the Si surface. This results in a calculated (6) annealing temperature of 1200°C.

Thermal annealing was carried out in flowing nitrogen. The furnace boat was of light construction and supported the sample at edges only so as to assure a quick heating and cooling of the sample when pushed in and pulled from the furnace.

2. Electrical Measurements: C_{ss}

We used Van der Pauw measurements combined with anodic sectioning to obtain the electron concentration and mobility vs. depth. The results from these measurements are given in Fig. 1. Also plotted in this figure is the calculated LSS profile for the as-implanted As as well as the Irvin mobility which is expected if the as-implanted profile is electrically active.

Laser annealing only produces practically complete activation of the implanted As: the dose integrated from the points given in Fig. 2 is $6.94 \times 10^{15} \text{ cm}^{-2}$. The fit with the LSS-profile is excellent. Also, the measured mobility agrees very well with the Irvin mobility.

We studied the effect of laser annealing power on the activation and found that the activation was complete even at a power which was 75% of the melting power, corresponding to an annealing temperature of 1050°C. Below this, unannealed areas were visible on the sample. This indicates that solid phase epitaxy, which is the mechanism of cw annealing (7), brings all the dopants to substitutional sites independently of the annealing temperature, providing that the annealing time and temperature are sufficient to regrow the entire implanted layer.

Thermal annealing at 900°C of the laser annealed sample causes a dramatic drop in the electron concentration (Fig. 1). After thermal annealing the maximum concentration is $2.7 \times 10^{20} \text{ cm}^{-3}$. No appreciable diffusion has taken place during thermal annealing, indicating that the decrease in the maximum electron concentration is really due to

deactivation of dopants rather than just broadening of the profile. It is also interesting to notice that while the concentration decreases, the mobility (also shown in Fig. 1) increases to a value which corresponds exactly to Irvin mobility at that lower concentration. This shows that the inactive As does not act as scattering centers.

When the laser annealed sample was thermally annealed at 1000°C for 6 min, the equilibrium electron concentration was slightly higher, namely $3.0 \times 10^{20} \text{ cm}^{-3}$. Some diffusion is also observed here. We noticed, however, that the maximum concentration stays constant while diffusion takes place. This means that the nonactive As is activated again when diffusion tends to lower the maximum concentration. This also suggests that the amount of nonactive As in the lattice does not affect the maximum active concentration at a given temperature.

Furthermore, we have seen that at 1000°C the concentration decreases to $3 \times 10^{20} \text{ cm}^{-3}$ independently of how much the metastable concentration exceeded that value. And, if the laser annealed concentration was even slightly below $3 \times 10^{20} \text{ cm}^{-3}$, no deactivation was observed at 1000°C. That is why the solubility determined in this fashion is a true solubility according to the earlier definition.

We have also laser annealed a second time a sample which was previously laser and thermally annealed. The concentration, as shown in Fig. 1, increased to $6 \times 10^{20} \text{ cm}^{-3}$, and the mobility decreased correspondingly. The calculated (6) laser annealing temperature was 1200°C, suggesting that the solubility at 1200°C might be at least $6 \times 10^{20} \text{ cm}^{-3}$.

The summary of solubility measurements is shown in Fig. 2. We can see that above 1000°C there is no increase in the measured equilibrium concentration. The reason is that at those temperatures the deactivation rate is so high that significant deactivation takes place during the cooling down after the sample is pulled from the furnace. That is why the point at 1100°C does not represent solid solubility; it demonstrates, however, that $3 \times 10^{20} \text{ cm}^{-3}$ is the maximum active concentration obtainable by diffusion, even at temperatures above 1000°C.

The point given at 1000°C might also be slightly too low for the above-mentioned reason. At 900°C and below the deactivation is slow enough to prevent any appreciable deactivation during the cooling down, which was observed to take place in a couple of seconds (the observation was based on the glowing of the sample).

The solubility value at 1200°C was taken from the laser + thermal + laser annealing experiment. It is subject to considerable uncertainty; however, it seems to fit the other data fairly well.

For comparison, the solubility data given by Trumbore (1) is also given in Fig. 2. We have included both the original measurement points and the interpolated and extrapolated curve found in the original paper

(1) and most manuals and textbooks.

We can see that extrapolation of our data above 1200°C leads to values which are not very far from Trumbore's measurement points. Those points might thus be quite good. However, Trumbore's extrapolation to lower temperatures has resulted in solubility values which are substantially higher than the maximum equilibrium electron concentrations.

3. Channeling Measurements, TEM

Figure 3 gives the results from 2.2 MeV $^4\text{He}^+$ channeling measurements performed on laser and laser + thermally annealed samples. Table I summarizes the values for minimum yield and nonsubstitutional As fractions. The measured values for electrically inactive fractions of As are also given in Table I. The TEM micrographs are given in Fig. 4.

After laser annealing, practically all the As is on substitutional sites, but there is substantial damage left: channeling minimum yield is as high as 13.8%, and TEM shows a fair number of dislocation loops. The channeling shows that there is a damage peak at the surface. TEM showed the same fact: removal of a thin (200 Å) Si layer by anodization decreased clearly the damage density.

Channeling of the sample after 900°C thermal annealing shows that, while a major portion (71%) of the As becomes electrically inactive during the thermal treatment, little increase takes place in the nonsubstitutional As fraction. This is in excellent agreement with the observations of W. K. Chu and B. J. Masters [8]. They show that thermal annealing of a metastable As concentration causes some As complexes to form, where the As atoms are displaced from lattice sites only slightly. Thus they are not easily detectable with channeling measurements without angular scan.

Both channeling and TEM show that annealing at 900°C causes an increase in the amount of crystal damage. According to the channeling spectrum, there are two damage maxima: one at the surface and near the depth of the peak As-concentration.

After thermal annealing at 500°C for 5 min. the amounts of inactive and off-axis As are a lot closer to each other, suggesting that gross precipitation has taken place. And indeed, TEM micrographs show formation of rod-shaped structures at 400°-500°C; those rods might serve as precipitation sites. (Fig. 4 shows a micrograph taken after 400°C annealing, because it is more clear. The structures after 500°C annealing are similar, but their density is much higher.)

4. Thermal Activation Energy of the Complex Formation

We have also measured the activation energy of the As deactivation process between 350°C and 410°C. Fig. 5 gives the time, which was required to decrease the metastable As concentration by 6%, as a function of temperature. The activation energy was found to be 2.0 eV. Since this is exactly the energy required to form one vacancy in Si, it

is likely that vacancies are part of the complexes formed during the deactivation.

Conclusions

We conclude that

- CW laser annealing can activate As in excess of solubility, because solid phase epitaxy causes the dopants to go on substitutional sites independently of temperature. (Of course, the temperature has to be high enough to regrow the entire implanted layer.)
- Concentrations above $3 \times 10^{20} \text{ cm}^{-3}$ are metastable. The dwell time of the laser spot is so short that no deactivation takes place during it. However, subsequent thermal annealing causes the concentration to relax to a value which depends on the annealing temperature only, providing a method of measuring solubility limits (C_{ss} according to the definition given in the introduction).
- The solubility of As in Si is $9 \times 10^{19} \text{ cm}^{-3}$ at 700°C and $3 \times 10^{20} \text{ cm}^{-3}$ at 1000°C , the latter value being in good agreement with thermal diffusion experiments.
- MeV ion channeling measurements suggest that the deactivation mechanism at high temperatures is formation of complexes where the As atoms are offset only slightly from their substitutional positions. At lower temperatures ($400\text{--}500^\circ\text{C}$) gross precipitation seems to take place.
- The activation energy of the process is well-defined at least around 400°C , and was found to be 2.0 eV. This suggests that vacancies are part of the complexes formed during the deactivation.

Acknowledgments

Stanford work was supported by DARPA (R. Reynolds) contracts MDA 903-78-C-0128 and MDA 903-78-C-0290. One of us (A. Lietoila) wishes to acknowledge Teledyne MEC for supporting this work.

REFERENCES

- (1) F. A. Trumbore, Bell Syst. Techn. J. 39, 205 (1960).
- (2) See, e.g., R. S. Fair and J. C. C. Tsai, J. Electrochem. Soc. 122, 1689 (1975).
- (3) J. L. Regolini, T. W. Sigmon and J. F. Gibbons, Appl. Phys. Lett. 35, 114 (1979).
- (4) A. Lietoila, J. F. Gibbons, T. J. Magee, J. Peng and J. D. Hong, Appl. Phys. Lett. 35, 532 (1979).
- (5) A. Gat and J. F. Gibbons, Appl. Phys. Lett. 32, 142 (1978).
- (6) Y. Nissim, A. Lietoila, R. B. Gold and J. F. Gibbons, to be published in J. Appl. Phys.
- (7) A. Gat, A. Lietoila and J. F. Gibbons, J. Appl. Phys. 50, 2926 (1979)
- (8) W. K. Chu and B. J. Masters, Laser-Solid Interactions and Laser Processing - 1978 (edited by S. D. Ferris, H. J. Leamy and J. M. Poate), AIP Conference Proceedings No. 50, p. 305.
- (9) W. K. Chu, J. W. Mayer, M. A. Nicolet, Backscattering Spectrometry, Academic Press, New York 1978, p. 269.

Table I. Minimum yield, X_{\min} , and the percentage of non-substitutional and electrically inactive As in the samples which were laser annealed and then subjected to various thermal treatments. The implantation was 7.3×10^{15} As/cm² at 100 keV.

Annealing	X_{\min}	Off-axis As*	Electrically inactive As
Laser only	13.8%	7.8%	5.5%
Laser + 16' 900°C	20.2%	18.9%	71.0%
Laser + 5' 500°C	23.5%	30.3%	50.0%

* Since X_{\min} for Si is relatively high, the off-axis As values have been corrected according to Ref. 9.

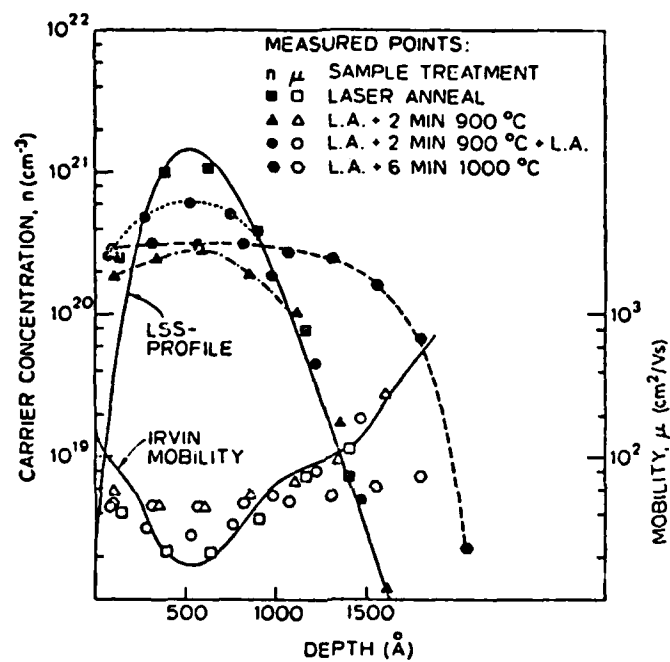


Fig. 1 Results from differential Van der Pauw measurements for samples which were laser annealed and then subjected to various thermal treatments. Also shown are the calculated LSS-profile for the $7.3 \times 10^{15} \text{ cm}^{-2}$, 100 keV $^{75}\text{As}^+$ -implantation and the Irvin mobility which is expected if the as-implanted profile is electrically active (solid lines).

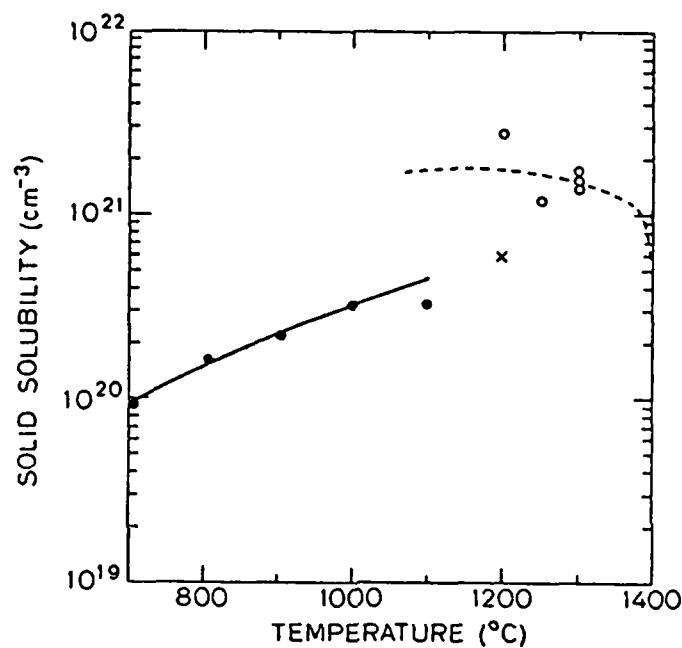


Fig. 2 The solubility of As in Si as an active, substitutional, non-complexed dopant. The closed circles are from the laser + thermally annealing experiments, and the cross was obtained by laser annealing a second time a laser + thermally annealed sample. The open circles and the dotted line are the data given in Ref. 1.

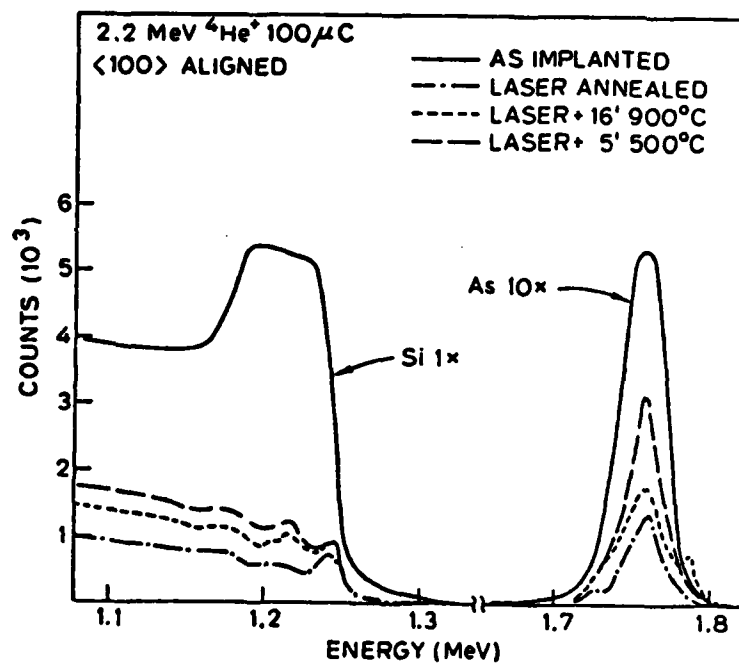


Fig. 3 2.2 MeV $^4\text{He}^+$ channeling spectra from the laser and thermally annealed samples. The implantation dose ($7.3 \times 10^{15} \text{ cm}^{-2}$) was calculated from the non-annealed spectrum.

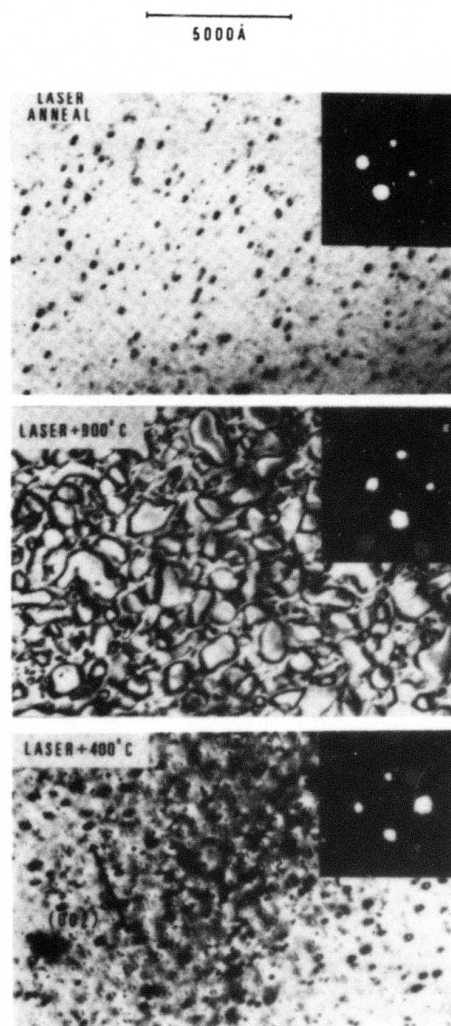


Fig. 4 TEM micrographs and selected area diffraction patterns of samples similar to those analyzed with channeling.

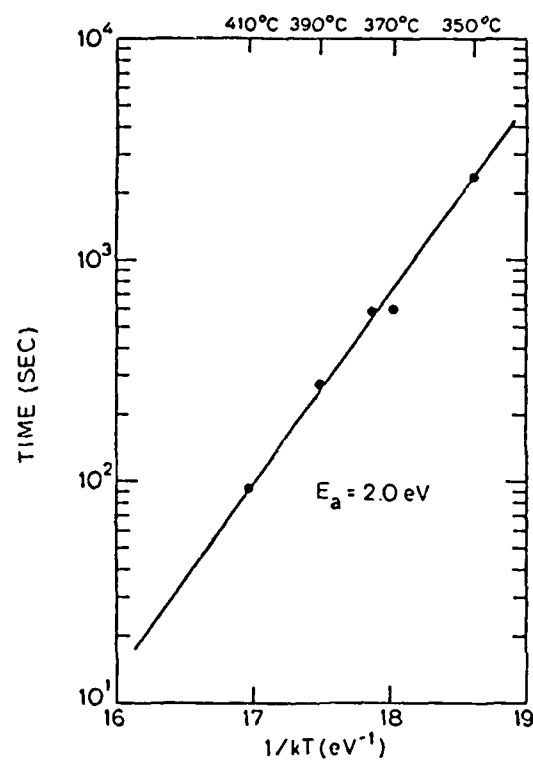


Fig. 5 The time required to decrease the metastable concentration by 6%. The plot shows a well-defined activation energy, 2.0 eV, for the deactivation process.

Metastable ^{75}As concentrations formed by scanned cw e-beam annealing of ^{75}As -implanted silicon

J. L. Regolini,^{a)} T. W. Sigmon, and J. F. Gibbons
Stanford Electronics Laboratories, Stanford, California 94305

(Received 9 April 1979; accepted for publication 15 May 1979)

The incorporation of ^{75}As into substitutional lattice sites in silicon in excess of 10^{21} cm^{-3} is reported. This has been accomplished by both a scanned cw e-beam and a scanned cw laser operating with dwell times in the range of milliseconds. Both electron concentration (using differential van der Pauw) and atom location measurements (using MeV ion channeling) are reported. Standard thermal processing indicates that these layers are metastable.

PACS numbers: 61.70.Tm, 71.55.Fr, 72.80.Ey, 81.40.Ef

The formation of metastable layers by the use of Q -switched lasers has been reported recently.¹ Of particular interest is the possibility of incorporating impurities into the silicon lattice at levels above their published solubilities. Further annealing of these layers by conventional means reduces the incorporated impurity to thermal equilibrium values, hence the term "metastable". It is generally accepted that the time constants involved in the Q -switched annealing case are short enough ($\sim 100 \text{ nsec}$) so that a nonthermal equilibrium situation exists, and the solubility of the impurity in the molten layer exists in the solid after cooling.²

The purpose of this work was to explore more fully the time constants of the kinetics governing the formation of metastable layers in silicon. To this end we have used implanted arsenic layers in silicon as they allow both ion channeling and electrical measurements to be easily performed, and a scanned cw e-beam and laser to obtain time constants on the order of milliseconds.

Implantation of 10^{16} As/cm^2 at 100 keV into $\langle 100 \rangle$ 10–20- Ω cm p -type Si held near -100 or 0°C was used to create thin ($\sim 1000 \text{ \AA}$) amorphous layers. Both a scanned cw argon laser³ and a scanned e-beam⁴ were used to anneal these layers. The important parameters were, for the cw laser, a substrate temperature of 350°C and a laser beam energy of 6.4 W, resulting in a corrected (reflection coefficient) power/radius value of $P/r = 0.17 \text{ W}/\mu\text{m}$. For the e-beam anneal, the substrate temperature was $\sim 50^\circ\text{C}$ and the beam energy was 14.0 W (31 kV at 0.45 mA), resulting in a $P/r = 0.14 \text{ W}/\mu\text{m}$. For both annealing techniques, electrical and/or mechanical scanning were used to provide uniform coverage of large areas. A differential van der Pauw technique⁵ was used to examine both electrical activity and mobility, while MeV ^4He -ion channeling measurements⁶ were used to analyze the lattice location of the implanted ^{75}As and residual damage effects within the annealed crystal.

We have used MeV ^4He -ion backscattering and channeling effect measurements to investigate both the impurity lattice site location and crystal quality of the annealed amorphous layers. In Fig. 1 we show data taken using a 2.2-MeV ^4He analyzing beam on: (a) as-implanted 10^{16} As/cm^2 and 10^{16} and 10^{15} As/cm^2 implanted and e-beam-annealed layers, respectively, (b) both laser and thermal annealed sam-

ples implanted to 10^{16} As/cm^2 . It can be seen that these aligned yields, which vary from 5 to 11%, for the various implant and anneal cases are above that expected for a virgin Si crystal (approximately 4%). The exact values are listed in Table I, with the values for 10^{15} As/cm^2 in parentheses. However, the following trend is clear: a high ^{75}As dose results in the highest minimum yield (χ_{\min}); the annealing order for a given dose is beam anneal then thermal for descending χ_{\min} . The thermal anneals were performed to ascertain whether or not the high residual disorder (residual disorder $\propto \chi_{\min}$) observed for the 10^{16} As/cm^2 implants were an artifact of the e-beam or laser anneals. The surface peak observed in all of these aligned spectra is on the order of a few hundred angstroms thick and has been reported to be caused by "knock-on" oxygen and carbon caused by the high-dose implant preventing recrystallization of this thin amorphous region.⁷

Comparison of the aligned ^{75}As yield obtained after annealing with that obtained for the unannealed amorphous layer results in information related to the percentage of ^{75}As atoms placed on substitutional lattice sites for a given anneal process. After correction for variation in the minimum yield for the various processes it can be seen that all three proce-

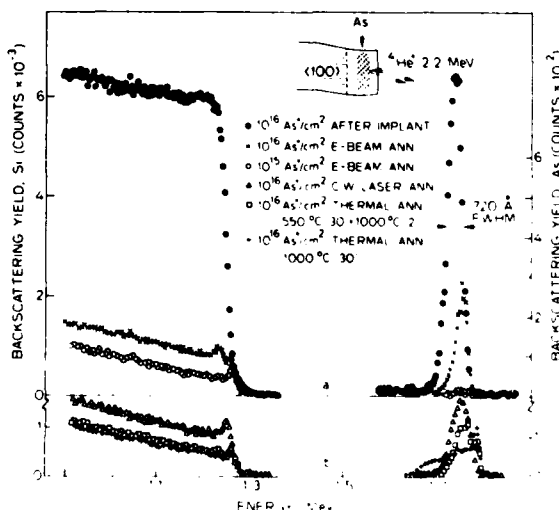


FIG. 1. 2.2-MeV ^4He backscattering and channeling results for (a) e-beam annealed As implanted Si and (b) laser- and thermal-annealed As-implanted Si.

^{a)}CONICET fellow on leave from CNEA, Argentina.

TABLE I. Experimental parameters and measured results for e-beam-, laser- and thermally annealed Si samples.

Implants 10^{16} As/cm ² , 100 keV (1.2×10^{15})	Thermal annealing			
	cw laser annealing	cw e-beam annealing	550 °C, 30 min + 1000 °C, 2 min	+ 1000 °C, 30 min
P/r (W/ μ)	0.17	0.14
Substrate Temp. (°C)	350	~ 50
Scanning speed (cm/sec)	12.5	2.5
Annealing ambient	Atmospheric	~ 10^{-4} Torr	N ₂	N ₂
χ_{\min} (Si) (%)	11.0	11.0 (3.9)	5.9	5.2
⁷⁵ As off axis (<100> channeling) (%)	22	21 (13)	19	24
⁷⁵ As inactive	20	28	63	...
(Difference between backscattering and (%) Van der Pauw measurements)				
Maximum carrier concentration (cm ⁻³)	1.13×10^{21}	1.07×10^{21}	4.1×10^{20}	...

dures result in approximately 75–80% substitutionality. These results are supported by the electrical measurements for all but the 575 °C thermal annealed case. Here, the number of atoms off axis and the electrically inactive differ by a factor of about 2. This effect is believed due to As pairing⁸ and will be discussed further later in this paper.

As expected for both the cw e-beam- and laser-annealed layers the measured impurity concentration (as inferred from the electron concentration) closely matches the calculated one (see Fig. 2). The more interesting aspect of this data is that the maximum electron concentration exceeds 10^{21} cm⁻³ for both the e-beam- and laser-annealed cases. This concentration is significantly higher than that measured on thermally annealed samples; for example, on an identically prepared sample annealed at 550 °C for 30 min followed by a 2-min anneal at 1000 °C (to minimize diffusion effects) a peak electron concentration of 4×10^{20} cm⁻³ was observed. Longer anneal times at 1000 °C result in only broadening of the ⁷⁵As profile with the peak electron concentration remaining at or below 4×10^{20} cm⁻³.

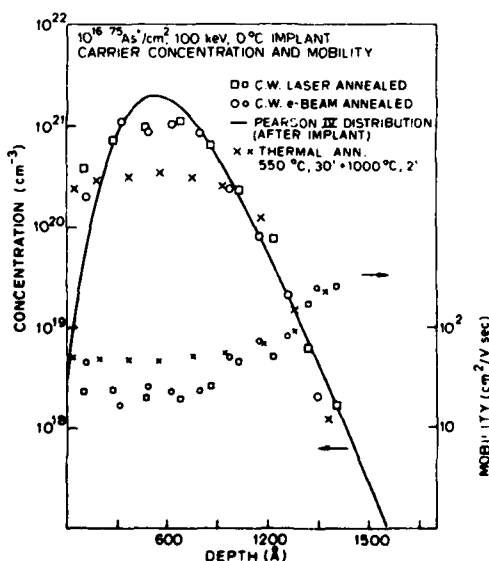


FIG. 2. Electron concentration and mobility versus depth for e-beam-, laser- and thermal-annealed samples.

Also shown in Fig. 2 is the measured electron mobility as a function of depth in the annealed layer. Excellent agreement is observed between this mobility and that calculated from Irwin⁹ using our measured electron concentration at all points (except those within 300 Å of the surface and at a depth of about 1200 Å). Since channeling effect measurements show a region of high damage near the surface and a small buried peak, one would expect to measure a mobility lower than theoretical, as is observed in Fig. 2 in these regions. It has been reported that thermally stable defects are generated in <100> ion-implanted Si near $R_p + \Delta R_p$ if the sample is not held below room temperature during the implant.¹⁰ This is a possible cause for the lower mobility observed near 1200 Å.

We have presented evidence that scanned cw e-beam and laser annealing can produce metastable electrically active layers with higher electron concentrations than can be obtained by standard thermal annealing. Both MeV ion channeling and differential resistivity and van der Pauw measurements have been used to measure the percent electrically active and on lattice sites after e-beam, laser, and thermal annealing. Electron concentrations in excess of 10^{21} cm⁻³ have been found for ⁷⁵As-implanted Si layers. Excellent agreement between the number of off-axis ⁷⁵As atoms and missing electrons has been obtained. Mobilities agree with calculated values within the annealed layer. Since arsenic is thought to form a $As^+ - V^- = As^+$ complex in silicon at high concentrations,⁸ we speculate that the time of formation of this complex is greater than the time constants of the e-beam laser-annealing process (order of milliseconds). This is supported by thermal annealing data for annealing times around 1 min.

We are pleased to acknowledge A. Lietoila for many fruitful discussions and to Dr. R. Reynolds, DARPA, for both his continued interest and support (Contracts DARPA MDA903-78-C-0290 and DARPA MDA903-78-C-0128).

J.M. Poate, H.J. Leamy, T.T. Sheng, and G.K. Celler, Appl. Phys. Lett. 33, 918 (1978).

C.W. White, W.H. Christie, B.R. Appleton, S.R. Wilson, P.P. Pronko, and C.W. Magee, Appl. Phys. Lett. 33, 662 (1978).

*A. Gat, J.F. Gibbons, T.J. Magee, J. Peng, V.R. Deline, P. Williams, and C.W. Evans, Jr., *Appl. Phys. Lett.* **32**, 276 (1978).
 *J.L. Regolini, J.F. Gibbons, T.W. Sigmon, and R.F.W. Pease, *Appl. Phys. Lett.* **34**, 410 (1979).
 *N.G.E. Johansson, J.W. Mayer, and O.J. Marsh, *Solid-State Electron.* **13**, 317 (1970).
 *W.K. Chu, J.W. Mayer, M-A. Nicolet, T.M. Buck, G. Amsel, and F. Eisen, *Thin Solid Films* **17**, 1 (1973).

*W.K. Chu, H. Müller, J.W. Mayer, and T.W. Sigmon, *Appl. Phys. Lett.* **25**, 297 (1974).
 *R.B. Fair and J.C.C. Tsai, *J. Electrochem. Soc.* **124**, 1107 (1977).
 *S.M. Sze, *Physics of Semiconductor Devices* (Wiley, New York, 1969), p. 43.
¹⁰L. Csepregi, E.F. Kennedy, S.S. Lau, J.W. Mayer, and T.W. Sigmon, *Appl. Phys. Lett.* **29**, 645 (1976).

Metastable As-concentrations in Si achieved by ion implantation and rapid thermal annealing

A. Lietoila, R. B. Gold, J. F. Gibbons, and T. W. Sigmon
Stanford Electronic Laboratories, Stanford, California 94305

P. D. Scovell and J. M. Young
Standard Telecommunication Laboratories Ltd., Harlow, Essex, England CM179NA

(Received 30 June 1980; accepted for publication 27 August 1980)

Rapid thermal annealing (4 min at 560 °C) of implanted As in Si can electrically activate concentrations up to $5 \times 10^{20} \text{ cm}^{-3}$, which exceeds the solubility at that temperature. Prolonged thermal annealing at the same temperature causes deactivation of such metastable concentrations. The results suggest that when the amorphous-crystalline interface is moving during solid phase epitaxial regrowth, dopants go to substitutional sites even in concentrations exceeding solubility. If solubility is exceeded, deactivation takes place after the material has recrystallized.

PACS numbers: 61.70.Tm

INTRODUCTION

It has recently been shown that cw laser or electron beam annealing of ion-implanted As in Si can lead to dopant concentrations in excess of solid solubility, thus creating a thermally unstable concentration.¹⁻³ A similar effect has been observed for thermally annealed implanted In in Si.⁴

In this paper we show that the equilibrium solubility can be exceeded also with thermal annealing of ion-implanted As in Si. The annealing time has to be so chosen that the amorphized layer can just regrow, but no time is available for subsequent deactivation of dopants.

EXPERIMENTAL

The samples were cut from 30 Ω -cm p-type $\langle 100 \rangle$ Si. The ⁷⁵As implantation was done at 150 keV to a dose of $6.2 \times 10^{15} \text{ cm}^{-2}$, keeping the samples at 0 °C in order to avoid self-annealing.

The short-time thermal anneals (up to 10 min) were performed by placing the samples onto a heatable brass vacuum chuck, which was held at a constant temperature, 560 °C. A simple calculation⁵ shows that once the sample is brought to contact with brass it reaches the chuck temperature in less than a second. Similarly, the sample cools down practically instantaneously after it has been removed from the chuck.

Thermal anneals for more than 10 min were done in a furnace in flowing nitrogen.

After annealing the samples for different times we studied the results by Van der Pauw⁶ and MeV-ion channeling measurements.⁷ The Van der Pauw measurements were performed in two ways. All samples were measured at the surface only, without depth profiling. This sheet measurement gives the true sheet resistivity R_s , an estimate \hat{N}_s of the sheet concentration, and a weighed average mobility $\bar{\mu}$ for the doped layer.⁶ For a few samples we also performed differential Van der Pauw measurements to obtain the electron concentration and mobility as a function of depth, as well as a more exact value for the active dose. The sectioning was done by anodic oxidation⁸ and stripping. The oxide thickness, which was measured by an ellipsometer, was about 450 Å at each step. The Si:SiO₂ thickness ratio has been measured to be 0.56 for our system at this thickness.⁹

The channeling measurements were done using 2.2 MeV ⁴He⁺ particles to a total charge of 40 μC .

RESULTS

The sheet Van der Pauw measurements (see Table I and Fig. 1 for results) show that the best activation is obtained with a 4 min annealing. Van der Pauw stripping (see Fig. 2)

TABLE I. Results from differential and sheet Van der Pauw measurements for samples annealed at 560 °C. The sheet concentration \hat{N}_s , sheet resistivity R_s , and average mobility $\bar{\mu}$, were obtained by measuring the entire implanted layer without stripping. The active dose is measured by the differential Van der Pauw method. The implanted dose was $6.2 \times 10^{15} \text{ As/cm}^2$ at 150 keV.

Anneal time	\hat{N}_s ($1/\text{cm}^2$)	R_s (Ω/\square)	$\bar{\mu}$ (cm^2/Vs)	Active dose ($1/\text{cm}^2$) ^a	Active As-fraction
3 min	4.4×10^{15}	32	44	...	79% ^b
4 min	4.5×10^{15}	31	46	5.0×10^{15}	81%
8 min	4.0×10^{15}	33	48	...	71% ^b
40 min	3.4×10^{15}	35	54	3.8×10^{15}	61%
15.5 h	2.2×10^{15}	40	70	...	39% ^b

^a Integrated from differential Van der Pauw measurements.

^b Calculated assuming that total active dose is 11% higher than \hat{N}_s , as it is in those cases where stripping was performed.

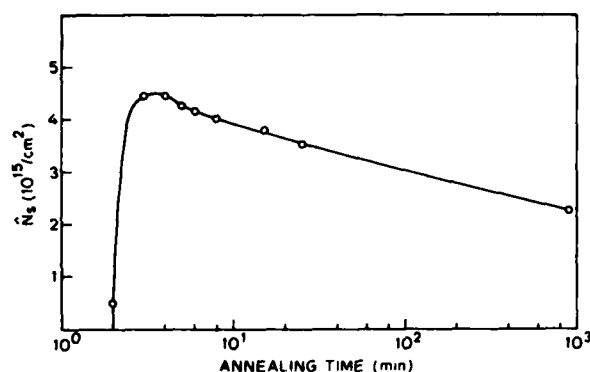


FIG. 1. Evolution of sheet carrier concentration \hat{N}_s of samples annealed at 560 °C.

reveals, however, that there is still 19% of inactive As; and the maximum active concentration is only $5 \times 10^{20} \text{ cm}^{-3}$, as opposed to the maximum of $9 \times 10^{20} \text{ cm}^{-3}$ in the as-implanted profile.

Channeling measurements (see Table II and Fig. 3) show that the sample is still partly amorphous after 2 min annealing, whereas 4 min is enough to completely regrow the amorphous layer. However, a relatively high density of damage is left at the sample surface. The observed regrowth rate is consistent with the data given by Csepregi *et al.*¹⁰: the thickness of the amorphous layer is 2050 Å (measured with channeling), which would regrow in about 15 min at 560 °C if the material were undoped. The doping reduces the total regrowth time of the entire layer by a factor of up to 4, depending on the dose.

The maximum concentration, $5 \times 10^{20} \text{ cm}^{-3}$, achieved with a 4 min annealing exceeds the solubilities given in Ref. 3 ($9 \times 10^{19} \text{ cm}^{-3}$ at 700 °C), so we would expect a prolonged annealing at 560 °C to cause deactivation of dopants. And indeed, Table I and Fig. 1 show that after 8 min the sheet concentration has already decreased about 10% from the maximum value. Continued annealing for up to 15.5 h produces a monotonic decrease in the sheet concentration, as is shown in Fig. 1 and Table I. After 15.5 h the sheet concentration was only $2.2 \times 10^{15} \text{ cm}^{-2}$, or 50% of the maximum value. We stopped annealing at this point, since there was still no sign of an approach to saturation.

To confirm that the decrease in sheet concentration really is due to deactivation of dopants, we stripped a sample annealed for 40 min at 560 °C. The results are given in Fig. 2, and show that the maximum active concentration has decreased to $3 \times 10^{20} \text{ cm}^{-3}$, while little diffusion has taken

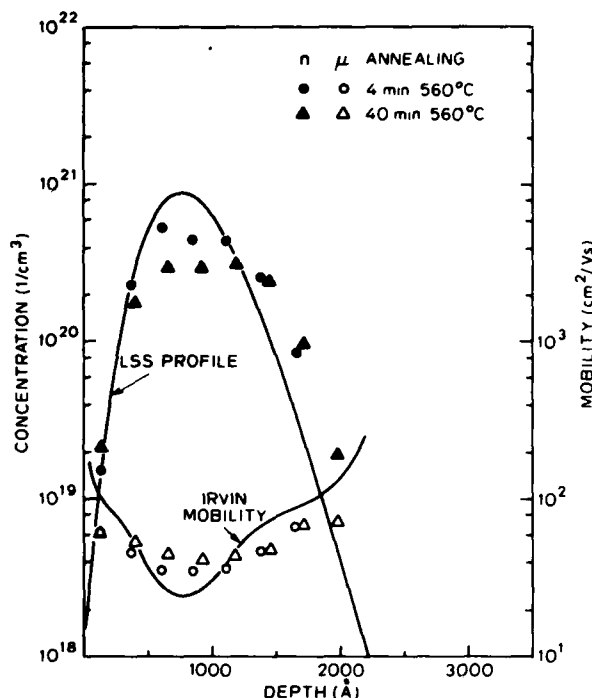


FIG. 2. Results from differential Van der Pauw measurements for samples annealed at 560 °C. The solid lines represent the calculated LSS-profile of the implantation ($6.2 \times 10^{15} \text{ As/cm}^2$, 150 keV) and the Irvin-mobility of that profile, assuming complete activation.

place. The amount of active As is $3.8 \times 10^{15} \text{ cm}^{-2}$ for this sample, which is 61% of the implanted dose.

Since the deactivation rate of As is initially so fast and decays with time, we believe that all As is at first activated during the regrowth. However by the time the entire layer has recrystallized, the dopants located deeper in the sample will have had ample time to start relaxing from the metastable state, resulting in incomplete activation even in the optimum case. Note that after the optimum annealing (4 min) the maximum electron concentration is closer to the surface than the peak of implanted distribution (see Fig. 2). This is consistent with the above hypothesis.

Finally, we performed channeling on a sample which was annealed for 40 min at 560 °C. We see in Fig. 3 and Table II that the amount of nonsubstitutional As has increased, compared to the case of 4 min annealing, along with electrical deactivation. In both cases the electrically inactive fraction is about a quarter larger than the non-substitutional fraction. This would suggest that part of the inactive As is incorporated in complexes, where the displacement of As-

TABLE II. Results from MeV-ion channeling measurements for samples annealed at 560 °C. The calculated fractions of nonsubstitutional As are subject to some error due to higher χ_{\min} values. For comparison, we also give the fractions of electrically inactive As.

Anneal time	Surface peak χ_0	minimum yield χ_{\min}	nonsubstitutional As	electrically inactive As
2 min		Still partially amorphous		
4 min	40%	10%	15%	19%
40 min	22%	8.7%	30%	39%

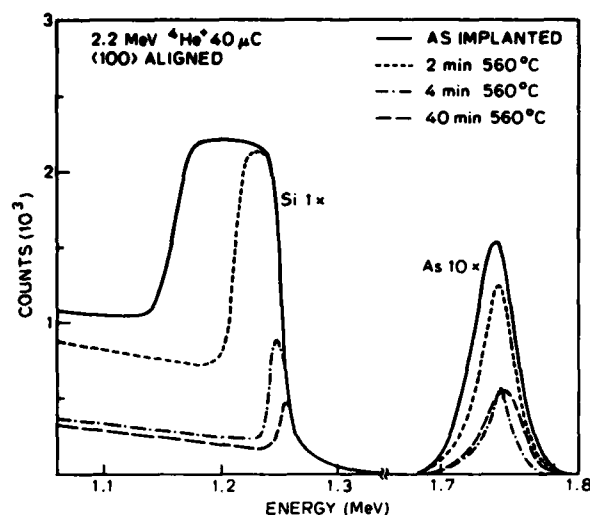


FIG. 3. Channeling spectra of as-implanted and annealed samples. The implantation dose ($6.2 \times 10^{15} \text{ cm}^{-2}$) and thickness of amorphous layer (2050 Å) were calculated from the as-implanted spectrum.

atoms off-lattice site is too small to be seen with regular channeling techniques.^{3,11}

CONCLUSIONS

The above results show that even thermal, often called "equilibrium", annealing of implanted As in Si can produce active concentrations well above the equilibrium solubility characteristic of the annealing temperature. To achieve this, the annealing time and temperature have to be so chosen that the amorphous layer can just regrow, but no time is available for deactivation. In practice, this requires annealing below 600 °C, which in turn results in substantial crystal damage being left at the sample surface. The concentrations exceeding solubility are of course thermally unstable.

The present results, and those given in Refs. 1–4, sug-

gest that when the amorphous-crystalline interface is moving in solid phase epitaxy, the impurity atoms go on substitutional sites even in concentrations exceeding the equilibrium solubility. The deactivation starts after the material has crystallized, if solubility was exceeded. This is analogous to the observed increase in solid-liquid segregation coefficient of impurities in liquid phase annealing by pulsed lasers.¹² In both cases, there is a moving crystal front, at which the dopants seem to prefer occupying substitutional sites even if the equilibrium concentration were exceeded.

ACKNOWLEDGMENTS

The Stanford authors are indebted to NSF, Grant DMR78-19970-A1, for financial support. The STL authors wish to acknowledge the support of the procurement executive, UK Ministry of Defense, sponsored by DCVD.

- ¹J. L. Regolini, T. W. Sigmon, and J. F. Gibbons, *Appl. Phys. Lett.* **35**, 114 (1979).
- ²A. Lietoila, J. F. Gibbons, T. J. Magee, J. Peng, and J. D. Hong, *Appl. Phys. Lett.* **35**, 532 (1979).
- ³A. Lietoila, J. F. Gibbons, and T. W. Sigmon, *Appl. Phys. Lett.* **36**, 765 (1980).
- ⁴P. Blood, W. L. Brown, and G. L. Miller, *J. Appl. Phys.* **50**, 173 (1979).
- ⁵J. Crank, *The Mathematics of Diffusion*, 2nd ed. (Clarendon, Oxford, 1975), p. 47.
- ⁶See, e.g., N. G. E. Johansson, J. W. Mayer, and O. J. Marsh, *Solid State Electron.* **13**, 317 (1970).
- ⁷W. K. Chu, J. W. Mayer, and M. A. Nicolet, *Backscattering Spectrometry* (Academic, New York, 1978).
- ⁸H. D. Barber, H. B. Lo, and J. E. Jones, *J. Electrochem. Soc.* **123**, 1404 (1976).
- ⁹J. L. Regolini (unpublished).
- ¹⁰L. Csepregi, E. F. Kennedy, T. J. Callaghan, J. W. Mayer, and T. W. Sigmon, *J. Appl. Phys.* **48**, 4234 (1977).
- ¹¹W. K. Chu, in *Laser and Electron Beam Processing of Electronic Materials*, *ECS Proc.* 80-1 (The Electrochemical Society, Princeton, 1980), p. 361.
- ¹²E. Rimini, in *Laser and Electron Beam Processing of Electronic Materials*, *ECS Proc.* 80-1 (The Electrochemical Society, Princeton, 1980), p. 270.

Use of a scanning cw Kr laser to obtain diffusion-free annealing of B-implanted silicon

A. Gat and J. F. Gibbons^{a)}

Stanford Electronics Laboratories, Stanford, California 94305

T. J. Magee and J. Peng

Advanced Research and Applications Corp., Sunnyvale, California 94086

P. Williams, V. Deline, and C.A. Evans, Jr.

School of Chemical Science, Materials Research Laboratory, University of Illinois, Urbana, Illinois 61801

(Received 21 March 1978; accepted for publication 9 May 1978)

The use of a continuous scanned Kr ion laser as a tool for annealing of boron-implanted silicon is described. Conditions were found that produce high electrical activity and crystallinity of the implanted layer without redistribution of the boron from the as-implanted profile.

PACS numbers: 79.20.Da, 81.40.Ef, 42.60.-v, 61.70.-r

Recent work at a number of laboratories¹⁻⁷ has shown that ion-implanted Si and GaAs can be annealed by exposing the implanted region to laser radiation of appropriate energy and wavelength. Annealing has been accomplished using both pulsed and cw lasers with generally similar results. In particular, high-quality epitaxial recrystallization of the implanted material on the underlying substrate has been reported for both pulsed and cw laser annealing. However, studies to date with pulsed lasers show that a substantial redistribution of the implanted dopant occurs during annealing, whereas in the cw laser annealing experiments reported by the present authors no diffusive redistribution of the implanted dopant was observed.

In view of the potential importance of diffusion-free annealing for the fabrication of fine geometry devices, we have undertaken a series of experiments to determine the conditions under which diffusion-free laser annealing can be obtained. We are particularly interested in the question of whether low-dose B implants into crystalline Si can be annealed without diffusion, especially in view of the results of Young *et al.*,³ who obtain B diffusion to greater depths with their laser-annealing conditions than they obtain under conventional thermal annealing conditions.

The central result of the experiment reported here is in sharp contrast to that obtained by Young *et al.* We observe no diffusion during annealing, using implantation conditions that are identical to those of Young *et al.*

B⁺ was implanted at room temperature at 35 keV to

a dose of 2×10^{15} ions/cm² into 5–10-Ω cm *n*-type (100) silicon samples. This dose is not sufficient to drive the silicon amorphous but damages the surface layer to a depth of ~0.25 μm. After the implantation, the wafer was cut into a set of 5×5-mm samples. Several samples were subjected to a 1000 °C 30-min thermal anneal in flowing N₂ to provide standards of comparison for the laser-annealed samples.

The laser-annealed samples were subjected to an annealing sequence similar to that described in Ref. 1. The main difference was the use of a krypton ion laser manufactured by Coherent Radiation (Model CR-3000K). This laser was operated in the multimode red region. Its main power is in the 6471-Å line with a weaker line (usually 25% of the strong line) at 6764 Å.

Several values of laser power and *x* scan rate were used in an attempt to find near-optimum annealing conditions. Satisfactory results were achieved with a total laser power of 6 W and an *x* scan rate of 9.8 cm/sec. The temperature of the sample, which proves to be critical for full anneal, was held at 178 °C in the experiments to be reported.

After annealing, the sheet resistivity of the samples was measured using a surface spreading resistance apparatus. Figure 1 shows the resistance recorded for three samples. Samples S1B155, which is typical of the thermally annealed samples, shows a probe-to-probe resistance of 73 Ω. Sample 7S37 was laser annealed over half of the sample and the probes were then stepped across the annealed boundary. On the unannealed side the probe-to-probe resistance was greater than 20 kΩ; in the annealed area the probe-to-probe resistance was about 95 Ω. The probes were also advanced across laser lines with the results shown in Fig. 1. The periodic character of the resistivity data shows that the overlap

^{a)}Work supported by the National Science Foundation DMR7618000 and the Advanced Research Projects Agency MDA903-78-C-0128.

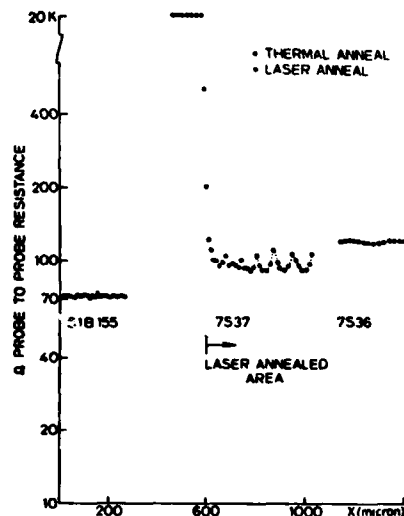


FIG. 1. Surface spreading resistance measurements done on implanted silicon samples subjected to laser and thermal anneal.

between two adjacent lines was not sufficient to complete the annealing process.

Sample 7S36 was laser annealed under the same conditions as 7S37. In this case the measurement was performed along the scanned lines. We observe good uniformity with distance in contrast with 7S37. To complete the study we measured four laser-annealed samples, all of which showed resistance in the range 100–150 Ω .

To estimate electrical activity for these samples requires a knowledge of the impurity profiles for both cases. These profiles were obtained by SIMS measurements and are reported below.

A variety of annealed and as-implanted samples were analyzed by a SIMS technique using O^- as the primary ion beam. The results of these measurements are shown in Fig. 2. Background noise has been subtracted and the separate profiles corrected in terms of the Si signal measured for each sample.

A comparison of results obtained from as-implanted, laser anneal, and thermal anneal is given in Fig. 2. The vertical axis is in counts per frame and is proportional to the impurity concentration in the solid. The horizontal axis is in sputtering time, which relates to depth of measured ion concentration.

The most striking result of this measurement is that the laser-annealed impurity distribution is essentially identical to the as-implanted distribution. By comparison, the thermally annealed sample shows substantial diffusive redistribution of the boron during the annealing cycle (as expected).

The impurity profiles given in Fig. 2 provide the key for explaining the difference in sheet resistance between the thermally annealed and laser-annealed samples. The equation for the sheet resistance of a layer is

$$R = \left[\int_0^{\infty} q \mu_p(x) p(x) dx \right]^{-1} = \left[\int_0^{\infty} d\mu_p(x) N_A(x) dx \right]^{-1}, \quad (1)$$

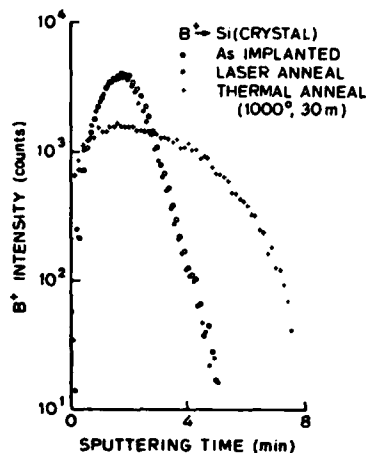


FIG. 2. Impurity profiles by SIMS technique in as-implanted, laser annealed and thermally annealed Si implanted with $2 \times 10^{15} B^+/cm^2$ at 35 keV.

where q is the electron charge, $p(x)$ is the concentration of holes, $\mu_p(x)$ is the hole mobility, and $N_A(x)$ is the acceptor concentration.

Equation (1) was numerically integrated with the values of Fig. 2 after proper transformation of the axis. The calculations predict a 50% increase in sheet resistance for the laser-annealed profile compared to the thermal profile, due to the higher peak concentration and lower carrier mobility in the laser-annealed samples. This same result was obtained experimentally in Fig. 1 and enables us to conclude that essentially all of the implanted boron is contributing to the electrical properties of the crystal. Stripping measurements confirm this result.

Transmission electron microscopy/diffraction was used to examine both laser scanned and thermally annealed samples. In all cases single-crystal (spot diffraction patterns were obtained after implantation (no postanneal), thermal annealing, or laser annealing.



FIG. 3. Transmission electron micrograph of B-implanted sample thermally annealed at 1000°C for 30 min.

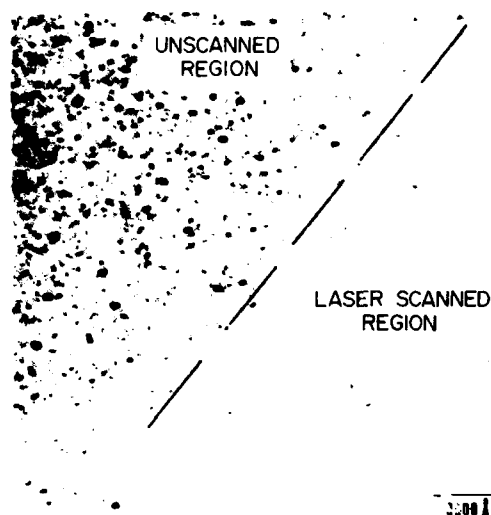


FIG. 4. Transmission electron micrograph of B-implanted laser-annealed sample at laser scan boundary.

In Fig. 3, we show a bright-field electron micrograph of an implanted sample annealed at 1000 °C in flowing N_2 for 30 min. In agreement with previous investigations^{10,11} on B-implanted silicon thermally annealed within this temperature range, residual defects in the form of dislocation loops, line defects, dipole remnants, and dislocation nests are observed throughout the implanted region.

For comparison, we show in Fig. 4 a micrograph obtained on a sample subjected to a single laser line scan. Negligible or near-zero defect concentration is observed throughout the laser-annealed regions of both single (nonoverlapping) line scans (Fig. 2) and overlapping line scans. This is the case whether observations are made at the center of the the annealed line or in overlapping regions between two adjacent lines (not shown in Fig. 4). In all samples examined, we detected no evidence of melting/recrystallization or implanted impurity segregation. Furthermore, our experiments indicate a complete absence of rod-shaped structures or dislocation dipoles previously reported¹²⁻¹⁴ for conventional thermal anneals at temperatures ≥ 700 °C. The absence of rod-shaped structures and dislocation lines at the boundary of a laser line in the presence of a thermal gradient and lower effective temperatures (within the unscanned region) suggests that rod defects are not nucleated in these experiments even under sub-threshold (lower power) laser-anneal conditions.

At the edge of the laser scan within the unscanned region (left portion, Fig. 4), the concentration of dislocation loops is observed to increase as a function of increasing distance from the laser scan boundary. In addition, the average loop (image) diameter determined from a number of micrographs decreases from ≈ 380 Å within the zone adjacent to the laser scan line to ≈ 250

Å at distances ≥ 8000 Å from the laser scan boundary. This lateral variation in defect density can be related to thermal gradients and differential annealing created at the edge of the scan line by the Gaussian beam profile while the increase in apparent loop diameter at the edge zone can either be attributed to strain relaxation at the peripheral boundary zone or interpreted as possible evidence of growth of a smaller number of sites that serve as sinks for defects during laser annealing.

In work previously reported by the present authors it was shown that Si samples implanted with 5×10^{14} As/cm² at an energy of 100 keV could be laser annealed to provide high electrical activity and essentially perfect recrystallization with no significant diffusion of the implanted species during annealing. These implantation conditions produce an amorphous layer that contains essentially all of the implanted atoms.

The present results extend this basic annealing behavior to nonamorphizing implants into Si. Hence, for Si at least, laser annealing can provide a technique for essentially perfect annealing of implanted material, where by "perfect" we imply complete recrystallization and 100% electrical activity without diffusive redistribution of the implanted species.

The authors would like to acknowledge the assistance of Mark Hanesian for help in using the Krypton laser; Carrol Frankfurt for the construction of the temperature-controlled sampler holder; Arto Leitoila for helpful discussion and samples preparation; and Dr. D. Lee (Hughes Research Laboratories) for performing the implantations.

¹A. Gat and J. F. Gibbons, *Appl. Phys. Lett.* 32, 142 (1978).

²A. Gat, J. F. Gibbons, T. J. Magee, J. Peng, V. R. Deline, P. Williams, and C. A. Evans, Jr., *Appl. Phys. Lett.* 33, 276 (1978).

³R. T. Young, C. W. White, G. J. Clark, J. Narayan, and W. H. Christie, *Appl. Phys. Lett.* 32, 139 (1978).

⁴G. A. Kachurin and E. V. Nidaev, *Sov. Phys.-Semicond.* 11, 350 (1977).

⁵A. Kh. Antonenko, N. N. Gerasimenko, A. V. Dvuvchenskii, L. S. Smirnov, and G. M. Teseiltin, *Sov. Phys.-Semicond.* 10, 81 (1976).

⁶G. Foti, E. Rimini, G. Vitali, and M. Bertolotti, *Appl. Phys. Lett.* (to be published).

⁷J. A. Golo'chenko and T. N. C. Venkatesan, *Appl. Phys. Lett.* 32, 147 (1978).

⁸J. J. Comer and S. A. Roosild, *Radiat. Eff.* 25, 275 (1975).

⁹G. P. Pelous, D. P. Lecrosnier, and P. Henoc, in *Ion Implantation in Semiconductors*, edited by S. Namba (Plenum, New York, 1975, p. 439).

¹⁰R. W. Bickness and R. M. Allen, *Radiat. Eff.* 6, 45 (1970).

¹¹S. M. Davidson and G. R. Booker, *Radiat. Eff.* 6, 33 (1970).

¹²L. T. Chadderton and F. H. Eisen, *Radiat. Eff.* 7, 129 (1971).

Constant-capacitance DLTS measurement of defect-density profiles in semiconductors^{a)}

N. M. Johnson and D. J. Bartelink

Xerox Palo Alto Research Center, Palo Alto, California 94304

R. B. Gold and J. F. Gibbons

Stanford University, Stanford, California 94305

(Received 26 December 1978; accepted for publication 16 February 1979)

An analysis is presented for obtaining spatial depth profiles of electronic defects in semiconductors from deep-level spectroscopic measurements performed in the constant-capacitance mode. Combined with the double-correlation technique proposed by Lefevre and Schulz, the new method offers significant advantages for measuring defect profiles. Deep-level transient spectroscopy (DLTS), performed in either the conventional capacitance-transient mode or the constant-capacitance mode, provides the energy levels of defect states in the semiconductor band gap. The double correlation DLTS technique (DDLTS) is used to define a narrow spatial observation window for defect profiling. However, in the DDLTS analysis of *capacitance-transient* data, specific approximations are required to deal with the change with time of the semiconductor depletion width during the transient response to a charging pulse. In the *constant-capacitance* mode, the depletion width is held constant by dynamically varying the applied voltage during the transient response, thus permitting more accurate measurements of defect profiles at high trap densities. Analytical expressions for computing the local trap density are derived, and experimental results are presented for damage profiles in self-implanted silicon.

PACS numbers: 72.20.Jv, 71.55.Fr

I. INTRODUCTION

This paper describes an improved transient-capacitance technique for measuring the spatial distribution of electronic defects in semiconducting materials. Transient-capacitance spectroscopy is widely used to measure (1) defect energy levels in a semiconductor forbidden energy band, (2) effective cross sections of point defects for capturing charge carriers, and (3) defect densities.¹ The spectroscopic principle is based on two electronic phenomena. The first is the ability to vary the capacitance of a semiconductor test structure with an applied dc bias. For example, in a metal-semiconductor rectifying contact, the application of a reverse bias creates a surface layer in the semiconductor which is depleted of majority carriers. The width of the depletion layer increases monotonically with reverse bias, up to the point of electrical breakdown. The depletion layer acts as the dielectric of a parallel-plate capacitor, giving rise to a voltage-dependent capacitance. The other basic phenomenon is the capture and emission of charge carriers by defect centers. In a semiconductor depletion layer, electronic transitions between localized defect levels and the extended states of the allowed energy bands alter the space-charge density. This in turn affects the depletion width so that such transitions can be detected as a change in device capacitance. In a transient-

capacitance measurement, trapping centers in a selected region of the depletion layer are first populated with charge carriers. Then the capacitance is monitored as the trapped charge is thermally emitted and swept out of the depletion layer. The emission process is thermally activated so that the rate at which the capacitance relaxes strongly depends on temperature. Several experimental techniques have been developed for efficiently monitoring this transient response with high sensitivity. The basic method used in this paper was developed by Lang² and is termed deep-level transient spectroscopy (DLTS). It combines a capacitance bridge of high sensitivity and fast transient response with signal-detection instrumentation for monitoring the capacitance decay in a temperature scan. An essential feature of this method is the implementation of an emission-rate window for monitoring a given relaxation time as the temperature is varied. The measurement yields trap emission spectra from which defect energy levels, capture cross sections, and defect densities are computed. A modification of the DLTS technique was proposed by Lefevre and Schulz¹ for measuring spatial depth profiles of defect levels. The technique is termed double-correlation DLTS (DDLTS) and is used to define a narrow spatial interval in a semiconductor depletion layer for detecting trap emission. This observation window can be translated in depth to obtain defect distributions. Both DLTS and DDLTS are conventionally performed as *capacitance-transient* measurements.

In this paper we present the analysis and results from

^{a)}Work supported by the Defense Advanced Research Projects Agency (Order No. 2397) through the National Bureau of Standards Semiconductor Technology Program.

DLTS measurements of bulk semiconductor defects which are performed in the *constant-capacitance* mode. The technique is termed constant-capacitance DLTS (CC-DLTS) and has proved to be essential for the DLTS analysis of interface defect levels in metal-insulator-semiconductor (MIS) structures.⁴ When combined with the double-correlation technique, the new method offers significant advantages for measuring defect profiles. In the DDLTS analysis of capacitance-transient data, specific approximations are required to deal with the change with time of the semiconductor depletion width during the capacitance decay.³ These approximations become inapplicable at high trap concentrations. In the constant-capacitance mode, the depletion width is held constant by dynamically varying the applied voltage during the transient response, thus permitting more accurate DLTS measurements of defect profiles at high trap densities. Measurements of semiconductor defect levels under conditions of constant capacitance have been reported by others.⁵⁻⁷ In the present study the constant-capacitance technique is combined with DLTS and DDLTS so as to fully retain the inherent advantages of these later techniques while gaining the additional feature provided by the constant-capacitance mode of measurement. The double-correlation CC-DLTS technique is described in Sec. II, and the analysis for obtaining defect-density profiles is presented in Sec. III. In Sec. IV the new method is illustrated with measurements of damage profiles in self-implanted silicon.

II. EXPERIMENTAL TECHNIQUE

One of several simple two-terminal devices can be used for transient-capacitance measurements on semiconducting materials. The principal requirement is the ability to vary the device capacitance with a dc bias. Current-rectifying devices based upon either the Schottky-barrier structure (metal-semiconductor contact) or the *p-n* junction are commonly employed, and the MIS structure can also be used. The Schottky diode is the simplest device to fabricate, requiring only the deposition of a metallic rectifying contact onto the semiconductor; this permits the maximum flexibility for semiconductor materials evaluation. A limitation of the Schottky-barrier structure for DLTS studies arises from its being a majority-carrier device: only defect levels in the majority-carrier half of the semiconductor band gap can be detected. With a *p-n* junction, minority-carrier trapping can also be examined.² In MIS structures the DLTS technique has been used to measure trapping centers at the semiconductor-insulator interface.^{4,8-10} With all of the above test devices there is an essential requirement for unambiguous DLTS analysis: the electrical contact to the back of the specimen must be Ohmic over the entire range of measurement temperatures, typically from 77 K to above room temperature. This requirement can be satisfied through the use of epitaxially grown semiconductors with degenerately doped substrates or by ion implanting the backside of a bulk semiconductor to create a degenerately doped surface layer. Alloyed back contacts can also be used for this purpose. For brevity of presentation the remainder of this paper will focus on the Schottky-barrier test device.

The measurement system used in the present study has

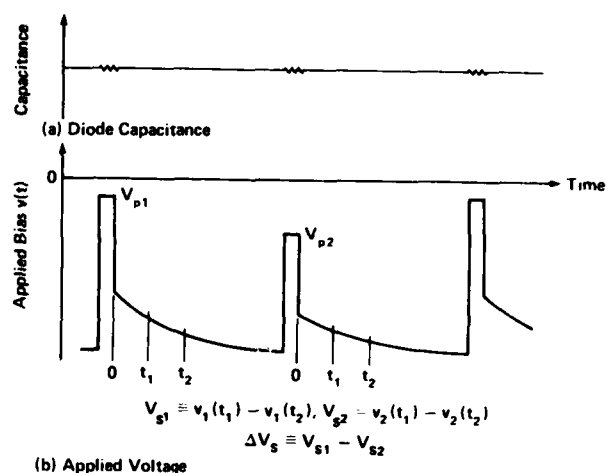


FIG. 1. Schematic diagrams of the transient response for a semiconductor diode in a constant-capacitance DLTS measurement. (a) The device capacitance is held constant after each charging pulse, and (b) the applied bias is a superposition of the charging pulses and a time-varying reverse bias. The pulses are applied in pairs with adjacent pulses set at different amplitudes in order to define a spatial observation window (see Fig. 2). The net emission signal ΔV_s is the difference of DLTS signals V_{s1} and V_{s2} , which are measured after pulses V_{p1} and V_{p2} , respectively.

been described elsewhere.^{4,10} It is based upon the system originally proposed by Lang¹¹ and consists of a capacitance bridge with fast transient response, a pulse generator for rapidly changing sample bias, a dual-gated signal integrator for monitoring the transient response, and a variable-temperature cryostat. The double-correlation DLTS technique is implemented by using a dual-pulse generator to apply pairs of voltage pulses with the adjacent pulses set at different amplitudes, and separate signal integrators are used to record the DLTS signal for each pulse in the pair.³ For the constant-capacitance mode of measurement, the system includes feedback circuitry which maintains the capacitance of a device at a constant value by dynamically varying the applied voltage.^{4,10}

Schematic diagrams of the capacitance and voltage waveforms for the double-correlation CC-DLTS measurement are shown in Fig. 1. For a Schottky barrier on an *n*-type semiconductor, DLTS is used to measure electron emission from defect levels. A reverse bias is used to establish a depletion layer, and a voltage pulse is periodically applied to reduce the depletion width. Traps located below the quasi-Fermi energy are filled with electrons during a charging pulse. After the charging pulse the trapped electrons are thermally emitted to the conduction band and swept out of the depletion layer. Between charging pulses the measurement system maintains the device capacitance at a constant value, as shown in Fig. 1(a). This is achieved for a time variation in the applied voltage, as shown in Fig. 1(b) for dual-pulse biasing conditions. The voltages during pulse biasing are designated V_{p1} and V_{p2} . For each pulse in the pair, the DLTS signal is obtained by forming the difference of the applied biases measured at the two delay times t_1 and t_2 after

the pulse. The DLTS signals following pulses V_{p1} and V_{p2} are designated V_{S1} and V_{S2} , respectively. The double-correlation CC-DLTS signal ΔV_S is obtained by taking the difference of V_{S1} and V_{S2} ; this yields a *net* emission signal. In Sec. III an analysis is presented for extracting a trap-density profile from measurements of ΔV_S over a range of reverse biases.

III. THEORY OF MEASUREMENT

In a Schottky-barrier structure, the application of a reverse bias depletes the semiconductor surface of majority carriers, with the depletion width dependent upon the magnitude of the reverse bias. With the DDLTS technique the charging-pulse pairs are used to define a narrow interval in the depletion layer for trap detection; the interval is referred to as the spatial observation window.¹ This is illustrated in Fig. 2 with a schematic energy-band diagram of a Schottky barrier with a single discrete trap level located at energy E_t in the semiconductor band gap. A reverse bias V_R produces a depletion layer of width W_D , which is the depth below the semiconductor surface where the electric field vanishes. The depth at which the trap level intersects the quasi-Fermi energy in the depletion layer is denoted X_D . The depths X_{p1} and X_{p2} designate the intercepts for the pulse biases V_{p1} and V_{p2} , respectively, as shown in Fig. 1. The interval $X_{p1} < X < X_{p2}$ is the spatial observation window. To obtain the defect profile, the observation window is shifted in depth by varying the reverse bias upon which the charging pulses are superimposed. When the DDLTS measurement is conducted in the capacitance-transient mode, specific approximations are required for data analysis to deal with the change with time of

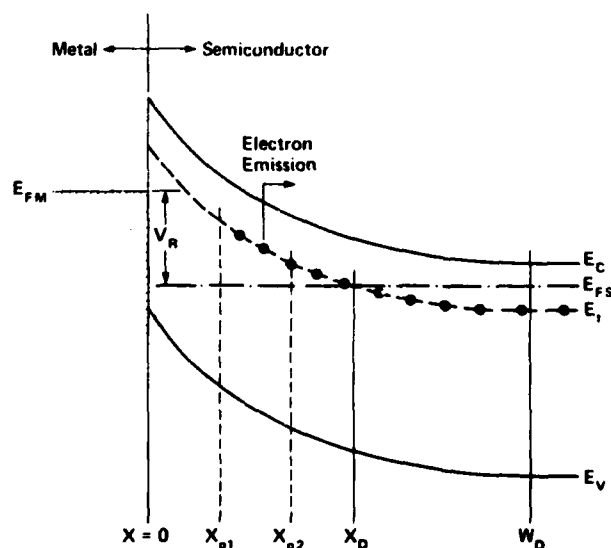


FIG. 2. Schematic energy-band diagram for a Schottky-barrier structure with a single discrete defect level at an energy E_t in the semiconductor band gap. The distance W_D is the depletion width for a reverse bias V_R , and X_D is the depth below the semiconductor surface at which the defect level intersects the quasi-Fermi energy. The distances X_{p1} and X_{p2} are the depths where the trap level intersects the quasi-Fermi energy for pulse biases V_{p1} and V_{p2} , respectively. The interval $X_{p1} < X < X_{p2}$ defines the spatial observation window for the double-correlation technique (Ref. 3).

the depletion width as the capacitance relaxes toward a steady-state value after a charging pulse.¹ A changing depletion width produces a corresponding time variation in the total number of defects contributing to the emission signal. In the constant-capacitance mode, the depletion width is held constant during the transient response, thus eliminating the need for such approximations and thereby permitting more accurate measurement of spatial depth profiles.

An analytical expression relating the measured emission signal ΔV_S to the trap density $N_t(X)$ can be readily obtained by considering a single electron trapping level in an *n*-type semiconductor, as shown in Fig. 2. The traps will be treated as being acceptorlike, that is, they are negatively charged when occupied with electrons and neutral when empty. It is assumed that all traps below the quasi-Fermi level are completely filled during a charging pulse. The analysis utilizes the depletion approximation with the inclusion of trapping centers. Thus, the space-charge density in the depletion layer consists of the shallow-dopant density $N_D(X)$ and the occupied-trap density $n_t(X,t)$. With the depletion approximation the spatial resolution for defect profiling is set by the spatial observation window, the interval $X_{p1} < X < X_{p2}$ in Fig. 2. Of course, the ultimate resolution is limited by the extrinsic Debye length λ_D , which is given by the expression

$$\lambda_D = (\epsilon_s kT / q^2 N_D)^{1/2}, \quad (1)$$

where ϵ_s is the permittivity of the semiconductor, k is Boltzmann's constant, T is the absolute temperature, and q is electronic charge.

The variation of the applied voltage with time after a charging pulse is readily computed from the following relationship between the electric potential across the device, V , and the space-charge density in the depletion layer, ρ_S :

$$\epsilon_s V = \int_0^x \rho_S dX, \quad \lim_{x \rightarrow \infty} \rho_S = 0. \quad (2)$$

This expression is derived from Gauss's law; it is not restricted to the depletion approximation and is generally valid for Schottky-barrier structures. The zero of potential is taken at the semiconductor surface. The total potential difference across the depletion layer is $V(W_D) = V_D + v(t)$, where V_D is the built-in potential and $v(t)$ is the time varying applied bias. The space-charge densities at time t after charging pulses V_{p1} and V_{p2} will be designated $\rho_{S1}(X,t)$ and $\rho_{S2}(X,t)$, respectively, and are given by the following expressions:

$$\begin{aligned} \rho_{S1} &= qN_D, & 0 < X < X_{p1} \\ &= q(N_D - n_t), & X_{p1} < X < X_D \\ &= q(N_D - N_t), & X_D < X < W_D \end{aligned} \quad (3)$$

and

$$\begin{aligned} \rho_{S2} &= qN_D, & 0 < X < X_{p2} \\ &= q(N_D - n_t), & X_{p2} < X < X_D \\ &= q(N_D - N_t), & X_D < X < W_D. \end{aligned} \quad (4)$$

When electron emission dominates the trap relaxation process, the trap occupation varies exponentially with time

$$n_i(X, t) = N_i(X) \exp(-e_n t), \quad (5)$$

where e_n is the electron emission rate, which from considerations of detailed balance is given by

$$e_n = \sigma_n v_n N_C \exp[-(E_C - E_i)/kT]. \quad (6)$$

In this equation σ_n is the electron capture cross section, v_n is the mean thermal velocity for electrons, and N_C is the effective density of states in the semiconductor conduction band. With the DLTS technique the delay times t_1 and t_2 (see Fig. 1) determine an emission rate window e_0 as follows:

$$e_0 = (t_2 - t_1)^{-1} \ln(t_2/t_1). \quad (7)$$

For spatial profiling, maximum sensitivity is obtained by adjusting the sample temperature such that $e_n = e_0$. In Fig. 1 the net emission signal is defined as

$$\Delta V_S = [v_1(t_1) - v_1(t_2)] - [v_2(t_1) - v_2(t_2)]. \quad (8)$$

When Eqs. (2)–(5) are substituted into Eq. (8), the following expression is obtained:

$$\Delta V_S = (q/\epsilon_S) [\exp(-e_n t_1) - \exp(-e_n t_2)] \times \int_{X_{p1}}^{X_{p2}} X N_i(X) dX. \quad (9)$$

This expression, relating the measured net emission signal to the defect density, applies for spatially varying as well as uniform shallow-dopant concentrations and is not restricted to low trap concentrations. The exponential terms in the bracket simply contribute a numerical factor to the proportionality constant. If the observation window $X_{p1} < X < X_{p2}$ is sufficiently narrow such that N_i is slowly varying over the interval, then N_i may be replaced by its average value $\langle N_i \rangle$, and the integral solved to obtain

$$\Delta V_S = (q/2\epsilon_S) [\exp(-e_n t_1) - \exp(-e_n t_2)] \times \langle N_i \rangle (X_{p2}^2 - X_{p1}^2). \quad (10)$$

This equation serves as the basis for defect-density profiling by the double-correlation CC-DLTS technique (experimental results are presented in Sec. IV). To measure trap energies, DLTS emission spectra are commonly recorded with charging pulses of a single amplitude. The CC-DLTS signal for uniform charging pulses V_S is also given by Eqs. (9) and (10) with X_{p2} replaced by X_D . In Sec. V is discussed an alternative approach for defect-density profiling which is based on the CC-DLTS measurement with uniform charging pulses.

IV. EXPERIMENTAL RESULTS

In this section results are presented from measurements of defect levels and their spatial distributions in self-implanted silicon. The purpose here is to illustrate the application of the CC-DLTS technique for bulk-defect measurements, in particular the measurement of defect profiles by the double-correlation CC-DLTS method. In addition to the results presented below, measurements with this technique are re-

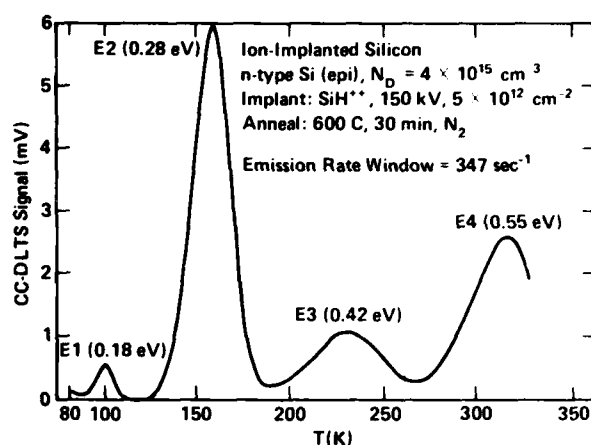


FIG. 3. Constant-capacitance DLTS spectrum for self-implanted furnace-annealed silicon. The emission activation energy is listed for each peak (see Fig. 4).

ported in Refs. 12 and 13. A study of ion-implantation damage in silicon for ranges of implantation and annealing conditions will be presented elsewhere.

A. Sample preparation

Schottky-barrier diodes were fabricated on epitaxial silicon wafers. The starting material consisted of 10- μ m-thick phosphorous-doped epilayers ($N_D = 4 \times 10^{15} \text{ cm}^{-3}$) which were grown on degenerately doped (100) oriented Czochralski-grown silicon substrates. Degenerate substrates were used to obtain back contacts which remained Ohmic at low temperatures. Wafers were implanted at room temperature with SiH^{+*} with an accelerating potential of 150 kV to a dose of $5 \times 10^{12} \text{ cm}^{-2}$. This dosage is not sufficient to drive the silicon amorphous. The implanted species was chosen to avoid nitrogen contamination (N_2^{+} and N^+) which can occur during $^{28}\text{Si}^{+}$ implantation. After implantation, the samples were annealed at 600 $^{\circ}\text{C}$ for 30 min in flowing N_2 . Aluminum field plates and back contacts were vacuum deposited, after which the test devices received a final anneal at 450 $^{\circ}\text{C}$ for 30 min in forming gas (15% H_2 , 85% N_2).

B. Defect levels

Defect energies in self-implanted silicon were measured by the CC-DLTS technique. An emission spectrum is shown in Fig. 3. Since a Schottky diode is a majority-carrier device, in an n -type semiconductor only defect levels in the upper half of the band gap can be detected. Four electron emission peaks are evident in Fig. 3. With each peak is listed the thermal activation energy for carrier emission from the corresponding defect. With the assumption that majority-carrier emission dominates the DLTS signal, the activation energy is obtained from an Arrhenius analysis of the temperature dependence of the emission rate e_n , which is given by Eq. (6). The measurement consists of recording the temperature of an emission peak for different emission-rate windows.² The Arrhenius analysis is shown in Fig. 4. To correct for the

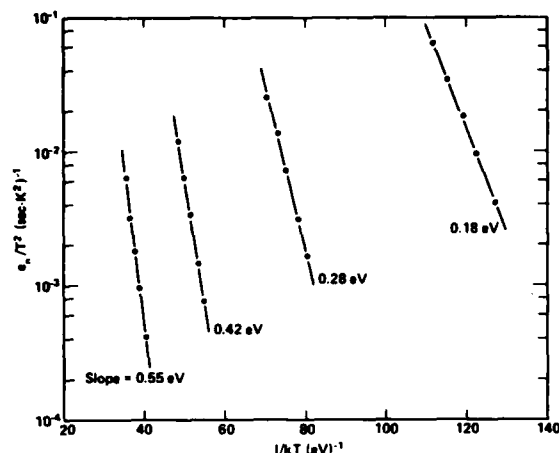


FIG. 4. Arrhenius analysis of the emission rate e_n for each of the four peaks in the CC-DLTS spectrum shown in Fig. 3.

assumed T^2 dependence of the product $v_n N_C$ in the prefactor of e_n , $\ln(e_n/T^2)$ is plotted versus $1/kT$. The activation energies were obtained from least-squares fits to the data, with estimated uncertainties of ± 0.01 eV.

The energy level in the semiconductor band gap is required for spatial depth profiling. If the capture cross section is independent of temperature, the activation energy approximately equals the defect energy. Miller *et al.*¹ have noted that the measured activation energy is actually an enthalpy while the trap depth is a free energy, the quantities being equal at $T = 0$. For the measurement of the spatial distributions, it will be assumed that the activation energies for emission peaks E1, E2, and E3 in Fig. 3 numerically equal the respective trap energies measured relative to the silicon conduction-band minimum E_C . The fourth emission peak with an activation energy of 0.55 eV identifies a trap level near midgap. In this case, the minority-carrier emission e_p cannot readily be neglected. The measured activation energy is an average of $e_n + e_p$, and the steady-state density of filled traps in the depletion layer can be a significant fraction of the total trap concentration, depending on the relative electron and hole emission rates.¹ For this reason, spatial depth profiles were measured only for the trap levels at $E_C - 0.18$, $E_C - 0.28$, and $E_C - 0.42$ eV, where electron emission could be considered the dominant process.

C. Spatial depth profiles

The spatial distributions of three trap levels in self-implanted silicon are shown in Fig. 5. Data were obtained with the double-correlation CC-DLTS technique described in Sec. II. For each trap level sample temperature was adjusted for an emission peak. The spatial observation window was incrementally shifted in depth by varying the reverse bias upon which the charging-pulse pairs were superimposed. The minimum depth for defect profiling is determined by the zero-bias depletion width, so that the profile immediately adjacent to the silicon surface cannot be directly measured. Defect densities were computed from Eq. (10). The depth at

which a trap level intersects the quasi-Fermi energy for a known bias is readily computed given the shallow-dopant density N_D and the depletion width. In the present study the Miller C-V feedback profiling technique¹⁴ was used to accurately measure depletion widths and the uniform dopant density; depletion widths were measured at the defect-profiling temperature. In Fig. 5 the horizontal bars mark the computed intervals ($X_{p1} < X < X_{p2}$) over which average defect concentrations were measured, and the vertical bars denote the uncertainties in the concentrations due to uncertainty in the measurement of the net emission signal. With each profile is shown the trap energy E_t , the profiling temperature T , and the extrinsic Debye length λ_D . Also shown is the projected range for Si⁺ implanted at 290 keV.¹⁵ This approximates the projected range of silicon for the actually implanted species SiH⁺ if it is assumed that the ionized molecule dissociates into Si⁺ and H⁺ at the silicon surface, with equal ion velocities at the instant of separation.

The densities of all three defect levels vary with depth. For the levels at $E_C - 0.28$ and $E_C - 0.42$ eV, the defect densities decrease monotonically with distance from the silicon surface over the investigated spatial ranges. These levels are ascribed to residual implantation damage, as suggested by their rapid decay over a depth comparable to the project-

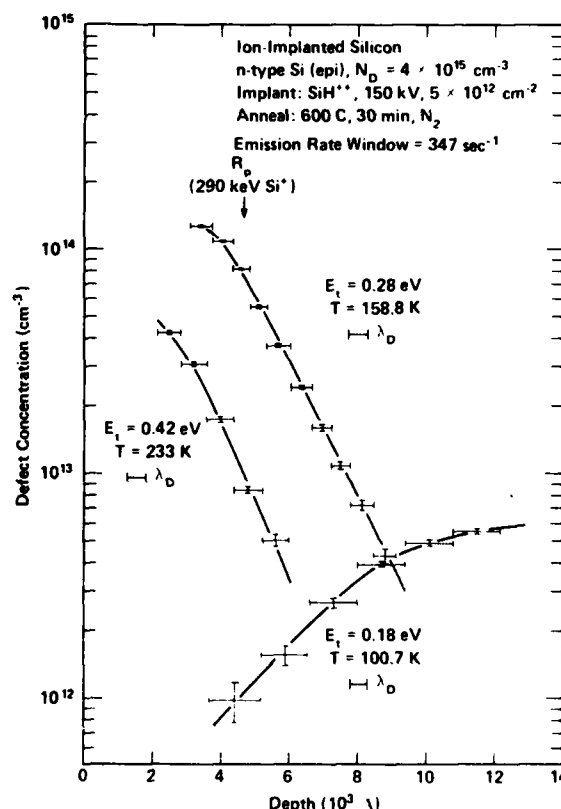


FIG. 5. Spatial depth profiles for three defect levels in self-implanted silicon (see Fig. 3), as measured by the double-correlation CC-DLTS technique. With each profile is listed the trap energy E_t , the measurement temperature T , and the extrinsic Debye length λ_D . The horizontal bars mark the computed intervals over which the average defect concentrations were measured.

ed range of the self implant. The level at $E_C - 0.18$ eV has been identified with the A center in silicon,^{16,17} which is a defect complex consisting of substitutional oxygen adjacent to a silicon vacancy.¹⁸ It is generally found that only a small fraction of the oxygen contamination in single-crystal silicon is complexed in the form of electrically active point defects.¹⁹ The A-center concentration increases over the same range as the damage centers decrease in density. This may be related to the annealing kinetics of implantation damage.

V. DISCUSSION AND CONCLUSIONS

The application of Eq. (10) for defect profiling is based on the assumption that the trap density $N_t(X)$ varies slowly over the observation window ($X_{p1} < X < X_{p2}$). Since the voltage pulses can be set for a spatial window approaching the extrinsic Debye length λ_D (as illustrated in Fig. 5), this assumption does not impose a serious limitation on the application of the technique. A similar limitation confronts the measurement of shallow-dopant profiles by capacitance-voltage techniques. When the shallow-dopant density varies rapidly on the scale of λ_D , the measured profile deviates significantly from the shallow-dopant distribution.²⁰⁻²² However, the assumption required for Eq. (10) constitutes a restriction which is in addition to the ultimate limit of spatial resolution given by λ_D .

Equation (9) can serve as the basis for an alternative approach to defect profiling which does not place a physical restriction on the spatial rate of change of N_t , other than that imposed by λ_D . This alternative approach also utilizes the CC-DLTS method but can be performed either as a double-correlation measurement or with uniform-pulse biasing. In the later case the CC-DLTS signal V_S is given by Eq. (9) with X_{p2} replaced by X_D :

$$V_S = (q/\epsilon_s) [\exp(-e_n t_1) - \exp(-e_n t_2)] \int_{X(V_p)}^{X_D} X N_t(X) dX. \quad (11)$$

Here X_p is the distance at which the trap level intersects the quasi-Fermi energy for a pulse bias V_p . Since the distance X_p can be varied by changing V_p , the emission signal can be measured as a function of X_p , with X_D held constant. Then the lower limit of integration in Eq. (11) may be treated as a variable, and V_S can be differentiated with respect to X . Evaluating the spatial derivative of Eq. (11) at X_p yields

$$\left. \frac{dV_S}{dX} \right|_{X_p} = \frac{q}{\epsilon_s} [\exp(-e_n t_1) - \exp(-e_n t_2)] X_p N_t(X_p). \quad (12)$$

Thus from the measurement of V_S as a function of X_p , Eq. (12) can be used to compute the defect profile.

The above formulation is simply the differential limit of the difference method which underlies the double-correlation technique. However, certain features of the double-correlation technique are not retained with this alternative approach. Specifically, traps at the boundary of the depletion layer which are not completely emptied and which have an enhanced transient response are not excluded in a uniform-pulse measurement.^{1,23} This feature can be regained by per-

forming the CC-DLTS measurement with dual pulses and varying the amplitude of only one of the pulses to obtain data for computing the spatial derivative of the net emission signal. Another feature of the double-correlation technique can be important in cases where the emission rate for a defect level strongly depends on the electric field in the space-charge layer. With the double-correlation technique the field variation within the observation window is only a fraction of the variation in the space-charge layer.^{1,23} With the alternative approach, the width of the observation window would typically be varied over a range comparable to the depletion width, in which case there is a significant variation of the electric field within the window. As with the method developed in Secs. II and III, the unique feature of the approach described here is that the measurement is performed in the constant-capacitance mode. This eliminates the degradation in spatial resolution which results from the depletion width varying with time during the transient response to a charging pulse (as occurs in the capacitance-transient mode) and permits measurements at high trap densities.

ACKNOWLEDGMENT

One of the authors (NMJ) expresses his appreciation to M. Schulz for helpful discussions. The authors thank K.N. Ratnakumar, Z. Norris, and C. Healy for assistance with sample preparation, and N. Lawler for typing the manuscript.

- ¹G.L. Miller, D.V. Lang, and L.C. Kimerling, 1977 *Annual Review of Material Science* (Annual Reviews Inc., Palo Alto, 1977), pp. 377-448.
- ²D.V. Lang, *J. Appl. Phys.* **45**, 3023 (1974).
- ³H. Lefevre and M. Schulz, *Appl. Phys.* **12**, 45 (1977).
- ⁴N.M. Johnson, D.J. Bartelink, and M. Schulz, *The Physics of SiO₂ and its Interfaces*, edited by S.T. Pantelides (Pergamon, New York, 1978), pp. 421-427.
- ⁵G. Goto, S. Yanagisawa, O. Wada, and H. Takanashi, *Appl. Phys. Lett.* **23**, 150 (1973).
- ⁶J.A. Pals, *Solid-State Electron.* **17**, 1139 (1974).
- ⁷J. Engemann and K. Heime, *CRC Crit. Rev. Solid-State Sci.* **5**, 485 (1975).
- ⁸M. Schulz and N.M. Johnson, *Appl. Phys. Lett.* **31**, 622 (1977).
- ⁹M. Schulz and N.M. Johnson, *Solid State Commun.* **25**, 481 (1978).
- ¹⁰M. Schulz and E. Klausmann, *Appl. Phys.* (to be published).
- ¹¹D.V. Lang, *J. Appl. Phys.* **45**, 3014 (1974).
- ¹²N.M. Johnson, R.B. Gold, and J.F. Gibbons, *Appl. Phys. Lett.* **34**, 704 (1979).
- ¹³N.M. Johnson, R.B. Gold, A. Lietoila, and J.F. Gibbons, paper presented at the Materials Research Society Symposium on Laser-Solid Interactions and Laser Processing, Boston, 1978 (AIP, New York, to be published).
- ¹⁴G.L. Miller, *IEEE Trans. Electron. Devices* **ED-19**, 1103 (1972).
- ¹⁵J.F. Gibbons, W.S. Johnson, and S.W. Mylroie, *Projected Range Statistics, Semiconductors and Related Materials*, 2 ed. (Halsted, New York, 1975).
- ¹⁶L.C. Kimerling and J.M. Poate, *Lattice Defects in Semiconductors*, 1974 (Institute of Physics, London, 1975), p. 126.
- ¹⁷L.C. Kimerling, *IEEE Trans. Nucl. Sci.* **NS-23**, 1497 (1976).
- ¹⁸G.D. Watkins, *Ref. 16*, p. 1.
- ¹⁹W. Kaiser, H.L. Frisch, and H. Reiss, *Phys. Rev.* **112**, 1546 (1958).
- ²⁰D.P. Kennedy, P.C. Murley, and W. Kleinfelder, *IBM J. Res. Dev.* **12**, 399 (1968).
- ²¹W.C. Johnson and P.T. Panousis, *IEEE Trans. Electron Devices* **ED-18**, 965 (1971).
- ²²C.P. Wu, E.C. Douglas, and C.W. Mueller, *IEEE Trans. Electron Devices* **ED-22**, 319 (1975).
- ²³M. Schulz and H. Lefevre, *Semiconductor Silicon 1977*, edited by H.R. Huff and E. Sirtl (Electrochemical Society, Princeton, 1977), pp. 142-151.

Electronic defect levels in self-implanted cw laser-annealed silicon

N. M. Johnson

Xerox Palo Alto Research Center, Palo Alto, California 94304

R. B. Gold and J. F. Gibbons

Stanford University, Stanford, California 94305

(Received 14 September 1978; accepted for publication 22 March 1979)

Electronic defect levels in self-implanted cw Ar-laser-annealed silicon have been measured by deep-level transient spectroscopy. The electron emission spectrum is dominated by two levels near the middle of the silicon forbidden energy band with activation energies of ~ 0.49 and 0.56 eV. These levels can be spatially resolved in the depletion layer of Schottky diodes due to a more rapid decrease with distance in the density of the shallower level. In samples receiving a 450°C furnace anneal (after laser irradiation) an additional level appears at 0.28 eV; the defect density is shown to decrease monotonically with depth into the silicon substrate.

PACS numbers: 71.55.Fr, 61.80.Jh, 61.70.Tm

cw laser irradiation has been shown to be an effective means for recrystallizing the amorphous layer created by high-dose ion implantation in silicon.^{1,2} In this case, recrystallization can occur by solid-phase epitaxial regrowth.¹⁻³ Further, it has been demonstrated that the cw laser-annealed layer contains a lower density of structural defects (e.g., dislocation loops) than can be obtained by a conventional thermal anneal.² In this paper, results are presented from a deep-level spectroscopic analysis of electrically active point defects in ion-implanted and cw laser-annealed silicon. A scanning cw Ar-ion laser system was used for the anneals.⁴ With this system an implanted amorphous layer can be recrystallized while retaining the as-implanted impurity profile,² which is consistent with solid-phase epitaxial regrowth of the damaged layer. Self-implantation was used to create radiation damage, of the form accompanying the implantation of the commonly used dopants in silicon (i.e., P, As, and B), without altering the shallow dopant concentration. This facilitated the measurement and analysis.

The test devices were Schottky-barrier diodes fabricated on epitaxial silicon wafers. The starting material consisted of $10\text{-}\mu\text{m}$ -thick phosphorus-doped epilayers which were grown on degenerately doped (100)-oriented Czochralski-grown silicon substrates. Semiconducting epilayers on degenerately doped substrates were used to ensure Ohmicity of the back contacts, which permitted evaluation of as-laser-annealed silicon. Wafers were implanted at room temperature with SiH^+ at 80 keV to a dose of $2 \times 10^{15} \text{ cm}^{-2}$, which is sufficient to drive the silicon amorphous to a depth of $\sim 1200 \text{ \AA}$. The implanted species was chosen to avoid nitrogen contamination (N_2^+) which can occur during $^{28}\text{Si}^+$ implantation. Laser annealing was performed with the focused and scanned beam from a cw Ar laser.⁴ Results are presented from two separate sets of laser-annealed specimens. In the first set the silicon substrate temperature T_s was maintained at $\sim 25^\circ\text{C}$ during laser annealing; the laser power level was 12 W , with a spot size of $\sim 40 \mu\text{m}$, and the scan rate was 12.5 cm/s , with a 40% overlap between adjacent scan lines.

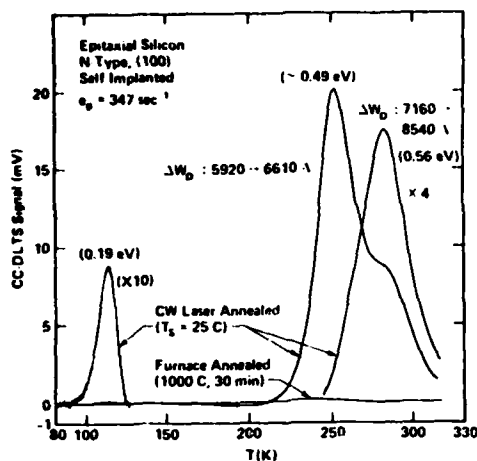


FIG. 1. CC-DLTS spectra for electron emission in self-implanted cw laser-annealed silicon and in a furnace-annealed control device.

These specimens received vacuum-evaporated Au field plates and Pd/Au back contacts. The second set of samples was laser annealed with $T_s = 350^\circ\text{C}$; the power level was 5.7 W, with a spot size of $\sim 40\ \mu\text{m}$, and the scan rate was 12 cm/s, with a 50% overlap between scan lines. With these samples, standard photolithography was used to define field plates in evaporated Al thin films, and the devices were furnace annealed at 450°C for 30 min in forming gas (15% H_2 , 85% N_2). For both of the above laser-annealing conditions, the implanted amorphous layer is recrystallized by solid-phase epitaxial regrowth. For comparison with the laser-annealed material, control devices were prepared with a conventional furnace anneal (1000°C , 30 min, N_2).

Deep-level transient spectroscopy (DLTS)⁷ was used to obtain electron emission spectra from the Schottky-barrier devices. The measurement was performed in the constant-capacitance mode (termed CC-DLTS),⁸ which is particularly applicable for high trap densities.⁹ On Schottky diodes the measurement involves first the application of a reverse bias to establish a depletion layer in the semiconductor, and a voltage pulse is periodically applied to populate additional traps by reducing the depletion width. Between charging pulses, the applied voltage is dynamically varied in order to maintain the device capacitance at a constant value as electrons (in an n -type semiconductor) are thermally emitted to the conduction band and swept out of the depletion layer. The CC-DLTS emission signal is obtained by forming the difference of the voltage transient measured at two delay times, t_1 and t_2 , after a charging pulse. The delay times define an emission rate window e_0 which is given by the expression $e_0 = (t_2 - t_1)^{-1} \ln(t_2/t_1)$.⁷ In a DLTS spectrum an emission peak appears at that temperature for which the emission rate of a trap, e_n , equals e_0 . The rate window can be varied to obtain the emission rate over a range of temperatures. Then, the activation energy for thermal emission is obtained from an Arrhenius analysis of the emission rate, which from considerations of detailed balance may be expressed as

$$e_n = \sigma_n v_n N_c \exp(-E_t/kT), \quad (1)$$

where σ_n is the electron capture cross section, v_n is the mean

thermal velocity for electrons, N_c is the effective density of states in the conduction band, E_t is the trap energy relative to the conduction-band minimum, k is Boltzmann's constant, and T is the absolute temperature.

The double-correlation technique¹⁰ was used for CC-DLTS measurement of defect-density profiles.⁹ With this technique the charging pulses are applied in pairs with the adjacent pulses set at different amplitudes. Separate DLTS signals are recorded for each pulse in the pair and then subtracted to form a *net* DLTS emission signal. In this way the adjacent pulses define a narrow spatial observation window, which is shifted in depth by varying the reverse bias upon which the pulses are superimposed. The measurement is performed with the sample temperature set for an emission peak in a DLTS spectrum. The net emission signal in the constant-capacitance mode, ΔV , depends upon the trap density in the observation window according to the following expression⁹:

$$\Delta V = (q/2\epsilon_s) [\exp(-e_n t_1) - \exp(-e_n t_2)] \langle N_t \rangle (X_{p2}^2 - X_{p1}^2), \quad (2)$$

where q is electronic charge, ϵ_s is the permittivity of the semiconductor, and $\langle N_t \rangle$ is the average trap density in the observation window. The distances X_{p1} and X_{p2} are the depths below the semiconductor surface at which the defect level intersects the quasi-Fermi energy for the two pulse biases; they define the bounds of the observation window. These depths can be computed given the shallow dopant density and trap energy. Emission spectra are recorded with uniform charging pulses, and the emission signal is given by Eq. (2) with X_{p2} replaced by X_D , which is the depth of intersection for a specified depletion bias.

CC-DLTS emission spectra are presented in Fig. 1 for a self-implanted laser-annealed sample that did not receive a forming-gas anneal. The two emission spectra were recorded with different combinations of reverse and pulse biases, which define different spatial observation windows for trap detection. The bounds of the spatial intervals quoted in Fig. 1 (i.e., ΔW_D) are the steady-state depletion depths under

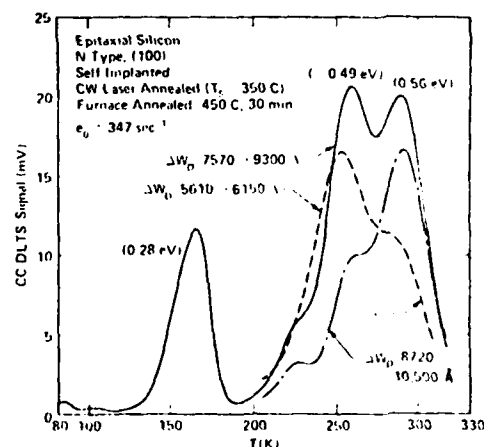


FIG. 2. CC-DLTS emission spectra for a self-implanted laser-annealed diode which also received a 450°C furnace anneal.

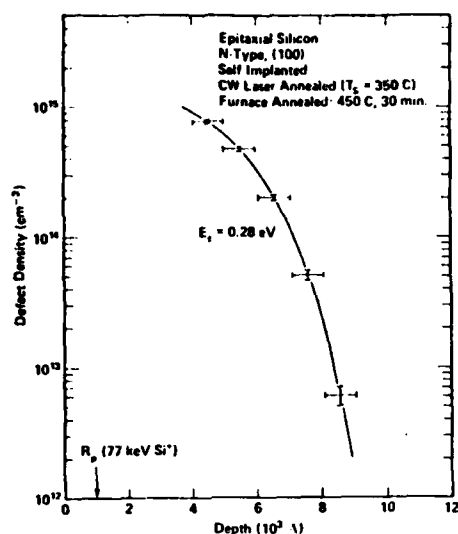


FIG. 3. Spatial depth profile of the defect level at $E_t = 0.28$ eV in self-implanted laser-annealed silicon.

reverse and pulse biases, which were computed from the high-frequency device capacitance. The intervals indicate the relative depths of the observation windows for the two spectra. The electron emission spectra are dominated by two defect levels which are located near the middle of the silicon band gap. The emission spectra recorded with different observation windows indicate that the ratio of the densities of the two defect levels varies rapidly with depth. The activation energies were obtained from measurements over spatial intervals in which a single emission peak dominated the spectrum. The activation energy for the high-temperature peak is 0.56 eV. The spatial separation of the two traps is primarily due to a rapid decrease with distance in the density of the shallower of the two midgap levels. The spatial separation is less complete for this shallower level, giving rise to an uncertainty in the activation energy which is found to be ~ 0.49 eV. A broad emission signal of reverse polarity at intermediate temperatures is ascribed to a high trap concentration near the silicon surface which contributes to a high degree of charge compensation. At low temperatures a third emission peak of low intensity is detectable, with an activation energy of 0.19 eV; this level is removed by the forming-gas anneal (see Fig. 2). Also shown in Fig. 1 is the emission spectrum for a furnace-annealed control device.

CC-DLTS emission spectra are shown in Fig. 2 for a forming-gas-annealed device. These spectra are dominated by the same two midgap defect levels as found above, with the level at ~ 0.49 eV decaying more rapidly than the 0.56-eV level with depth into the silicon substrate. However, there is an additional emission peak with an activation energy of 0.28 eV which is comparable in magnitude to the midgap peaks. This level is well resolved in the emission spectrum and can be unambiguously profiled by the double-correlation CC-DLTS technique. The defect-density distribution is shown in Fig. 3. The horizontal bars mark the spatial intervals over which average defect densities were computed from Eq. (2), and the vertical bars denote the uncertainties in

the densities due to uncertainty in the measurement of the net emission signal. The defect density decreases monotonically with depth below the laser-irradiated surface, over the investigated interval. Also shown is the projected range for Si^+ implanted at 77 keV.¹¹ This approximates the projected range of silicon for the actually implanted species, SiH^+ , if it is assumed that the ionized molecule dissociates into silicon and hydrogen atoms at the silicon surface, with equal particle velocities at the instant of separation.

High densities of electronic defect levels remain after cw laser annealing of ion-implanted silicon. The levels are ascribed to incomplete removal of implantation damage by the laser anneal, although the microscopic origins of the defects have not been identified. The levels at ~ 0.49 and 0.56 eV are present in the as-laser-annealed material (Fig. 1) and in samples which also receive a 450 °C anneal (Fig. 2). After the 450 °C anneal, an additional level of comparable density appears at 0.28 eV. The densities of all three levels decrease with depth into the silicon substrate from $>10^{15}$ cm^{-2} in the near-surface region, as shown for the level at 0.28 eV in Fig. 3. By comparison, the defect density is orders of magnitude lower in self-implanted control devices which receive a conventional furnace anneal at 1000 °C (Fig. 1). The level at 0.19 eV, detected in as-laser-annealed silicon (Fig. 1), may be due to the vacancy-oxygen complex,¹² although it differs slightly in energy from a level at 0.18 eV which has been previously assigned to this defect.¹³ The projected range for Si^+ shown in Fig. 3 approximates the depth of the amorphous layer after self-implantation and reveals that the measured defects reside in material that was not driven amorphous. The measured energy levels and spatial distributions suggest that the residual point defects should serve as efficient charge generation and recombination centers in ion-implanted and cw laser-annealed p - n junction devices.

The authors express their appreciation to M. Schulz for helpful discussions and to A. Gat and A. Lietoila for performing the laser anneals. The work at Stanford University was funded by ARPA Contract DAHC MDA 903-78-C-0128.

¹G.A. Kachurin, E.V. Nidaev, A.V. Khodyachikh, and L.A. Kovaleva, *Sov. Phys.-Semicond.* **10**, 1128 (1976).

²A. Gat, J.F. Gibbons, T.J. Magee, J. Peng, V. Deline, P. Williams, and C.A. Evans, Jr., *Appl. Phys. Lett.* **32**, 276 (1978).

³D.H. Auston, J.A. Golovchenko, P.R. Smith, C.M. Surko, and T.N.C. Venkatesan, *Appl. Phys. Lett.* **33**, 539 (1978).

⁴J.S. Williams, W.L. Brown, H.J. Leamy, J.M. Poate, J.W. Rodgers, D. Rousseau, G.A. Rozgonyi, J.A. Shelnett, and T.T. Sheng, *Appl. Phys. Lett.* **33**, 542 (1978).

⁵A. Gat, A. Lietoila, and J.F. Gibbons, *J. Appl. Phys.* **50**, (1979).

⁶A. Gat and J.F. Gibbons, *Appl. Phys. Lett.* **32**, 142 (1978).

⁷D.V. Lang, *J. Appl. Phys.* **45**, 3014 & 3023 (1974).

⁸N.M. Johnson, D.J. Bartelink, and M. Schulz, *The Physics of SiO₂ and its Interfaces* (Pergamon Press, New York, 1978), ed. S.T. Pantelides, pp. 421-427.

⁹N.M. Johnson, D.J. Bartelink, R.B. Gold, and J.F. Gibbons, *J. Appl. Phys.* **50** (1979).

¹⁰H. Lefevre and M. Schulz, *Appl. Phys.* **12**, 45 (1977).

¹¹J.F. Gibbons, W.S. Johnson, and S.W. Mylroie, *Projected Range Statistics, Semiconductors and Related Materials*, 2nd ed. (Halsted, New York, 1975).

¹²G.D. Watkins and J.W. Corbett, *Phys. Rev.* **121**, 1001 (1961).

¹³L.C. Kimerling, *IEEE Trans. Nucl. Sci.* **NS-23**, 1497 (1976).

DEEP LEVELS IN ION-IMPLANTED, CW LASER-ANNEALED SILICON

N. M. Johnson

Xerox Palo Alto Research Center, Palo Alto, California 94304

R. B. Gold, A. Lietoila, and J. F. Gibbons

Stanford University, Stanford, California 94305

ABSTRACT

Electronic defect levels in self-implanted, CW Ar-laser-annealed silicon have been measured by deep-level transient spectroscopy. Results are presented from measurements on n-type Schottky diodes which were fabricated on both Czochralski-grown and epitaxial silicon wafers. High densities of electron traps remain after CW laser-induced recrystallization of an implanted amorphous layer. The defect densities decrease with depth into the silicon substrate. The residual damage is only partially removed by a 600-C anneal and is substantially removed after an 800-C anneal.

INTRODUCTION

CW laser irradiation has been shown to be an effective means for recrystallizing the amorphous layer created by high-dose ion implantation in silicon.^{1,2} It has been shown that for this annealing procedure, recrystallization can occur by solid-phase epitaxial regrowth.³⁻⁵ It has also been demonstrated that the CW laser-annealed layer contains a lower density of structural defects (e.g., dislocation loops) than can be obtained by a conventional thermal anneal.⁵ In this paper, results are presented from a deep-level spectroscopic study of electrically active point defects in ion-implanted and CW laser-annealed silicon. A scanning CW Ar-ion laser system was used for the anneals.⁶ With this system an implanted amorphous layer can be recrystallized while retaining the as-implanted impurity profile,⁵ which is consistent with solid-phase epitaxial regrowth of the damaged layer. Self implantation was used to create radiation damage of the form accompanying the implantation of the commonly used dopants in silicon (i.e., P, As, and B). Samples were prepared on both epitaxial silicon and Czochralski-grown silicon, and the effectiveness of furnace anneals for removing residual implantation damage after laser annealing was investigated.

SAMPLE PREPARATION

Schottky-barrier diodes were fabricated on both epitaxial silicon and bulk single-crystal silicon. The epitaxial silicon consisted of 10- μ m thick, phosphorus-doped epilayers which were grown on degenerately doped, (100)-oriented silicon substrates. The bulk material was phosphorus-doped, (100)-oriented, Czochralski-grown silicon. The back surface of bulk silicon wafers was implanted with phosphorus to produce a degenerately doped layer; the dopant was electrically activated with an anneal at 800 C for 30 min in flowing N₂. Epitaxial silicon wafers with degenerate substrates and ion-implanted back surfaces on single-crystal silicon were used to obtain back contacts which remained ohmic at low-

temperatures. This also permitted the evaluation of as-laser-annealed silicon. The front surface of the wafers was implanted at room temperature with SiH^+ at 80 keV to a dose of $2 \times 10^{15} \text{ cm}^{-2}$. This dose is sufficient to drive the silicon amorphous to a depth of approximately 1200 Å. The implanted species was chosen to avoid nitrogen contamination (N_2^+) which can occur during $^{28}\text{Si}^+$ implantation. Laser annealing was performed with the focussed and scanned beam from a CW Ar-ion laser.⁶ The substrates were maintained at 350 C during laser annealing. The power level was 5.7 W, with a spot diameter of $\sim 40 \mu\text{m}$, and the scan rate was 12 cm/sec, with a 50% overlap between adjacent scan lines. Under these annealing conditions, the implanted amorphous layer is recrystallized by solid-phase epitaxial regrowth. Part of the specimens received a furnace anneal after laser irradiation. These specimens were annealed at either 600 or 800 C in flowing N_2 for 30 min. Schottky-barrier diodes were fabricated by vacuum evaporating aluminum on both surfaces of the wafer. Standard photolithographic techniques were used to define the rectifying contacts. Unless otherwise stated, the test devices received a final anneal at 450 C for 30 min in forming gas (15% H_2 , 85% N_2).

MEASUREMENT TECHNIQUE

Transient-capacitance techniques were used to measure electrically active defects on Schottky diodes. The basic method used in this study was developed by Lang⁷ and is termed deep-level transient spectroscopy (DLTS). The double-correlation DLTS (DDLTS) technique⁸ was used to measure spatial depth profiles of defect levels. In the present study both DLTS and DDLTS were performed in the constant-capacitance mode, which is particularly applicable when measuring high trap densities. A detailed analysis of constant-capacitance DLTS (CC-DLTS) measurements of bulk-semiconductor defects has been presented elsewhere.⁹

The essential features of the above techniques for detecting defects are illustrated in Fig. 1 with an energy-band diagram for a Schottky-barrier structure with a single trap level at energy E_t in the bandgap of an n-type semiconductor. The DLTS measurement involves first the application of a reverse bias V_R to establish a depletion layer of width W_D . The trap level intersects the quasi-Fermi energy E_{FS} at X_D . Traps located below E_{FS} are filled with electrons and those above are empty. Voltage pulses periodically reduce the depletion width in order to populate additional traps. After returning to the quiescent bias, these trapped electrons are thermally emitted to the conduction band and swept out of the depletion layer. This gives rise to a voltage transient in the constant-capacitance mode of measurement. With the double-correlation technique, voltage pulses are applied in pairs, with adjacent pulses set at different amplitudes. The depths X_{p1} and X_{p2} in Fig. 1 designate the intercepts of the trap level with E_{FS} for two such voltage pulses. The interval $X_{p1} \leq X \leq X_{p2}$ is the spatial observation window, which can be shifted in depth by varying the reverse bias to obtain defect density profiles.

The CC-DLTS signal is obtained by forming the difference of the applied voltages measured at two delay times t_1 and t_2 after a charging pulse. For an exponential transient response, the delay times define an emission rate constant e_0 which is given by the expression $e_0 = (t_2 - t_1)^{-1} \ln(t_2/t_1)$.⁷ In a DLTS spectrum an emission peak appears at that temperature for which the emission rate of a given trap, e_n , equals e_0 . The emission rate constant can be varied to obtain the emission rate over a range of temperatures. Then the activation energy for thermal emission is obtained from an Arrhenius analysis of the emission rate, which from considerations of detailed balance may be expressed as

$$e_n = \sigma_n v_n N_c \exp[-(E_c - E_t)/kT], \quad (1)$$

where σ_n is the electron capture cross section, v_n is the mean thermal velocity for electrons, N_c is the effective density of states in the semiconductor conduction band, E_c is the conduction-band minimum, k is Boltzmann's constant, and T is the absolute temperature. For defect profiling by the double-correlation CC-DLTS technique, the measurement yields a net emission signal ΔV_S which depends on the average trap density $\langle N_t \rangle$ in a narrow spatial observation window, $X_{p1} \leq X \leq X_{p2}$, according to the following expression:⁹

$$\Delta V_S = (q/2\epsilon_s) [\exp(-e_n t_1) - \exp(-e_n t_2)] \langle N_t \rangle (X_{p2}^2 - X_{p1}^2), \quad (2)$$

where q is electronic charge and ϵ_s is the permittivity of the semiconductor. The CC-DLTS signal for uniform charging pulses is also given by Eq. (2) with X_{p2} replaced by X_D .

EXPERIMENTAL RESULTS

For n-type silicon DLTS measurements on Schottky-barrier diodes can detect electron traps in the upper half of the silicon bandgap. In Fig. 2 are shown three electron emission spectra for self-implanted, laser-annealed epitaxial silicon. The three emission spectra were recorded with different spatial intervals for trap detection. The bounds of the intervals quoted in the figure are the steady-state depletion widths for the reverse and pulse biases; the widths were computed from measurements of the high-frequency device capacitance. These depletion intervals are denoted ΔW_D and indicate the relative depths of the observation windows for the three spectra. The complete spectrum (solid curve) is dominated by three defect levels, two of which are located near the middle of the silicon bandgap. The emission spectra recorded with different depletion intervals indicate that the ratio of the concentrations of these two midgap levels varies rapidly with depth. The activation energies were computed from measurements over spatial intervals in which a single emission peak dominated the spectrum. The activation energy for the high-temperature peak is 0.56 eV. The spatial separation of the two traps is primarily due to a rapid decrease with distance in the concentration of the shallower of the two midgap levels. The spatial separation is less complete for this shallower level giving rise to an uncertainty in the activation energy which is found to be ~0.49 eV. The peak emission signal for the 0.49-eV level which appears in the depletion interval nearest the surface (dashed curve) corresponds to an average defect density of $>10^{15} \text{ cm}^{-3}$ in a trap observation window of $\sim 2500 \rightarrow 3100 \text{ \AA}$. The third dominant emission peak has an activation energy of 0.28 eV.

The effect of a furnace anneal after laser irradiation is illustrated in Fig. 3. The results are from specimens on epitaxial silicon which were first self implanted and laser annealed and then furnace annealed at 600 and 800 C before metallization. In specimens annealed at 600 C, the emission spectrum is dominated by the same three levels shown in Fig. 2. Except for the level at ~0.49 eV there is little change in the trap concentrations after a 600-C anneal. This level has significantly decreased in density relative to the others, for a near-surface depletion interval, which suggests a low dissociation energy for the corresponding (unidentified) defect complex. After an 800-C anneal, all defect densities are significantly reduced. The insert in Fig. 3 shows the spatial distribution of the defect level at $E_c - 0.28 \text{ eV}$ in a specimen annealed at 600 C. The profile was measured by the double-correlation CC-DLTS technique. The horizontal bars mark the computed intervals over which the average defect concentrations were measured. The density of the defect level decreases rapidly with depth. Also shown in the insert is the projected range for Si^+ implanted at 77 keV.¹⁰ This approximates the projected range of silicon for the actually implanted species, SiH^+ , if it is assumed that the ionized molecule dissociates into silicon and hydrogen atoms at the silicon surface, with equal particle velocities at the instant of separation.

Czochralski-grown silicon yields essentially the same results as obtained from the epitaxial material. This is illustrated in Fig. 4. The self-implanted, laser-annealed specimen

received an anneal at 600 C. The emission spectrum is dominated by the levels at 0.28 eV and 0.56 eV, and the level at ~ 0.49 eV appears as a shoulder on the high-temperature peak. As suggested by the magnitudes of the emission signals, the trap concentrations are comparable to those for epitaxial silicon after a 600-C anneal (Fig. 3). Also shown with the same measurement sensitivity is the featureless emission spectrum for the Czochralski-grown starting material.

The electron emission spectrum for laser-annealed specimens which are not subjected to the forming gas anneal differs from those shown above. The results presented in Figs. 2-4 were obtained from specimens which received a forming gas anneal after metallization. A 450-C anneal removes many damage-related defect complexes in silicon.^{11,12} Since the samples were prepared with degenerately doped back surfaces, the forming gas anneal is not required to establish ohmic back contacts. In Fig. 5 are shown results from a self-implanted, laser-annealed specimen on Czochralski-grown silicon. The two high-temperature peaks dominate the emission spectrum, with the level at 0.56 eV appearing as a shoulder on the level at ~ 0.49 eV. At intermediate temperatures a broad emission signal of reverse polarity is observed. This otherwise anomalous segment of the spectrum is ascribed to a high trap concentration near the silicon surface which contributes to a high degree of charge compensation. At low temperatures a new emission signal is detected. The activation energy for this level is 0.19 eV. This level is not observed in the starting material (the spectrum for which is also shown in Fig. 5) and is not present in specimens annealed at 450 C (Fig. 4); this suggests a low dissociation energy for the corresponding defect center. Also given in Fig. 5 is the average trap density in the specified spatial observation window for the level at $E_C - 0.19$ eV. This defect level is also detected in as-laser-annealed epitaxial silicon.¹³

DISCUSSION AND CONCLUSIONS

The results presented in the previous section reveal that high densities of electron traps remain after CW laser-induced recrystallization of an implanted amorphous layer. The CC-DLTS spectra in Figs. 2-4 are dominated by three electron emission peaks with thermal activation energies of 0.28, ~ 0.49 , and 0.56 eV. A new defect level at 0.19 eV is observed in as-laser-annealed silicon (Fig. 5 and Ref. 13); this level is not detectable after a 450-C anneal (Fig. 2). The level at 0.28 eV is absent in the as-laser-annealed material (Fig. 5); its appearance after a 450-C anneal (Fig. 2) indicates a reverse-annealing behavior. The residual damage is only partially removed by a 600-C anneal. A substantial recovery is achieved by an anneal at 800 C, which is also obtained by an 800-C anneal in the absence of laser annealing.

The implantation and measurement conditions were such that the detected defect levels were located several thousand Angstroms below the implanted amorphous layer; that is, the measured defects were situated in material which was not driven amorphous by ion implantation. These defects may be considered part of the nominally Gaussian damage profile which extends into the silicon substrate. The arrangement is illustrated in the insert in Fig. 3, which shows the rapid decrease with depth in the density of the level at $E_C - 0.28$ eV. Also shown in the insert is the projected range for the self-implanted silicon. The implanted amorphous layer extends to a depth comparable to the projected range. The minimum depth for defect profiling is determined by the zero-bias depletion width so that defect centers immediately adjacent to the silicon surface cannot be analyzed. However, the measured defect levels include those which would extend into the depletion layer of a p-n junction device if a shallow dopant was implanted instead of silicon ions (e.g., if P or As ions were implanted into p-type silicon). The two midgap defect levels which dominate the electron emission spectra in Figs. 2-5 should serve as efficient charge generation centers in the depletion layer of a reverse biased p-n junction, giving rise to large leakage currents. On the other hand, since only the surface layer of the silicon is raised to high temperatures during laser annealing, junction fabrication does not entail any degradation of the bulk electrical

properties, thereby minimizing the diffusion-current contribution to the reverse-bias leakage current. The relative significance of these two counteractive features of CW laser annealing would depend on details of junction fabrication.

ACKNOWLEDGEMENT

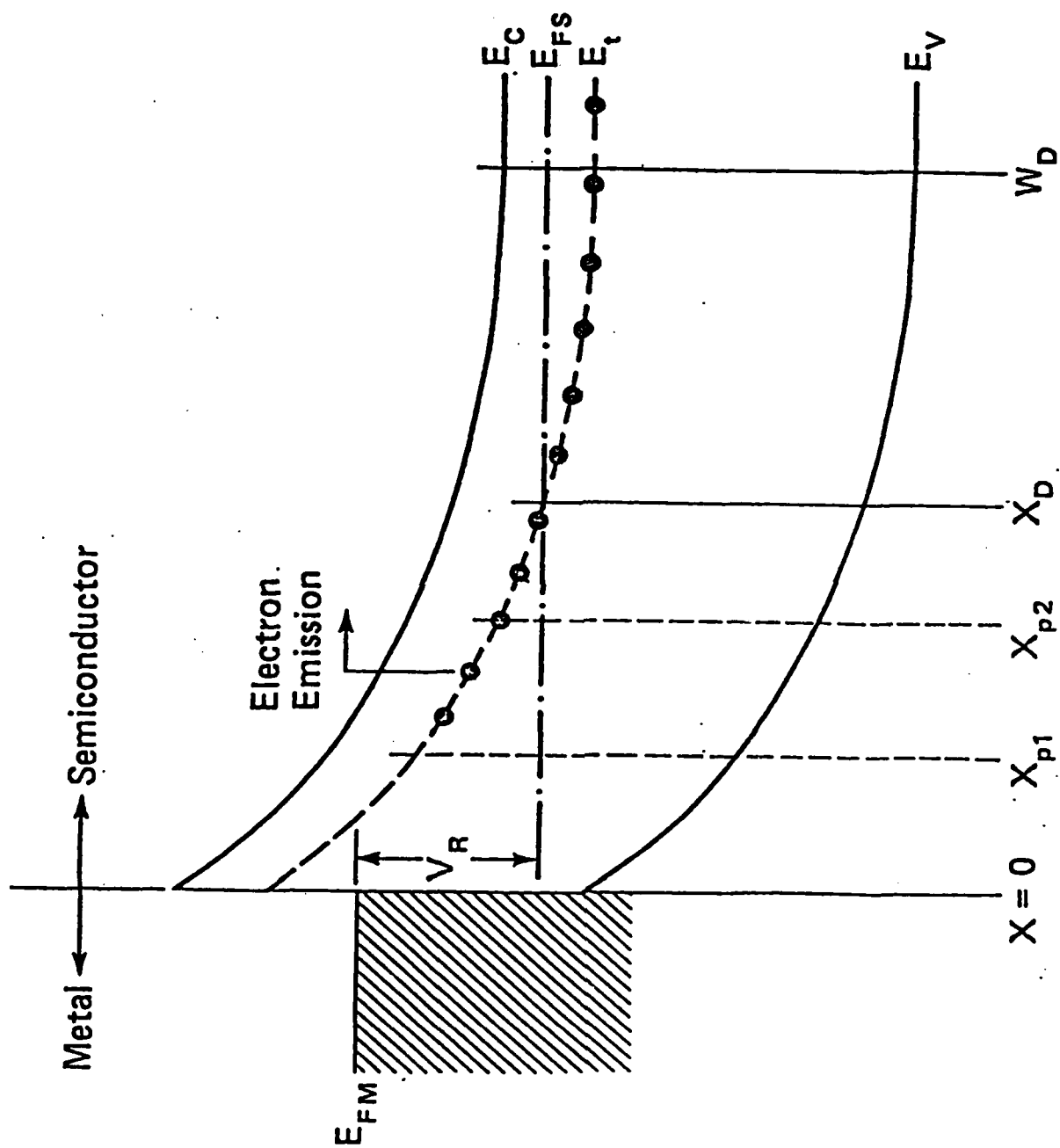
The authors express their appreciation to M. Schulz for helpful discussions and thank R. Giles for assistance with sample preparation. The work at Stanford University was funded by ARPA Contract DAHC MDA 903-78-C-0128.

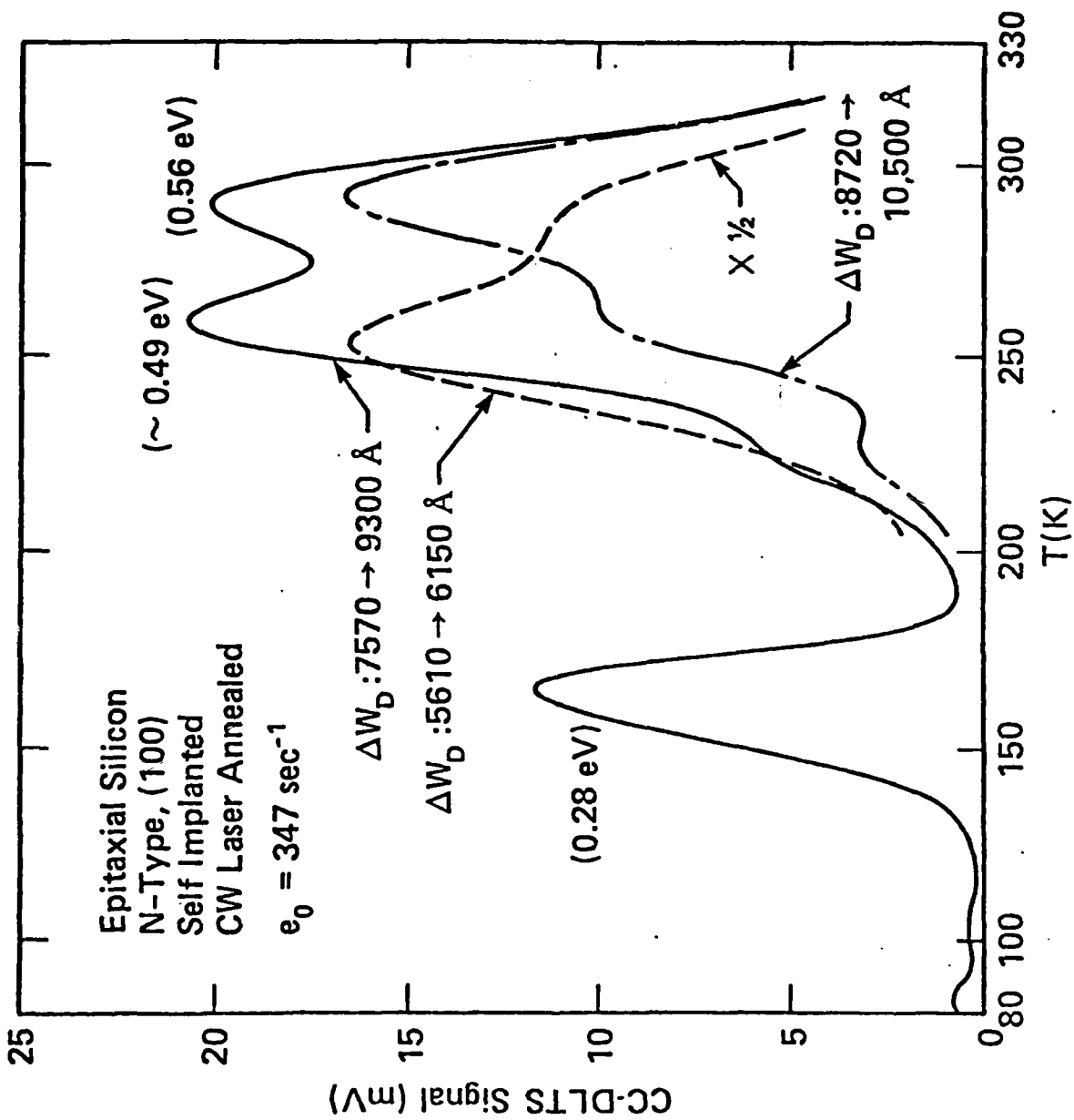
REFERENCES

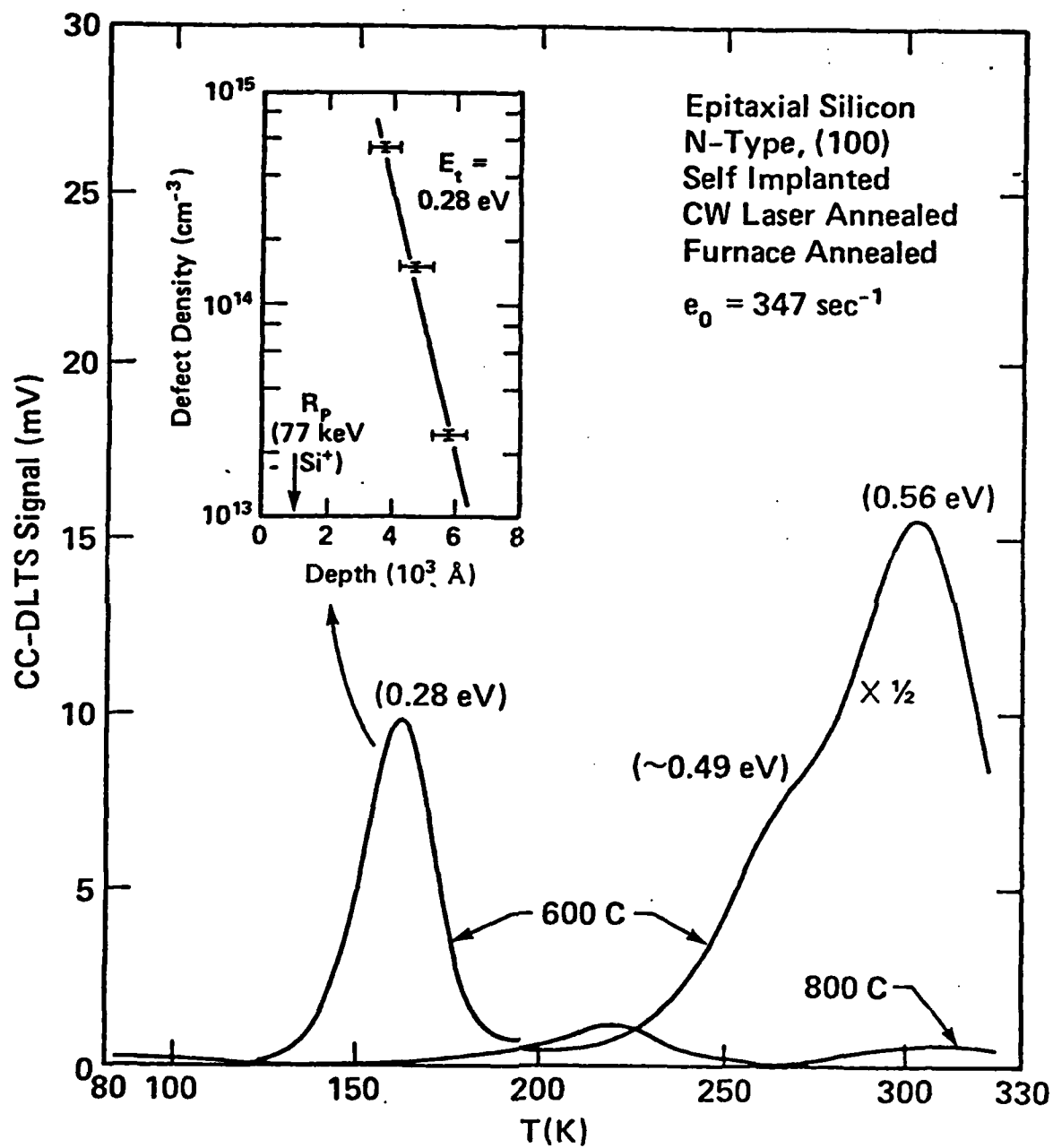
1. G. A. Kachurin, E. V. Nidaev, A. V. Khodyachikh, and L. A. Kovaleva, *Sov. Phys. Semicond.* **10**, 1128 (1976).
2. A. Gat, J. F. Gibbons, T. J. Magee, J. Peng, V. Deline, P. Williams, and C. A. Evans, Jr., *Appl. Phys. Lett.* **32**, 276 (1978).
3. D. H. Auston, J. A. Golovchenko, P. R. Smith, C. M. Surko, and T. N. C. Venkatesan, *Appl. Phys. Lett.* **33**, 539 (1978).
4. J. S. Williams, W. L. Brown, H. J. Leamy, J. M. Poate, J. W. Rodgers, D. Rousseau, G. A. Rozgonyi, J. A. Shelnett, and T. T. Sheng, *Appl. Phys. Lett.* **33**, 542 (1978).
5. A. Gat, J. F. Gibbons, and A. Lietoila, *J. Appl. Phys.*, (accepted for publication).
6. A. Gat and J. F. Gibbons, *Appl. Phys. Lett.* **32**, 142 (1978).
7. D. V. Lang, *J. Appl. Phys.* **45**, 3014 & 3023 (1974).
8. H. Lefevre and M. Schulz, *Appl. Phys.* **12**, 45 (1977).
9. N. M. Johnson, D. J. Bartelink, R. B. Gold, and J. F. Gibbons, (submitted for publication).
10. J. F. Gibbons, W. S. Johnson, and S. W. Mylroie, Projected Range Statistics, Semiconductors and Related Materials, 2nd Ed. (Halsted Press, New York, 1975).
11. L. C. Kimerling and J. M. Poate, Lattice Defects in Semiconductors, 1974 (Institute of Physics, London, 1975), p. 126.
12. L. C. Kimerling, *IEEE Trans. Nucl. Sci.* **NS-23**, 1497 (Dec. 1976).
13. N. M. Johnson, R. B. Gold, and J. F. Gibbons, *Appl. Phys. Lett.*, (accepted for publication).

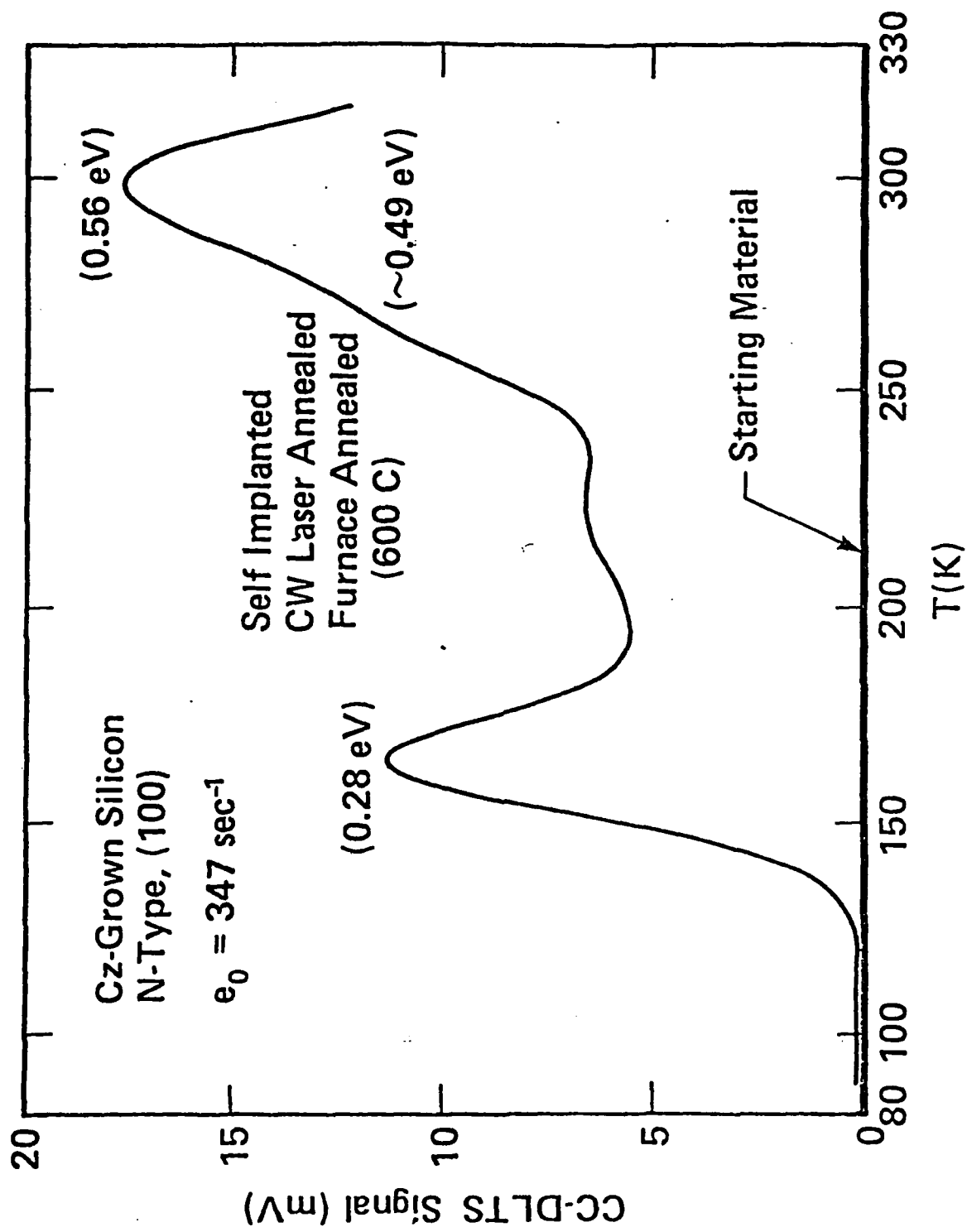
FIGURE CAPTIONS

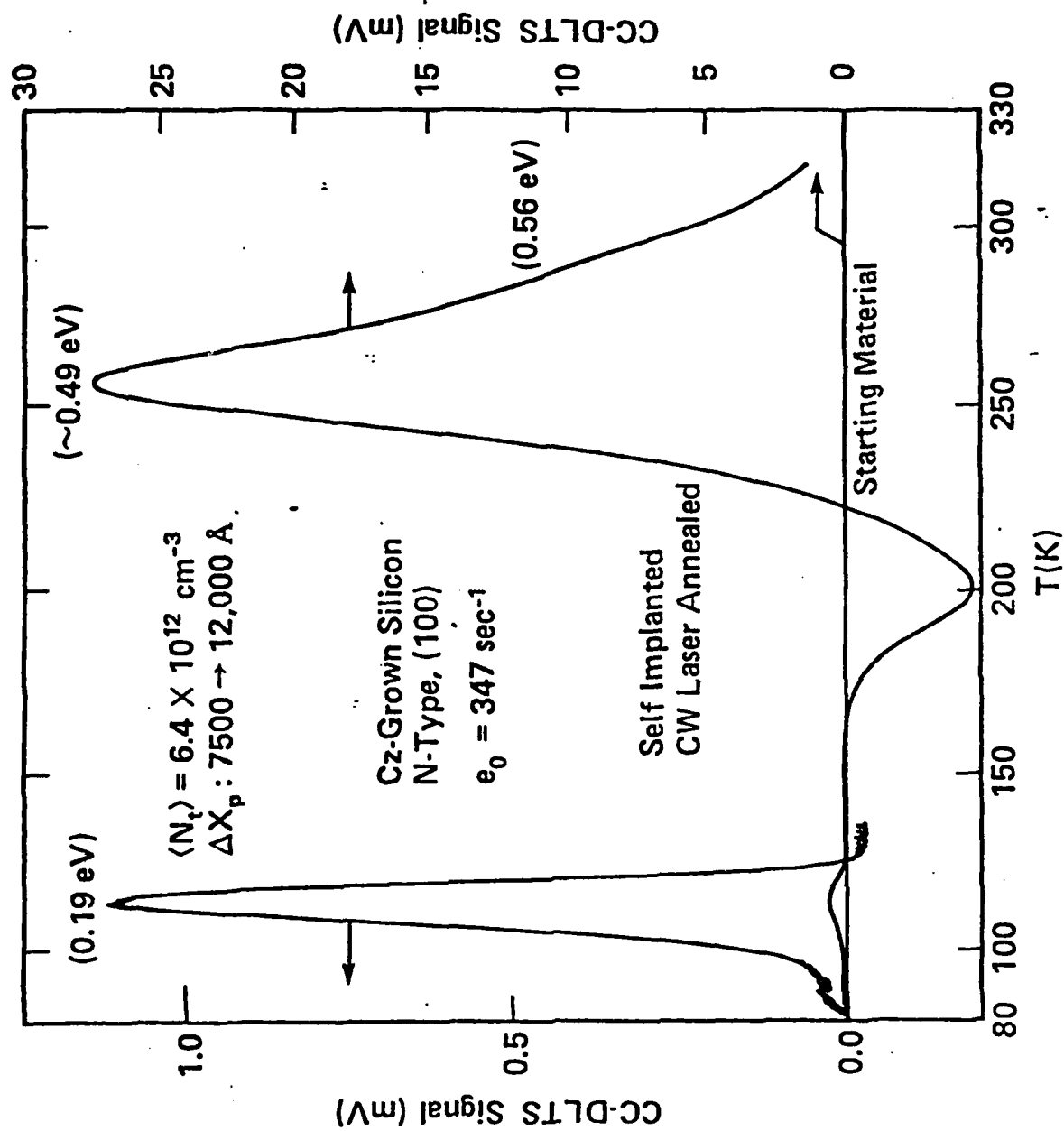
- Fig. 1. Schematic energy-band diagram for a Schottky-barrier structure on an n-type semiconductor.
- Fig. 2. CC-DLTS spectra for electron emission in self-implanted, CW laser-annealed epitaxial silicon.
- Fig. 3. Electron emission spectra for epitaxial silicon which was furnace annealed after self implantation and CW laser annealing. The insert shows the defect density profile for the level at $E_C - 0.28$ eV in a 600-C annealed specimen.
- Fig. 4. Electron emission spectrum for Cz-grown silicon which was annealed at 600 C after self implantation and CW laser annealing.
- Fig. 5. Electron emission spectrum for self-implanted, CW laser-annealed Cz-grown silicon. The sample did not receive a 450-C anneal after metallization.











Deep levels in scanned electron-beam annealed silicon

N. M. Johnson, J. L. Regolini,^{a),b)} and D. J. Bartelink
Xerox Palo Alto Research Center, Palo Alto, California 94304

J. F. Gibbons and K. N. Ratnakumar^{a)}
Stanford Electronics Laboratories, Stanford, California 94305

(Received 1 October 1979; accepted for publication 21 December 1979)

Electronic defect levels in scanned electron-beam annealed (SEBA) silicon have been measured by deep-level transient spectroscopy. In As⁺-implanted *p-n* junctions, hole-trap densities in the 10^{13}-cm^{-3} range have been achieved with the dominant levels energetically situated for inefficient charge generation and recombination. In Schottky diodes on unimplanted silicon, SEBA-induced electron traps have been detected with principal levels at $E_c - 0.19\text{ eV}$ and $E_c - 0.44\text{ eV}$; the defect densities decrease exponentially with distance from the beam-annealed surface. Both levels are ascribed to vacancy-impurity complexes (e.g., the 0.44-eV level identifies the *P-V* center), and a simple vacancy-diffusion model is proposed to explain the defect distributions.

PACS numbers: 71.55.Fr, 72.20.Jv, 61.70.Tm

It has been demonstrated that a scanned electron beam can be used to anneal ion-implantation damage in silicon, with results that are substantially identical to those obtained with a scanning cw laser.¹ More recently, it has been demonstrated that with a commercial scanning electron microscope (SEM), modified for high-current operation, annealing can be performed with submicron spatial resolution.² Detailed studies of the physical properties of arsenic-implanted silicon have demonstrated the following features of SEM annealing²⁻⁴: (1) The entire implanted amorphous layer is recrystallized, with the annealed layer displaying a structural integrity comparable to that of the starting material, (2) there is no significant dopant redistribution, which is consistent with solid-phase epitaxial regrowth of the amorphous layer, and (3) the electron mobility displays the predicted dependence on dopant concentration. These are sub-

stantially the same results as obtained when using a commercial electron-beam welder to anneal As⁺-implanted silicon.¹ The above studies clearly identify scanned electron-beam annealing (SEBA), and in particular SEM annealing, as a potentially powerful processing technique for fabricating fine-feature silicon devices. In this letter, results are presented from a deep-level spectroscopic study of residual point defects in SEBA-processed silicon. Similar studies on self-implanted cw laser-annealed silicon have revealed high densities of deep levels, as compared to specimens receiving a conventional furnace anneal.^{5,6} In the present study, point defects remaining after SEBA processing were measured in As⁺-implanted *p-n* junction diodes and in unimplanted *n*-type Schottky diodes.

The test devices were fabricated on (100)-oriented, Czochralski-grown silicon. The back surface of the silicon wafers was implanted with the substrate dopant, which was electrically activated with an anneal at 800 °C (30 min, N₂), in order to produce a degenerately doped layer for Ohmic contact. To further facilitate electrical connection to the

^{a)}Consultant to the Xerox Corporation.

^{b)}Present address: Centro Atomico-8400 Bariloche, Argentina.

TABLE I. System parameters for scanned electron-beam annealing.

	Welder	SEM
Electron energy (keV)	31	20
Beam current (μA)	300-400	60
Scan rate (cm/sec)	20	10 ^a
Beam diameter (μm)	<300 ^b	10
Scan-line separation (μm)	< 100	1.25

^aLine scan in SEM.^bA single scan line of annealed Si was 100 μm wide.

back contact, aluminum films were vacuum evaporated over the back surface of the wafers and then sintered at 450 °C (30 min, forming gas). Preparation of back contacts was completed prior to front surface processing. For p - n junctions, As⁺ was implanted (100 keV, $5 \times 10^{14} \text{ cm}^{-2}$) into p -type (B-doped, 1-3 $\Omega \text{ cm}$) silicon. The ion energy and dose were sufficient to drive the silicon surface amorphous to a depth of approximately 1000 Å. Scanned electron-beam annealing, performed with both a commercial electron-beam welder¹ and a scanning electron microscope,^{2,3} was used to recrystallize the amorphous layer and activate the implanted arsenic. The parameters of the SEBA systems are summarized in Table I; the substrates were maintained at room temperature during annealing. The p - n junction diodes were completed by depositing aluminum over the front surface and using conventional photolithographic and plasma-etching techniques to define a mesa structure. The Schottky diodes were prepared on n -type (P-doped, 1-3 $\Omega \text{ cm}$) silicon and received no front-surface ion implantation. After SEBA processing, aluminum films were deposited, and photolithography was used to define the Schottky contact. For control devices, p - n junction diodes received a furnace anneal at 1000 °C (30 min, N₂) after As⁺ implantation, and the SEBA step was omitted in the fabrication of Schottky diodes.

Deep-level transient spectroscopy (DLTS)⁷ was used to

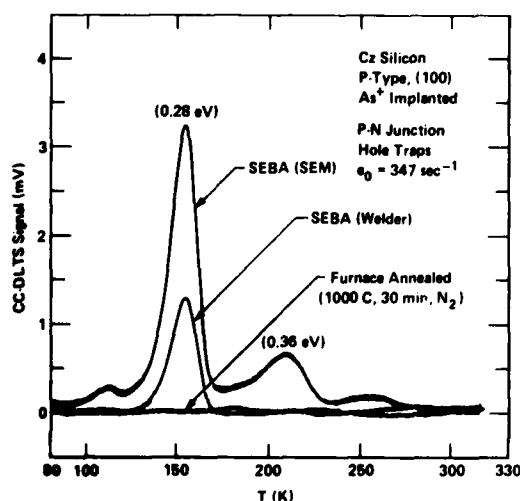


FIG. 1 CC-DLTS spectra for hole emission in As⁺-implanted scanned electron-beam annealed silicon. The spectrum for a furnace-annealed p - n junction diode is also shown.

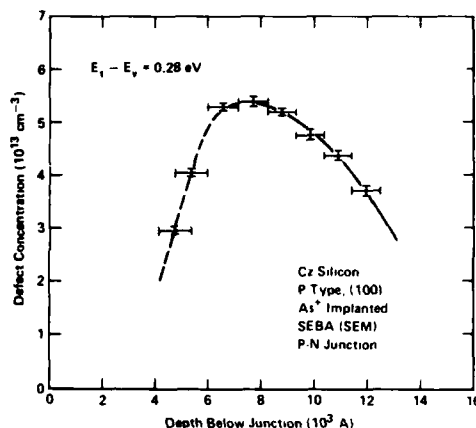


FIG. 2. Spatial depth profile of the defect level at $E_1 = +0.28 \text{ eV}$ in As⁺-implanted scanned electron-beam annealed silicon.

evaluate the above devices. The measurement provided both trap emission spectra and spatial depth profiles of selected defects and was performed in the constant-capacitance mode (CC-DLTS), which is particularly applicable when measuring trap densities comparable to the shallow dopant concentration.^{5,6,8}

CC-DLTS spectra are shown in Fig. 1 for hole emission in As⁺-implanted p - n junction diodes. Spectra were recorded, with the same emission rate window e_0 , for diodes which were SEBA processed with the electron-beam welder and SEM and for a furnace-annealed control. The activation energies for hole emission were obtained from an Arrhenius analysis of the emission rate; the quoted energies have been corrected for the assumed temperature-squared dependence of the preexponential factor in the emission coefficient.⁸ The hole trap at 0.28 eV dominates the emission spectra in the SEBA-processed diodes, with an additional peak appearing at 0.36 eV in the SEM-annealed sample. Neither level appears in the control device. The defect at 0.28 eV is present in comparable densities in the SEM- and welder-annealed diodes. The spatial depth profile of this level is shown in Fig. 2. The profile is measured relative to the metallurgical junction, which is estimated to be 1500 Å below the silicon surface. The horizontal bars mark the spatial intervals over which average defect densities were measured, and the vertical bars arise from uncertainty in the measured signal. Determination of the spatial intervals depends on the net dopant concentration⁸, which is less certain near the junction, as signified by the dashed-line segment of the defect distribution. The defect density remains in the 10^{13} cm^{-3} range to greater than a micron below the junction.

Unimplanted Schottky diodes were used to investigate SEBA-induced defects in n -type silicon. The diodes received the same beam-annealing schedule used to recrystallize As⁺-implanted amorphous layers. In Fig. 3 the electron emission spectrum for a SEBA-annealed diode is compared to that for unannealed material. The spectrum for beam-annealed silicon is dominated by two emission peaks with activation energies of 0.19 and 0.44 (± 0.01) eV. Shoulders on both peaks indicate additional unresolved emission centers; the shoul-

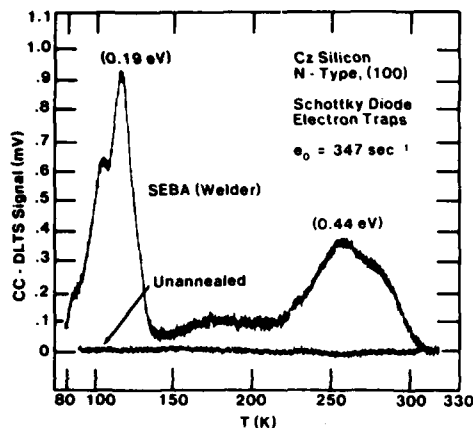


FIG. 3. CC-DLTS spectrum for electron emission in unimplanted scanned electron-beam annealed silicon. Also shown is the spectrum for the unannealed material.

der on the 0.44-eV peak is less pronounced in spectra recorded nearest the Si surface, where the trap density is largest (see Fig. 4), thus permitting an accurate determination of energy. In the unannealed control, no emission peaks are detectable on the indicated scale of sensitivity. The spatial distributions of the principal SEBA-induced levels are shown in Fig. 4; the densities have not been corrected for contributions from the unresolved secondary peaks. The densities of both defects decrease exponentially with distance from the electron-irradiated surface, over the investigated range, with the minimum depth set by the zero-bias depletion width of the Schottky diode.

The hole emission centers detected in SEBA-processed *p-n* junction diodes (Fig. 1) can be tentatively identified based on previous studies of point defects in silicon. The level at 0.28 eV matches within experimental error (± 0.01 eV) a defect state at 0.27 eV, which has been assigned to interstitial carbon.⁹ The hole trap at $E_c + 0.36$ eV has been assigned to the defect complex consisting of substitutional carbon adjacent to interstitial carbon.^{9,10} In the present study, the two defects reveal an incomplete removal of ion-implantation damage by SEBA processing. As evident in Fig. 2, the measured defects reside in material that was not driven amorphous by ion implantation, since the metallurgical junction is necessarily located beneath the initially amorphous layer. For silicon device applications, an encouraging feature is the low density of defect levels near midgap, where they are most efficient as charge generation and recombination centers according to Shockley-Reed-Hall theory.¹¹ A study is planned to evaluate residual defects from SEBA processing with heated substrates. In addition, it has been shown in cw laser-annealed diodes that the 0.28-eV hole trap is removed by a furnace anneal at 450 °C.¹²

The results presented in Figs. 3 and 4 provide the first experimental evidence of SEBA-induced defects in silicon. The basic mechanism leading to defect formation may differ from that giving rise to point defects during MeV-electron irradiation; specifically, localized heating and rapid quenching, rather than collisional displacement of lattice atoms, may provide the stimulus for defect formation during electron-beam annealing. We propose that the measured defect

distributions (Fig. 4) arise from the thermal generation of vacancies, and their subsequent diffusion and capture by impurities to form immobile vacancy-impurity complexes. The 0.44-eV level identifies the phosphorus-vacancy complex.⁹ We suggest that the 0.19-eV level is a multidefect complex involving the lattice vacancy and oxygen. This level is observed in ion-implanted cw laser-annealed silicon and is removed by a 450 °C furnace anneal.^{5,6} The absence of divacancies, with states at $E_c - 0.23$ eV and $E_c - 0.41$ eV,⁹ is consistent with impurity-dominated trapping kinetics.

The essential features of the vacancy-diffusion model can be illustrated by considering the idealized case in which an intense electron beam elevates the silicon surface region to a sufficiently high temperature for significant vacancy generation. The surface then serves as the principal source for vacancy diffusion into the substrate, where vacancies are trapped with the formation of immobile defect complexes. With the assumptions that the vacancy diffusivity D_v is a constant and the trapping rate is first order, the vacancy concentration C_v must satisfy the following continuity equation in the substrate,

$$\frac{\partial C_v}{\partial t} = D_v \frac{\partial^2 C_v}{\partial x^2} - \frac{C_v}{\tau_v}, \quad (1)$$

where τ_v is the vacancy lifetime, the reciprocal of which equals the sum of the reciprocal lifetimes due to separate impurity trapping centers. For typical electron-beam dwell times of the order of 1 msec, we solve Eq. (1) for the steady-state vacancy distribution, with the vacancy concentration at the surface denoted by C_{v0} and $C_v \rightarrow 0$ deep in the substrate: $C_v(x) = C_{v0} \exp(-x/L_v)$, where the vacancy diffusion length $L_v \equiv (D_v \tau_v)^{1/2}$. The defect distributions should reflect the exponential variation of the vacancy concentration, with a decay length L_v . Within the accuracy of the two measured distributions (Fig. 4) the decay lengths are equal, with a value of 860 Å obtained from the 0.19-eV profile. A comparable vacancy diffusion length has been reported from

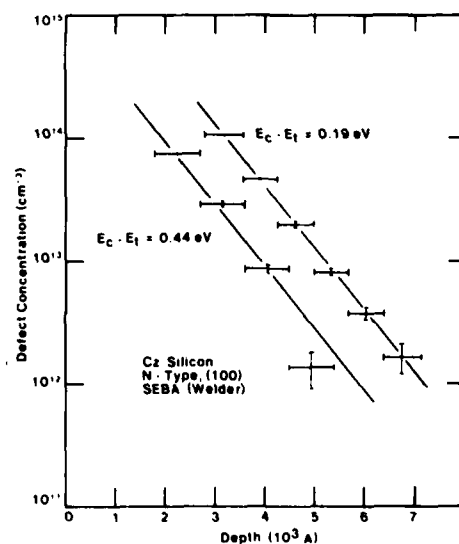


FIG. 4. Spatial depth profiles of the defect levels at $E_c - 0.19$ eV and $E_c - 0.44$ eV in unimplanted scanned electron-beam annealed silicon.

proton-enhanced diffusion studies in silicon.¹³ For an estimated vacancy diffusivity of 10^{-3} cm²/sec,^{13,14} the vacancy lifetime is ~ 0.1 μ sec, which justifies the steady-state formulation. A more detailed analysis of beam-induced defects will be presented elsewhere.

The authors express their appreciation to R.F.W. Pease for helpful discussions on SEM annealing. The authors also thank D. Moyer, N. Latta, and C. Healy for assistance with sample preparation and D. Bernsen for typing the manuscript. The work at Stanford University was partially supported by ARPA Contract MDA 903-78-C-0128.

¹J.L. Regolini, J.F. Gibbons, T.W. Sigmon, R.F.W. Pease, T.J. Magee, and J. Peng, *Appl. Phys. Lett.* **34**, 410 (1979).

²K.N. Ratnakumar, R.F.W. Pease, D.J. Bartelink, N.M. Johnson, and J.D. Meindl, *Appl. Phys. Lett.* **35**, 463 (1979).

³K.N. Ratnakumar, R.F.W. Pease, D.J. Bartelink, and N.M. Johnson, *J. Vac. Sci. Technol.* (to be published).

⁴J.L. Regolini, N.M. Johnson, R. Sinclair, T.W. Sigmon, and J.F. Gibbons, *Laser and Electron Beam Processing of Materials* (Academic, New York, to be published) edited by C.W. White and P.S. Percy.

⁵N.M. Johnson, R.B. Gold, and J.F. Gibbons, *Appl. Phys. Lett.* **34**, 704 (1979).

⁶N.M. Johnson, R.B. Gold, A. Lietoila, and J.F. Gibbons, *AIP Conf. Proc.* **50**, 550 (1979).

⁷D.V. Lang, *J. Appl. Phys.* **45**, 3023 (1974).

⁸N.M. Johnson, D.J. Bartelink, R.B. Gold, and J.F. Gibbons, *J. Appl. Phys.* **50**, 4828 (1979).

⁹L.C. Kimerling, *Inst. Phys. Conf. Ser.* **31**, 221 (1977).

¹⁰L.C. Kimerling, W.M. Gibson, and P.W. Blood, *Inst. Phys. Conf. Ser.* **46**, 273 (1979).

¹¹A.S. Grove, *Physics and Technology of Semiconductor Devices* (Wiley, New York, 1967), Chaps. 5 and 6.

¹²N.M. Johnson, D.J. Bartelink, M.D. Moyer, J.F. Gibbons, A. Lietoila, K.N. Ratnakumar, and J.L. Regolini, *Laser and Electron Beam Processing of Materials* (Academic, New York, to be published), edited by C.W. White and P.S. Percy.

¹³R.L. Minear, D.G. Nelson, and J.F. Gibbons, *J. Appl. Phys.* **43**, 3468 (1972).

¹⁴G.D. Watkins, *Inst. Phys. Conf. Ser.* **23**, 1 (1975).

A COMPARISON OF ION-IMPLANTATION INDUCED DEEP LEVELS IN SCANNED ELECTRON-BEAM ANNEALED AND CW LASER- ANNEALED SILICON

N. M. Johnson, D. J. Bartelink, and M. D. Moyer
Xerox Palo Alto Research Center
Palo Alto, California

J. F. Gibbons, A. Lietoila, K. N. Ratnakumar, and J. L. Regolini
Stanford Electronics Laboratories
Stanford, California

Electronic defect levels in scanned electron-beam annealed and CW laser annealed p-n junction diodes on silicon have been measured by deep-level transient spectroscopy. In As^+ -implanted diodes, the dominant hole trap appears at $E_V + 0.28$ eV, with a second major level at $E_V + 0.36$ eV. The densities of both defects remain in the 10^{13}-cm^{-3} range to depths of greater than $1\text{ }\mu\text{m}$ below the junction. Both levels are tentatively identified with carbon complexes in silicon. A 450-C furnace anneal removes the hole trap at 0.28 eV and reveals an electron trap at $E_C - 0.28$ eV in the near junction region. The reverse-bias leakage current is also significantly reduced by the furnace anneal. The hole trap is not removed by CW laser annealing with the substrate heated to 350 C.

I. INTRODUCTION

It has been demonstrated that both a CW laser beam (1-2) and a scanned electron beam (3) can be used to anneal ion implantation damage in silicon. With both forms of beam annealing, the processed silicon displays the following properties (2-5): (1) the entire implanted amorphous layer is recrystallized, with the annealed layer displaying a structural perfection comparable to that of the starting material; (2) there is no significant dopant redistribution, which is consistent with solid-phase epitaxial regrowth of the amorphous layer; and (3) the electron mobility displays the predicted dependence on dopant concentration. These results show that CW beam annealing is a potentially powerful processing technique for silicon IC technology. In this paper, results are presented from a study of

residual point defects in CW beam processed silicon. Similar studies on self-implanted CW laser-annealed silicon have revealed high densities of deep levels, as compared to specimens receiving a conventional furnace anneal (6). In the present study, point defects were measured in As^+ -implanted p-n junction diodes which were processed with either a scanned electron beam or a CW laser.

II. EXPERIMENT

The p-n junction diodes were fabricated on B-doped ($1-3 \Omega\text{-cm}$) (100)-oriented Czochralski-grown silicon. To obtain Ohmic contact, boron was implanted into the back surface of the silicon wafers and electrically activated with an anneal at 800 C (30 min.). The degenerately doped back surface was then coated with aluminum and sintered (450 C, 30 min.). Preparation of back contacts was completed prior to front surface processing. To form p-n junctions, As^+ was implanted into the front surface at 100 keV to a dose of $5 \times 10^{14} \text{ cm}^{-2}$, which drives the silicon amorphous to a depth of approximately 1000 Å. Both scanned electron-beam annealing and CW laser annealing were used to recrystallize the amorphous layer and activate the implanted arsenic. Scanned electron-beam annealing was performed with both a commercial electron-beam welder (3) and a scanning electron microscope (SEM), which was modified for high-current operation (4). For electron-beam annealing, the system parameters were as follows: for the welder the electron energy was 31 keV, the beam current was 300-400 μA , the scan rate was 20 cm/sec, the beam diameter was $\leq 300 \mu\text{m}$, and the scan-line separation was $< 100 \mu\text{m}$. With the SEM the energy was 20 keV, the current was 50-70 μA , the line scan was 10 cm/sec, the beam diameter was $\sim 10 \mu\text{m}$, and the scan-line separation was $0.25 \mu\text{m}$. Laser anneals were performed with the scanned and focused beam from a CW argon-ion laser. For anneals with the substrate at room temperature, the beam power was 9.75 W, the beam diameter was $30 \mu\text{m}$, the scan rate was 0.75 cm/sec, and the scan-line separation was $10 \mu\text{m}$. For laser anneals with the substrate held at 350 C, the beam power was 11.5 W, the beam diameter was $80 \mu\text{m}$, the scan rate was 5 cm/sec, and the scan-line separation was $30 \mu\text{m}$. The beam powers quoted above are typically $\sim 90\%$ of those required to melt the silicon surface, and the lateral uniformity of the anneals was confirmed from Nomarski interference microscopy. After beam processing, the p-n junction diodes were completed by vacuum evaporating aluminum over the front surface and using conventional photolithography and plasma etching to define a mesa structure.

The above test devices were evaluated with deep-level transient spectroscopy (DLTS) (7). The measurement, performed in the constant-capacitance mode (CC-DLTS), provided temperature spectra for thermal emission of trapped charge and spatial depth profiles of selected defects. Details of the measurement and analysis are presented elsewhere (8).

III. RESULTS

CC-DLTS spectra are presented in Fig. 1 for hole emission in scanned electron-beam annealed diodes. Spectra were recorded, with the same emission rate window e_0 , for diodes which were processed with the electron-beam welder and the SEM; the spectrum for a furnace-annealed control is also shown. In parentheses are listed the activation energies obtained from an Arrhenius analysis of the emission rate (8). The hole trap at 0.28 eV dominates the emission spectra, with an additional peak appearing at 0.36 eV in the SEM-annealed diode. In the furnace annealed diode, no emission peaks are detectable on the indicated scale of sensitivity. The defect at 0.28 eV is present in comparable densities in both electron-beam annealed diodes. In the present study, emission peak intensities varied by a factor of $2 \rightarrow 3$ for diodes prepared by the same processing techniques but processed at different times.

The spectrum for a welder-annealed diode is shown in Fig. 2. Here, the spectrum is dominated by the peak at 0.36 eV. The scale of sensitivity, and the volume of sampled material, is the same as in the previous figure, which indicates that the defects are present in comparable densities. The spatial depth profile of the 0.36-eV level is shown in Fig. 3. The profile is measured relative to the metallurgical junction, which is estimated to be 1500 Å below

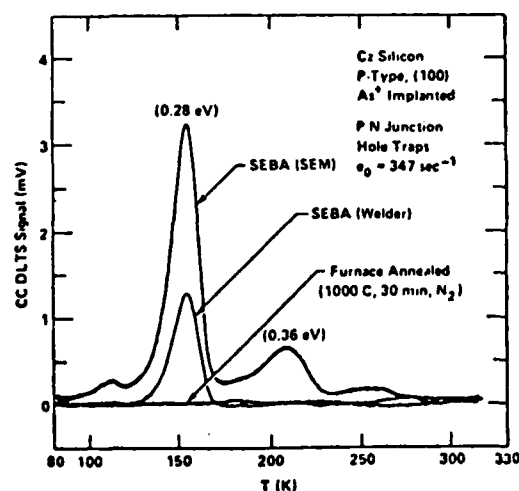


FIGURE 1. Hole emission spectra for As^+ -implanted p-n junction diodes which were SEM, e-beam welder, and furnace annealed.

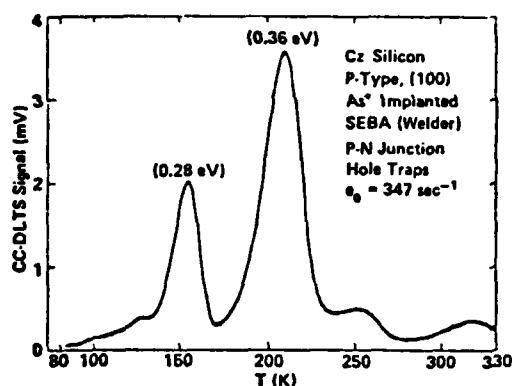
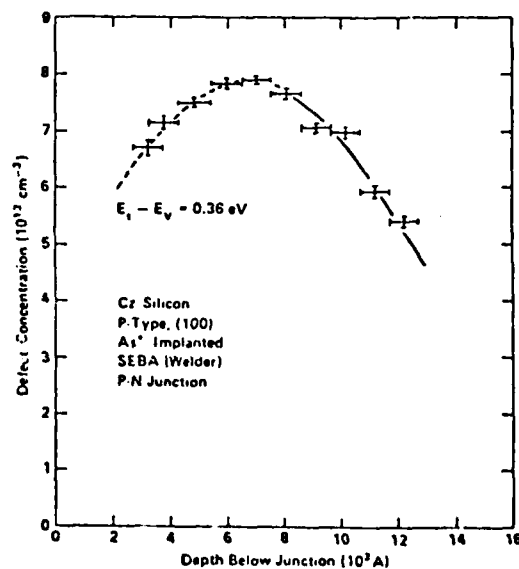


FIGURE 2. CC-DLTS spectrum for hole emission in an e-beam welder annealed diode.

the silicon surface. The horizontal bars mark the spatial intervals over which average defect densities were measured, and the vertical bars signify uncertainty in the measured signal (8). Determination of the spatial intervals depends on the net dopant concentration (8) which is uncertain near the junction, as signified by the dashed-line segment of the defect distribution. The defect density remains in the 10^{13}-cm^{-3} range to greater than $1\text{ }\mu\text{m}$ below the junction.

Trap emission spectra for CW laser annealed diodes are shown in Fig. 4. The spectrum in Fig. 4 (a) was obtained from a diode which was laser annealed with the substrate maintained at room temperature. The spectrum consists of the hole emission center at $E_V + 0.28\text{ eV}$ and a broad emission peak of reverse polarity near room temperature. In a p-n junction diode, the reverse polarity signifies minority carrier emission (7), which in this case arises from electron emission from traps in the lower half of the silicon bandgap. The observation of a similar broad emission of reverse

FIGURE 3. Spatial depth profile of the defect level at $E_V + 0.36\text{ eV}$.



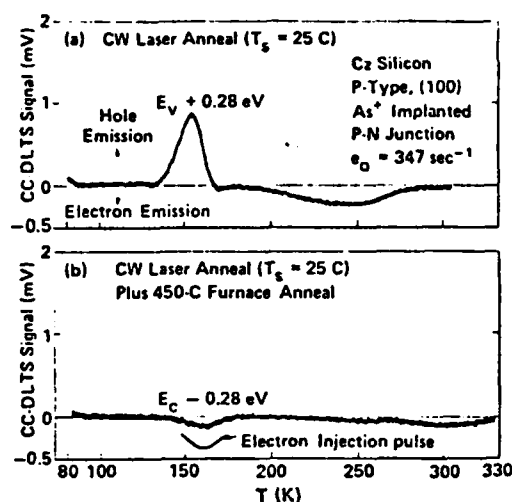


FIGURE 4. CC-DLTS emission spectra for CW laser annealed diodes. In (a) the diode received only the laser anneal, and in (b) the diode also received a 450-C furnace anneal.

polarity in furnace annealed control diodes (e.g., Fig. 1) as well as in beam-processed diodes suggests that the electron emission is due in part to edge effects in the mesa structure. However, from Fig. 4 it is evident that the electron emission arises largely from the properties of the junction itself. Figure 4 (b) shows the spectrum for a diode which was processed simultaneously with that of Fig. 4 (a) except for the addition of a 450-C furnace anneal which was performed immediately after CW laser annealing. Both diodes were then aluminum metallized and plasma etched to define the mesa diodes so that the edges received identical treatment. It is seen in Fig. 4 (b) that the hole trap at 0.28 eV is absent and the broad emission near room temperature has been significantly reduced in intensity. In addition, a new electron emission peak appears corresponding to an electron trap at $E_C - 0.28$ eV. The electron emission intensity is slightly enhanced by using a forward-bias voltage pulse for trap filling which injects electrons (minority carriers) into the substrate. This suggests that the electron traps are located near the metallurgical junction. This new electron emission peak appears at nearly the same temperature as the hole emission peak and apparently is masked by the more intense hole emission in Fig. 4 (a). The removal of the hole trap at $E_V + 0.28$ eV uncovers the residual electron trap, which requires higher anneal temperatures for removal (6).

The observed reduction in defect density is accompanied by a decrease in the reverse-bias leakage current for the above diodes, as shown in Fig. 5. The mesa diode is a poor test device for leakage-current measurements because of the exposed p-n junction which gives rise to large surface leakage currents that are sensitive to surface preparation. However, the identical processing received by the above CW laser annealed diodes permits a meaningful comparison of the *relative* magnitudes of the leakage currents. As shown in Fig. 5, the low-temperature furnace

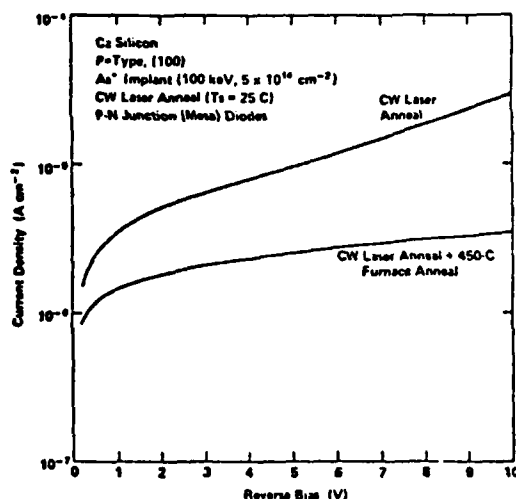


FIGURE 5. Reverse-bias leakage current for CW laser annealed (mesa) diodes.

anneal produces a significant improvement in the reverse current-voltage characteristics of the diodes.

The observed reduction in defect density realized by a 450-C furnace anneal after laser annealing suggests that a similar reduction should be achievable by laser annealing with a heated substrate. Results are presented in Fig. 6 for a diode which was CW laser annealed at a substrate temperature T_S of 350 C. The spectrum displays the same features as in Fig. 4 (a). The dominant feature is the hole trap at $E_V + 0.28$ eV; also evident is the broad electron emission near room temperature. As remarked earlier, a factor of $2 \rightarrow 3$ in peak intensity represents the degree of reproducibility at the present state-of-the-art in beam processing so that from Figs. 4 (a) and 6 it can only be concluded that the 0.28-eV level is present in comparable densities in diodes CW laser annealed with T_S equal to room temperature and 350 C.

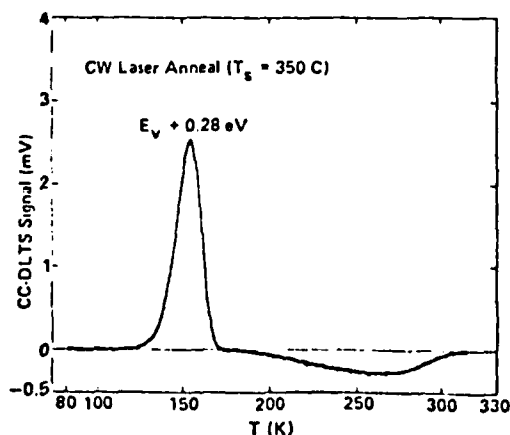


FIGURE 6. Hole emission spectrum for a diode CW laser annealed with $T_S = 350$ C.

IV. DISCUSSION AND CONCLUSIONS

Previous work on point defects in silicon provide tentative identifications for the trap emission centers observed in the present study. The hole trap at $E_V + 0.28$ eV matches within experimental error (± 0.01 eV) a defect state at 0.27 eV which has been assigned to interstitial carbon, and the hole trap at $E_V + 0.36$ eV has been assigned to the C_I-C_S complex (9). The electron trap at $E_C - 0.28$ eV has not been microscopically identified, but it has been previously observed in ion implantation and laser annealing studies in silicon (6,8). The broad electron emission signal observed near room temperature has not been identified.

From the present study it is concluded that the same defect levels are present in comparable densities in As^+ -implanted diodes which are annealed with either a scanned electron beam or a CW laser. The hole and electron traps reveal an incomplete removal of ion-implantation damage by beam processing. As evident in Fig. 3, the measured defects reside in material that was not driven amorphous by ion implantation, since the metallurgical junction is necessarily located beneath the initially amorphous layer. For silicon device applications, encouraging observations are the removal of the 0.28-eV hole trap and the reduction in reverse-bias leakage current by a furnace anneal at 450 C, which is compatible with present Si IC processing procedures. Studies are in progress to evaluate residual defects in silicon for beam processing over a range of substrate temperatures and to characterize defects in oxide-passivated silicon diodes.

REFERENCES

1. G. A. Kachurin, E. V. Nidaev, A. V. Khodyachikh, and L. A. Kovaleva, *Sov. Phys.-Semicond.* **10**, 1128 (1976).
2. A. Gat, J. F. Gibbons, T. J. Magee, J. Peng, V. Deline, P. Williams, and C. A. Evans, Jr., *Appl. Phys. Lett.* **32**, 276 (1978).
3. J. L. Regolini, J. F. Gibbons, T. W. Sigmon, R. F. W. Pease, T. J. Magee, and J. Peng, *Appl. Phys. Lett.* **34**, 410 (1979).
4. K. N. Ratnakumar, R. F. W. Pease, D. J. Bartelink, N. M. Johnson, and J. D. Meindl, *Appl. Phys. Lett.* **35**, 463 (1979).
5. J. L. Regolini, N. M. Johnson, R. Sinclair, T. W. Sigmon, and J. F. Gibbons (this conference).
6. N. M. Johnson, R. B. Gold, A. Lietoila, and J. F. Gibbons, *AIP Conf. Proc.* **50**, 550 (1979).
7. D. V. Lang, *J. Appl. Phys.* **45**, 3023 (1974).
8. N. M. Johnson, D. J. Bartelink, R. B. Gold, and J. F. Gibbons, *J. Appl. Phys.* **50**, 4828 (1979).
9. L. C. Kimerling, *Radiation Effects in Semiconductors 1979* (Inst. Phys. Conf. Ser. **31**, Bristol, 1977), p. 221.

(Invited) Applications of Scanning CW Lasers and Electron Beams in Silicon Technology

J. F. GIBBONS

Stanford Electronics Laboratories Stanford, California 94305

Scanning cw laser and electron beams provide an extremely convenient tool for rapidly heating the surface of a semiconductor to a precisely controlled temperature. As a result, they can be used for a variety of semiconductor processing operations, including growth of surface oxides, reduction of Q_{ss} in deposited oxide films, the annealing of ion implanted layers and the improvement of the electrical properties of both metal silicides and deposited silicon films. Experiments performed to explore these processes will be discussed in this paper.

§1. Introduction

Extensive research has been performed over the past few years on the use of both lasers and electron beams for annealing damage created in silicon by ion implantation. At Stanford we have concentrated primarily on the use of scanned cw laser and electron beams for annealing ion implanted silicon.¹⁻⁴ The principal results obtained from this work, to be elaborated upon below, are as follows:

(1) for thin amorphized layers of silicon, the annealing process is a solid phase epitaxial regrowth for which the critical beam parameter is the beam power divided by the spot size (approximately 0.2 W/micron);

(2) recrystallization of the damaged layer is perfect (no residual damage in TEM) to within a resolution of approximately 50 Å;

(3) no diffusion of implanted impurities occurs during the annealing, irrespective of whether the material is driven amorphous by the implantation;

(4) electrical activity can be essentially 100% even for impurity concentrations that exceed the solid solubility limit;

(5) doped polycrystalline silicon (deposited on either Si_3N_4 or SiO_2) can be annealed to provide an increase in grain size from approximately 200 Å (as prepared) to $2 \mu \times 25 \mu$ (after annealing) with correspondingly significant reductions in the sheet resistance of the film.

All of these effects can be related directly to the fact that the scanning electron or laser beam provides an extremely convenient and highly controllable process for heating the surface of a semiconductor to a given temperature. Recogni-

tion of this fact leads naturally to the development of a number of other processes that are of interest in silicon device technology, namely growth of oxides, reduction of Q_{ss} in deposited oxides, and control of the reaction between metals such as palladium and silicon to form single phase metal silicides. In what follows we describe first the basic physics of the process and then consider its applications to semiconductor device technology.

§2. Basic Laser Annealing Systems

The basic annealing system used for our scanned cw laser experiments is shown schematically in Fig. 1 and described in Ref. 1. The output of an Ar or Kr cw laser is passed through a lens and deflected by X and Y mirrors onto a sample that is mounted in the focal plane of the lens. The X mirror is mounted on a galvanometer that is driven with a triangular waveform and the Y mirror is mounted on a galvanometer that is driven by a staircase waveform. This arrangement permits the beam to be scanned across the target in the X direction, stepped by a controlled Y increment and then scanned back across the target in reverse X direction. Individual scan lines can be overlapped or not by appropriate adjustments

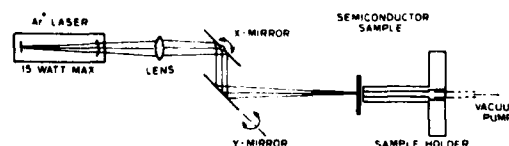


Fig. 1. A general schematic of the annealing apparatus, including Ar⁺ laser, lens perpendicular X and Y mirrors, and a vacuum sample holder.

of the Y step.

The samples are mounted on a sample holder that can be heated to about 500°C using a set of cartridge heaters mounted in the back of the sample holder (not shown). Control of the annealing ambient can be obtained by placing a cylindrical quartz jacket around the sample holder and pumping appropriate gases into this jacket. A variety of lenses, laser powers, scan rates, and sample temperatures have been found to produce essentially perfect annealing of ion implanted semiconductors. If the samples are held at room temperature, a typical set of annealing conditions consists of a laser output (Ar, multi-line mode) of 7 W focused through a 79 mm lens into a 38 micron spot on the target. This spot is typically scanned across the target at a rate of approximately 2.5 cm per second. Adjacent scan lines are overlapped by approximately 30% to produce full annealing in the overlapped areas. The laser power for full annealing can be reduced (and the width of the annealed line increased) by increasing the sample temperature.

§3. Surface Temperature Profiles

The beam geometry and scanning conditions listed above lead to a spot dwell time on the order of 1 ms. This is to be compared to a thermal time constant (for a 40 μm cube of Si) of approximately 10 μs , from which it follows that the semiconductor surface has adequate time to come to thermal equilibrium with the scanning heat source. It is therefore possible to calculate exactly the surface temperature that will be produced at the center of the spot by simply solving the steady state equation for heat flow. Calculations of this type have been carried out for both circular and elliptical scanning beams;⁵⁾ the results for a cylindrical beam irradiating a silicon substrate are shown in Fig. 2. The calculations presented there account for the temperature dependence of the thermal conductivity and specific heat, and have proven to give very accurate estimates of the surface temperatures achieved with the laser beam.

Two features of these curves are worth particular attention. First, the horizontal axis is in units of power per unit radius of the beam, this being due to the fact that the heat flow problem has essentially hemispherical symme-

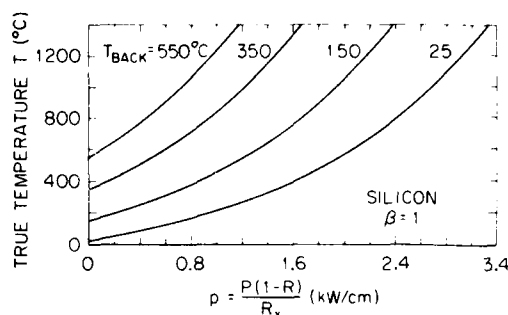


Fig. 2. The true maximum temperature ($X=Y=Z=V=0$) in Si is plotted versus the normalized power p ($p=P(1-R)/R_s$) for different substrate back-surface temperatures.

try. As a result the surface temperature is a function of power divided by spot radius rather than power per unit area of the beam. Secondly, the sizeable decrease of thermal conductivity of Si with temperature leads to a situation in which the temperature at the irradiated surface is a very sensitive function of the back-surface temperature. For example, a surface temperature at the center of a 40 micron spot of 1000°C can be obtained with a 5 watt laser output if the back-surface temperature (or thermal bias) is 350°C. If the back-surface temperature is reduced to 150°C, the temperature in the center of the irradiated area drops by nearly 500°C. Hence it is very important to control the back-surface temperature accurately, and it is also possible to use relatively low laser powers if substantial thermal bias can be employed.

§4. Results for Ion Implanted Single Crystal Si

In this section we will consider the basic experimental results which have been obtained using scanning laser and electron beams to anneal ion implanted silicon.

4.1 As⁺-implantations

Samples for the first set of experiments were prepared by implanting $3 \times 10^{14}/\text{cm}^2$ As⁺ at 100 keV into purposely misoriented $\langle 100 \rangle$ Si. Rutherford backscattering measurements show that this dose is sufficient to drive the Si amorphous to a depth of ~ 1000 Å.

After implantation the wafers were cut into a number of 5 mm \times 5 mm samples and annealed under a variety of conditions. For comparison purposes, some samples were thermally annealed at 1000°C for 1/2 hour, a

treatment that is known to be sufficient to recrystallize the amorphous layer on the underlying substrate and incorporate essentially all of the implanted As atoms on substitutional sites. Other samples were annealed with the scanned cw laser beam under a variety of conditions. The following results were obtained with the conditions described previously.

4.1.1 Sheet resistance

The probe-to-probe resistance was measured on an ASR Model 100 spreading resistance probe.²⁾ The thermally annealed samples exhibit a probe-to-probe resistance of $157 \pm 3 \Omega$, corresponding to a sheet resistance of $\sim 200 \Omega/\square$. The laser annealed samples show an essentially identical sheet resistance in the annealed area ($160 \pm 10 \Omega$) and a probe-to-probe resistance of $\sim 3000 \Omega$ in the unannealed (as-implanted) area. Similar experiments performed with overlapped scan lines show that the laser can recrystallize the amorphous layer at least as well as a thermal anneal, with regard to both crystallinity and substitutionality of the unimplanted species, as long as the scan lines are overlapped by at least 30%.

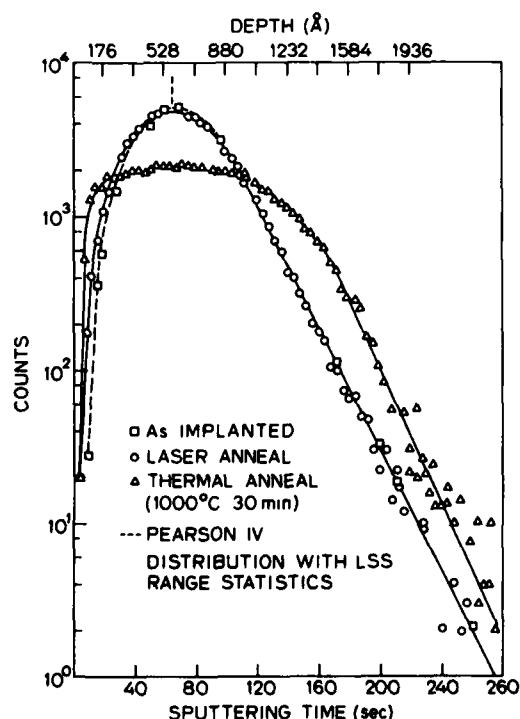


Fig. 3. Carrier concentration and mobility profiles obtained on As-implanted samples annealed with a scanning Ar cw laser beam.

4.1.2 Impurity profile

Figure 3 shows the impurity profiles obtained by SIMS under as-implanted, laser annealed and thermally annealed conditions. The most striking feature of this figure is that the laser annealed profile is identical to the as-implanted profile. In other words, there has been no diffusion of the implanted species during the laser anneal. Furthermore, the as-implanted impurity distribution is matched exactly by the Pearson type IV distribution function using LSS moments, so the experimental and theoretical profiles are in excellent agreement. The thermal anneal shows the well-catalogued impurity redistribution given by the open triangles in Fig. 3.

Majority carrier profiles and carrier mobilities were obtained by sheet resistance and Hall effect measurements and are shown in Fig. 4. As can be seen the carrier concentration profile also fits the Pearson type IV distribution quite well. Under very high dose conditions ($> 10^{16}/\text{cm}^2$), As precipitation can occur near the peak of the profile, leading to a residual, nonsubstitutional As content of approximately 5%.⁶⁾

4.1.3 Transmission electron microscopy

Typical results of TEM performed on thermally annealed and laser annealed samples

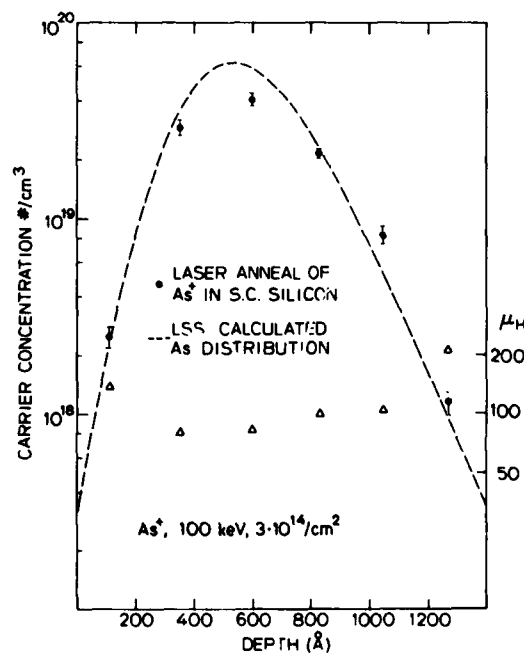


Fig. 4. As concentration profile in As-implanted silicon after laser anneal and thermal anneal.

are shown in Fig. 5. The thermally annealed sample (Fig. 5a) shows a single crystal diffraction pattern with a bright field micrograph containing the usual variety of ~ 200 Å diameter defect clusters and dislocation loops. The laser annealed sample shown in Fig. 5b is essentially free of any defects observable in TEM except near the boundary between crystallized and amorphous regions. It should be emphasized also that no defects are observed

in TEM in the region where adjacent scan lines overlap.

4.1.4 Recrystallization model

The absence of diffusive redistribution rules out a melting/liquid phase epitaxial recrystallization mechanism for the anneal, such as is believed to occur for Q-switched laser annealing.^{7,8)} Instead, it has been shown by two independent experiments^{9,10)} that under proper operating conditions the scanning cw laser promotes solid phase epitaxial recrystallization of the amorphized layer. The solid phase growth rates obtained are within experimental error of those obtained by extrapolating the measurements of Csepregi *et al.*¹¹⁾ to the surface temperature calculated from Fig. 2. A similar orientation dependence is also measured.

A solid phase epitaxial recrystallization model will of course explain all of the previous data satisfactorily, especially the absence of any apparent As diffusion during the anneal. Such a result would be expected if the sample is not melted since the As diffusivity in either amorphous or crystalline Si is too low to permit significant redistribution in 1 ms (the laser spot dwell time in the scanning anneal).

4.2 B-implanted single crystal Si

A similar set of experiments has been performed in B-implanted Si. The central results, reported in Ref. 3, are identical to those described above for As-implanted Si. In particular, 100% electrical activity can be obtained with no diffusion of the implanted species from its as-implanted profile. Recrystallization is also perfect as judged by TEM to a resolution of ~ 20 Å. These results are independent of whether the B is implanted into pre-amorphized Si or directly into single crystal material.

§5. Doped Polycrystalline Si

An interesting and potentially very important application of the scanning cw laser system is in the annealing of doped polycrystalline Si. This material is used for gates and interconnects in Si-gate MOS devices, where the sheet resistance of the material is an important (in some cases limiting) characteristic for device operation.

The material used for these experiments was ~ 0.5 μm thick undoped poly-Si obtained by

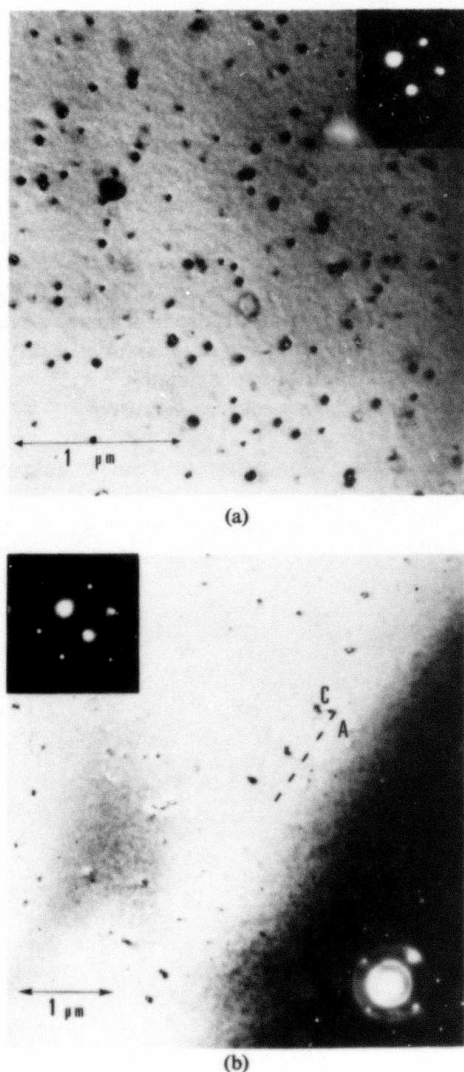


Fig. 5. Electron micrographs of As-implanted silicon subjected to thermal anneal of 1000°C 30 min (a) and laser annealing; (b) inserts show diffraction patterns which are typical to their regions.

low pressure CVD deposition on a Si_3N_4 amorphous substrate. B was implanted into as-received, undoped material to a level of $5 \times 10^{14}/\text{cm}^2$ at an energy of 60 keV. This results in a B peak near the center of the film and an average impurity concentration of $\sim 10^{19}/\text{cm}^2$.

Samples thermally annealed in flowing N_2 at 1000°C for 1/2 hour show a sheet carrier concentration of $4.7 \times 10^{14}/\text{cm}^2$ and a carrier mobility of $24 \text{ cm}^2/\text{V}\cdot\text{sec}$. The sheet resistance was $623 \Omega/\square$. These results are typical for ion-implanted, thermally annealed poly-Si. The relatively low mobility is due to the small grain size, measured to be $900\text{--}1200 \text{ \AA}$ for the experimental parameters listed above.

For laser annealing, a 136 mm lens was used in the apparatus shown in Fig. 1, with a total laser power of 11 watts, a scan rate of 12.5 cm/sec , and a sample temperature of 350°C . Under these conditions, as-implanted samples show, after laser annealing, a sheet carrier concentration that is essentially identical to the implanted dose and a carrier (hole) mobility of $45 \text{ cm}^2/\text{V}\cdot\text{sec}$. The sheet resistance of the laser annealed poly-Si is $269 \Omega/\square$, a factor of ~ 2.2 lower than that of the thermally annealed material. A further reduction in sheet resistance to $260 \Omega/\square$ can be obtained by laser anneal following a thermal anneal on account of the impurity redistribution that occurs during the thermal anneal.¹²⁾

The principal result of the laser anneal is the dramatic increase in carrier mobility. The

principal cause of this increase is shown in Fig. 6, where we show a transmission electron micrograph of the laser annealed poly-Si at the boundary of a laser scan line. The left side of the figure shows the as-deposited, as-implanted poly Si; the right side shows the material after laser anneal. The grain size in the laser annealed material has been increased very dramatically.

The laser annealed poly observed under less magnification is found to consist of crystallites that are $\sim 2 \mu\text{m} \times 25 \mu\text{m}$. These crystallites develop at an angle to the scan boundary, developing a chevron structure in the direction of the laser scan line. The crystallites show no evidence of fine grained poly-Si in the scanned region and appear to grow with no preferred orientation.

The increase in grain size leads to a situation in which lattice (including grain boundary) scattering is insignificant compared to impurity scattering (for the relatively high doping density employed). The result is that the carrier mobility obtained is essentially the same as would be obtained in a single crystal for the doping density employed.

§6. Thin Film MOSFETs Fabricated Directly on Laser-Annealed Polycrystalline Silicon

Polycrystalline silicon films formed by chemical vapor deposition are also a potentially important material for device fabrication. However, the relatively small grain size obtained under normal growth conditions makes device fabrication unfeasible since the grain boundaries usually determine the transport properties of the film. For example, pn junction diodes fabricated in poly-Si exhibit minority carrier lifetimes on the order of 20 psec;¹³⁾ and MOSFETs fabricated on such films have also exhibited poor electrical properties, particularly transconductance.¹⁴⁾

The similarity in electronic properties between laser annealed poly-Si and single crystal Si leads naturally to the question of whether MOSFETs with reasonable electrical characteristics can be fabricated directly in the laser annealed polycrystalline material. To study this possibility, conventional poly-Si samples having a thickness of 5500 \AA were prepared by low pressure chemical vapor deposition. The substrates were (for convenience only) single crystal Si onto which a 1000 \AA layer of silicon

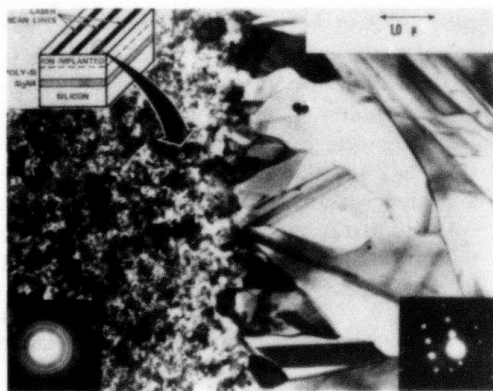


Fig. 6. Transmission electron micrograph of ion-implanted laser annealed poly-Si film at boundary of laser scan line; insets show selected area diffraction patterns characteristic of each region.

nitride had been deposited. Phosphorus was implanted at an energy of 100 kV to a dose of $3 \times 10^{12}/\text{cm}^2$ to form the channel for depletion mode devices. Boron was implanted at an energy of 100 kV to a dose of $3 \times 10^{11}/\text{cm}^2$ for the enhancement mode devices. The wafers were then annealed by an Ar cw scanning laser so that long grains were formed. The annealing conditions were similar to those just described. Enhancement and depletion mode devices were then prepared by conventional MOS processing.

The drain characteristics for these devices are found to be quite similar to those obtained using the same processing sequence on single crystal silicon.¹⁵⁾ Carrier mobilities in the channels of these devices are found to be approximately $340 \text{ cm}^2/\text{V}\cdot\text{sec}$, compared to a value of $630 \text{ cm}^2/\text{V}\cdot\text{sec}$ obtained in single crystal silicon. A 9-stage ring oscillator has been built on this material,¹⁶⁾ using devices with a gate length of 4 microns, with the ring oscillator exhibiting a period of 70 nsec. The period estimated for a similar ring oscillator built on single crystal material is 35 nsec.

These results suggest that poly-Si that is annealed under conditions that produce long grain crystallites can successfully be used for fabrication of integrated circuits, leading to the intriguing possibility of layered (high-rise) IC's.

§7. Laser-Assisted Oxidation of Silicon Surfaces

The fact that the surface of a silicon wafer can be heated to temperatures on the order of 1000° during laser annealing indicates that, if the surface is left in an oxidizing environment, SiO_2 can be expected to grow on the irradiated surface. By purposely providing the irradiated surface with a conventional oxidizing environment (O_2 or steam), this feature can be used to grow oxides of a desired thickness on a silicon substrate. Preliminary results on experiments of this type show that the oxidation rates for laser-assisted steam oxidation are comparable to the furnace oxidation rates. There is some possibility that the oxidation rate is enhanced somewhat over the purely thermal rate, due possibly to the electron-hole pair density produced by the laser beam. To date, the experiments have not been carried sufficiently far to either justify or negate the possibility of

enhancement of the oxidation rate due to the photon flux.

By repeated raster scanning of a silicon surface immersed in an oxidizing environment, it has been possible to grow $\sim 200 \text{ \AA}$ thick oxide layers having breakdown voltages of more than 20 V. There is a distinct tendency for slip lines to form on the surface of the underlying silicon under the oxidation conditions, though this effect can be minimized by using a relatively large substrate temperature and low laser power. Investigation of the electronic properties of silicon surfaces that have been oxidized by this process is currently underway.

§8. Reduction of Q_{ss} in Deposited SiO_2 Film

It is often important to be able to reduce the surface state charge density (Q_{ss}) in films that are intended for MOS device fabrication. SiO_2 films deposited by chemical vapor deposition typically have values of Q_{ss} that are far too large to be useful for MOS device fabrication, and it is therefore of interest to determine whether an annealing process can be used to reduce Q_{ss} in these deposited films.

Thermal annealing procedures have been devised that are capable of reducing Q_{ss} from an as-deposited value of approximately $5 \times 10^{11}/\text{cm}^2$ to a residual value of approximately $2 \times 10^{10}/\text{cm}^2$.

A set of preliminary experiments were performed to determine the effectiveness with which a scanning argon laser can be used to reduce Q_{ss} . A laser power of 6 W and a dwell time of 3 ms was found to be sufficient to reduce Q_{ss} to a level of $6 \times 10^{10}/\text{cm}^2$. This is not as low as can be obtained with thermal annealing procedures, but is nonetheless acceptable for some device applications. It seems likely that an appropriate combination of laser annealing parameters and annealing ambient will lead to a further reduction of Q_{ss} , to values that are essentially identical to those that can be obtained with a thermal anneal.

§9. Laser-Assisted Formation of Palladium Silicide

In work previously reported, we have used a scanning cw argon laser to successfully react very thin (approximately 300 \AA) layers of palladium with silicon to form single phase

palladium silicide (both PdSi and Pd_2Si). The reflection of light produced by thicker metal films in the original experiments was such that the metal/silicon reaction could not be controlled by the laser. To circumvent this problem, we decided to use E-gun evaporated layers of palladium (1000 Å thick) and silicon (500 Å thick) to form a Si-Pd-Si sandwich in which laser reflection from the front surface of the metal can produce sufficient energy deposition in the top layer of silicon to promote silicide formation.

The central results obtained with this experimental structure are shown in Figs. 7 and 8.¹⁷⁾ In Fig. 7 we show the backscattering spectra for both the unreacted palladium on silicon and the reacted layers that are produced when a 6 W, 40 μ spot is scanned across the multilayer film at a speed of 10 cm/sec (backsurface tempera-

ture of 25°C). Some interdiffusion of the silicon and palladium is apparent from this spectrum.

In Fig. 8 we show the backscattering spectra for 10 W and 12.5 W of laser power, respectively, and observe that for the 10 W condition there is complete mixing of the palladium and silicon in both directions from the center of the palladium film. The palladium-to-silicon ratio obtained from this data is exactly 2:1. Measurements made on a Read camera show that well over 95% of this film is single-phase Pd_2Si . When the laser power is increased to 12.5 W the palladium-to-silicon ratio changes to exactly 1:1, indicating that the average composition of the film is now 1:1 (Pd to Si). Once again X-ray analysis shows that the film is almost completely single phase PdSi .

§10. Scanning Electron Beams

We have used scanned cw electron beams to anneal arsenic implanted $\langle 100 \rangle$ silicon with results that are very similar to those obtained using the scanning laser.⁴⁾ This result has been obtained using both an electron beam welder and a modified scanning electron microscope as the instrument for providing the scanning electron beam. In both cases there is no redistribution of the implanted dopant during the annealing process, suggesting that solid phase epitaxy is the annealing mechanism for scanning electron beam annealing as well as scanning laser annealing. Essentially perfect recrystallization as judged by both transmission electron microscopy and the channeling effect is obtained for both cases, and electron concentrations in excess of 10^{21} electrons/cm³ have been found for the arsenic-implanted silicon layers. Mobilities agree well with values measured for bulk silicon samples of equivalent doping. Also, the reaction of refractory metals on silicon surfaces using the electron beam has been shown to provide an interesting process for forming metal silicide layers, in this case without the overlayer of silicon that is necessary if a laser beam is to be used.

Acknowledgments

The author is pleased to acknowledge the cooperation and suggestions of the Stanford University Laser/E-beam Annealing Mafia, effort, whose work has been summarized in this paper.

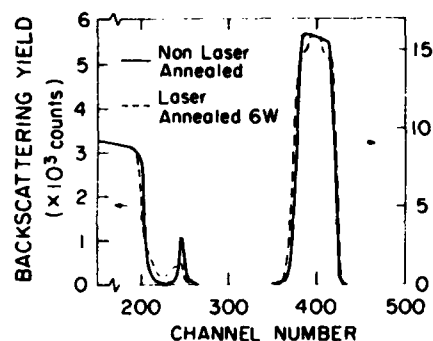


Fig. 7. MeV ^4He backscattering spectra for Si (200 Å)/Pd (1000 Å)/Si sample before and after laser anneal 6 W.

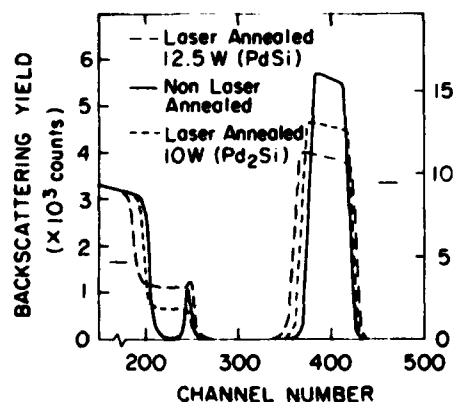


Fig. 8. MeV ^4He backscattering spectra for Si (200 Å)/Pd (1000 Å)/Si sample after being laser-annealed at various powers. Pd_2Si and PdSi were formed at 10 W and 12.5 W respectively.

He would also like to express his appreciation for the support provided by NSF Contract No. DMR78 19970 and ARPA Contract No. MDA903-78-C-0128; and to Drs. Richard A. Reynolds and Benjamin Wilcox for their continued interest and financial support of this program.

References

- 1) A. Gat and J. F. Gibbons: Appl. Phys. Lett. 32(1978) 142.
- 2) A. Gat, J. F. Gibbons, T. J. Magee, J. Peng, V. R. Deline, P. Williams and C. A. Evans, Jr.: Appl. Phys. Lett. 32(1978) 276.
- 3) A. Gat, J. F. Gibbons, T. J. Magee, J. Peng, P. Williams and C. A. Evans, Jr. Appl. Phys. Lett. 33(1978) 389.
- 4) J. F. Gibbons et al.: "Annealing of Ion-Implanted Si Using Scanned Laser and Electron Beams", *proc. of Laser-Solid Interactions and Laser Processing-1978, Boston Meeting, Materials Research Society, Boston, Nov. 28-Dec. 1, 1978*, Eds. S. D. Ferris, H. Leamy and J. M. Poate.
- 5) Nissim et al.: J. Appl. Phys. (accepted for publication).
- 6) W. Brown, "Laser Effects in Ion Implanted Semiconductors", E. Rimini, Ed., Inst. di Struttura della Materia, Universita di Catania, Corso, Italy.
- 7) G. K. Celler, J. M. Poate and L. C. Kimerling: Appl. Phys. Lett. 32(1978) 464.
- 8) H. G. Leamy, G. A. Rozgonyi, T. T. Sheng and G. K. Celler: Appl. Phys. Lett. 32(1978) 535.
- 9) J. S. Williams, W. L. Brown, H. J. Leamy, J. M. Poate, J. W. Rodgers, D. Rousseau, G. A. Rozgonyi, J. A. Shelnutt, and T. T. Sheng: Appl. Phys. Lett. 33(1978) 542; and D. H. Auston, J. A. Golovchenko, P. R. Smith, C. M. Surko, and T. N. C. Venkatesan: Appl. Phys. Lett. 33(1978) 539.
- 10) A. Gat, A. Lietoila and J. F. Gibbons: J. Appl. Phys. 50(1979) 2929.
- 11) L. Csepregi, J. W. Mayer and T. W. Sigmon: Appl. Phys. Lett. 29(1976) 92.
- 12) A. Gat, L. Gerzberg, J. F. Gibbons, T. J. Magee, J. Peng and J. D. Hong: Appl. Phys. Lett. 33(1978) 775.
- 13) J. Manoliu and T. I. Kamins: Solid-State Electron. 15(1972) 1103.
- 14) T. I. Kamins: Solid-State Electron. 15(1972) 789.
- 15) K. F. Lee, J. F. Gibbons, K. C. Saraswat and T. I. Kamins: Appl. Phys. Lett. 35(1979) 173.
- 16) T. I. Kamins, K. F. Lee, J. F. Gibbons and K. C. Saraswat: submitted to IEEE Trans. on Electron Devices.
- 17) T. Shibata, J. F. Gibbons and T. W. Sigmon: submitted to Appl. Phys. Lett.